

Combustion Characterization and Optimization of Outdoor Wood Burning Hydronic Heaters

Final Report

Prepared for:

New York State Energy Research and Development Authority

Albany, NY

Megan G. Bulman
Business Analyst

Michael E. Genovese
Project Manager

Prepared by:

The State University of New York at Buffalo (SUNYUB)

Buffalo, NY

Paul Desjardin, Professor
Joseph Mollendorf, Professor
Project Managers

Mark Odell, Econoburn
Dale Furman, Econoburn
Brian Bojko, PhD Student
Joseph Richter, PhD Student
Joshua Weisberger, PhD Student
Theodore Nalesnik, PhD Student

Notice

This report was prepared by SUNYUB in the course of performing work contracted for and sponsored by the New York State Energy Research and Development Authority (hereafter “NYSERDA”). The opinions expressed in this report do not necessarily reflect those of NYSEDA or the State of New York, and reference to any specific product, service, process, or method does not constitute an implied or expressed recommendation or endorsement of it. Further, NYSEDA, the State of New York, and the contractor make no warranties or representations, expressed or implied, as to the fitness for particular purpose or merchantability of any product, apparatus, or service, or the usefulness, completeness, or accuracy of any processes, methods, or other information contained, described, disclosed, or referred to in this report. NYSEDA, the State of New York, and the contractor make no representation that the use of any product, apparatus, process, method, or other information will not infringe privately owned rights and will assume no liability for any loss, injury, or damage resulting from, or occurring in connection with, the use of information contained, described, disclosed, or referred to in this report.

NYSERDA makes every effort to provide accurate information about copyright owners and related matters in the reports we publish. Contractors are responsible for determining and satisfying copyright or other use restrictions regarding the content of reports that they write, in compliance with NYSEDA’s policies and federal law. If you are the copyright owner and believe a NYSEDA report has not properly attributed your work to you or has used it without permission, please email print@nyserda.ny.gov

Information contained in this document, such as web page addresses, are current at the time of publication.

Abstract

An experimental and numerical modeling approach is utilized to study the combustion efficiency, characteristic emissions, and optimization strategies for a two-staged wood-fired boiler provided by Econoburn (EBW-200). The EBW-200 boiler operates through a dual stage combustion process by first burning wood fuel in the primary chamber. The products from the primary chamber are then redirected into a secondary chamber and combined with more oxygen to eliminate any unburnt hydrocarbons or volatile products such as CO and soot. Experimental procedures consist of accurately capturing the mass loss rate of the biomass fuel source, the combustion emissions of CO , NO , H_2O , and CO_2 , the heat output, and the overall combustion efficiency. A system level numerical model is used to estimate emissions output in real time using a combustion model that considers variable fuel compositions and accounts for the effects of finite-rate chemistry. Large eddy simulations (LES) for the turbulent flow of the secondary combustion chamber aid in the development of new boiler designs/alterations to reduce harmful emissions and increase overall efficiency. The combination of all three methods are used to better understand the combustion process of woody materials during an entire operating cycle of the hydronic heater, which is shown to be least efficient and release harmful emissions during the startup and shutdown phases.

Keywords

Wood Combustion, Biomass, Emissions, Hydronic Heater, Efficiency, Numerical Modeling, Simulation, Design Optimization, Variable Fuel

Acknowledgments

Thanks to Ms. Victoria Miller at Summit Wood Industries for their supply of the BIOBLOCKS[®] fuel used in this study, also Mr. Dale Furman and Mr. Mark Odell from Econoburn for their generous donation of the EBW-200 wood-fired boiler, consultation and support. We also thank Mr. Xinnan Peng and the University at Buffalo (UB) Engineering Machine Shop for their support in constructing the instrument modifications to the boiler. We would also like to acknowledge the support of UB's center for computational research (CCR) for the tremendous number of computational hours utilized during the numerical simulations.

Table of Contents

Notice	ii
Abstract.....	iii
Keywords	iii
Acknowledgments	iv
List of Figures	viii
List of Tables.....	x
Acronyms and Abbreviations	x
Executive Summary	1
1 Boiler Installation and Baseline Testing.....	1
1.1 Real Time Fuel Burn Rate Monitor (RTFBRM)	1
1.1.1 Conventional Approach: Weigh Entire Boiler.....	1
1.1.2 New Approach: Real time fuel burn rate monitor design	1
1.1.2.1 Concept	1
1.1.2.2 System Design.....	1
1.1.3 Components.....	2
1.1.3.1 Load Cell, Load Cell Base, and Load Cell Mount	2
1.1.3.2 Sliding Rods	3
1.1.3.3 Hanging Basket	3
1.1.3.4 Lift System for Lifting and Lowering Basket	4
1.1.4 General Operation of RTFBRM	4
1.1.5 Results	5
1.1.6 Conclusions	6
1.2 Baseline Testing of Boiler and Monitoring Equipment.....	7
1.2.7 Introduction	7
1.2.8 Experimental Methods.....	8
1.2.9 Performance Characterization: Efficiency Definitions	9
1.2.9.1 Emissions Measuring	12
1.2.10 Results and Discussion	12
1.2.10.1 Fuel Mass Monitoring	12
1.2.10.2 Efficiency	13
1.2.10.3 Emissions	14
1.2.11 Conclusions	14
2 Numerical Modeling and Combustion Optimization	27
2.1 Introduction	27
2.2 Experiments	27
2.2.1 Hydronic Heater Setup and Operation.....	27

2.2.2	Fuel Burn Rate Measurement and Fuel Type	28
2.2.3	Emission Measurements	28
2.2.4	Combustion Chamber Measurements	29
2.3	System Level Modeling	29
2.4	Results and Discussion	31
2.4.5	Solid Fuel Mass Loss and Mass Loss Rate	31
2.4.6	Emissions	33
2.4.6.1	Time Trends	33
2.4.6.2	State Maps	34
2.4.7	Thermal Efficiency	35
2.5	Conclusions	36
3	Emission Reduction Design and Testing	45
3.1	Introduction	45
3.2	Experimental Setup	46
3.3	Emissions Reduction Design Selection	47
3.3.1	Motivation for Design Selection	47
3.4	Modification of Boiler and Performance Testing	48
3.4.2	Experimental Results	48
3.4.3	Computational Simulations	49
3.5	Impact Plate Geometry Optimization and Minimization of CO	53
3.6	Conclusion	55
4	Fuel Sensitivity	86
4.1	Introduction	86
4.2	Experimental	87
4.2.1	Hydronic Heater Experimental Setup	87
4.2.1.1	Measurements of CO, NO, and O ₂	88
4.3	Emissions Analysis	88
4.4	Results	89
4.4.2	Time History: Elemental Fuel Composition	89
4.4.3	Time History: Heating Value	90
4.4.4	Time History: Thermal Efficiency	90
4.4.5	Total Emissions	91
4.5	Conclusion	91
5	Improving Emission Measurements	97
5.1	Water Vapor Corrections	97
5.1.1	Introduction	97
5.1.2	Experiments	99
5.1.3	Results	100
5.1.4	Conclusion	101
5.2	Emission Measurements using Laser Absorption Spectroscopy	102

5.2.5	Introduction	102
5.2.6	Experimental Facility	103
5.2.7	Emissions Analysis.....	103
5.2.7.1	Experimental Validation: TDLAS Measurements of CO ₂ and H ₂ O.....	104
5.2.8	Results	106
5.2.8.1	Time History: Elemental Fuel Composition.....	106
5.2.8.2	Time History: Heating Value	107
5.2.8.3	Time History: Thermal Efficiency	107
5.2.9	Conclusions	108
	References	119
	Appendix A. Testing and Safety Protocols.....	1

List of Figures

Figure 1-1. Schematic of RTFBRM Showing Front and Side View	15
Figure 1-2. Load Cell Mount Showing Intermediate Plate and Tube Spacer without Insulation	16
Figure 1-3. Load Cell Mount Assembly with Insulation	16
Figure 1-4. Safety Collar on RTFBRM with Upper Cross Member Assembly	17
Figure 1-5. Drawing of Stay Arrangement of Boiler for Sliding Rod	17
Figure 1-6. RTFBRM Hanging Basket.....	18
Figure 1-7. Inside View of Primary Combustion Chamber with Hanging Basket	19
Figure 1-8. Hanging Basket Lift System Mounted On Boiler.....	19
Figure 1-9. RTFBRM Mass Loss and Burn Rate Results.....	20
Figure 1-10. Normalized RTFBRM Mass Loss and Burn Rate Results	21
Figure 1-11. Instantaneous Heat Release Rates for Various Fuels	22
Figure 1-12. Boiler Experimental Schematic	23
Figure 1-13. Arrangement of BIOBLOCKS in Primary Chamber	23
Figure 1-14. RTFBRM Results Comparison of Data	24
Figure 1-15. Normalized RTFBRM Comparison of Data.....	25
Figure 1-16. Stack Loss Efficiency Comparison.....	25
Figure 1-17. Emissions Comparison	26
Figure 2-1. Econoburn Boiler, Internal View, Schematic.....	37
Figure 2-2. RTFBRM and Fuel Loading Configuration.....	38
Figure 2-3. Instrument Cluster Cell	39
Figure 2-4. Pyrolysis Products as a Function of Pyrolysis Temperature	39
Figure 2-5. Comparison of Mass (a) and Burn Rate (b) for Cases.....	40
Figure 2-6. Comparison of Normalized Mass and Burn Rate.....	41
Figure 2-7. Comparison of Characteristic Runs for System Level Model to Data	42
Figure 2-8. Emissions State Maps for Major Species	43
Figure 2-9. Summary of Thermal Efficiency Calculation	44
Figure 4-1. Experimental Schematic	57
Figure 4-2. Real Time Fuel Burn Rate Monitor with Hanging Basket.....	57
Figure 4-3. Cutaway View of Econoburn Two-Stage Hydronic Heater	58
Figure 4-4. Physical and Computational Model of Mixing Pot.....	58
Figure 4-5. Gas Temperature Measurements	59
Figure 4-6. Emission Measurements.....	60
Figure 4-7. CFD Domain of Econoburn.....	61
Figure 4-8. Econoburn Boiler Mesh with Mixing Pot	62
Figure 4-9. Mixing Pot Clearance Gap	63
Figure 4-10. High-speed Camera Image of Air-fuel Jet.....	64
Figure 4-11. Average and RMS Mixture Fraction of Baseline Case.....	65
Figure 4-12. TKE in Baseline Case	66
Figure 4-13. Average and RMS Mixture Fraction of Mixing Pot Case.....	67
Figure 4-14. TKE in Mixing Pot Case	68
Figure 4-15. PDF Comparisons Between Baseline and Mixing Pot Cases	68
Figure 4-16. Mesh Use In Forward 4° Angle of Inclination Case.....	69

Figure 4-17. Mesh Use In Forward 11° Angle of Inclination Case.....	69
Figure 4-18. Mesh Use In Forward 18° Angle of Inclination Case.....	70
Figure 4-19. Mesh Use In Sideways 4° Angle of Inclination Case.....	70
Figure 4-20. Mesh Use In Backward 4° Angle of Inclination Case	71
Figure 4-21. Average Mixture Fraction for Empty, 11°, and 18° Cases (Front).....	72
Figure 4-22. Average Mixture Fraction for Empty, 11°, and 18° Cases (Side).....	73
Figure 4-23. TKE in Empty, 11°, and 18° Cases	74
Figure 4-24. TKE and Vortex Formation in Empty, 11°, and 18° Cases	75
Figure 4-25. RMS Mixture Fraction in Empty, 11°, and 18° Cases (Front)	76
Figure 4-26. RMS Mixture Fraction in Empty, 11°, and 18° Cases (Side)	77
Figure 4-27. Average Mixture Fraction in 4° Backward and Sideways Cases (Front).....	78
Figure 4-28. Average Mixture Fraction in 4° Backward and Sideways Cases (Side).....	79
Figure 4-29. TKE in 4° Backward and Sideways Cases.....	80
Figure 4-30. TKE and Vortex Formation in 4° Backward and Sideways Cases	81
Figure 4-31. RMS Mixture Fraction in 4° Backward and Sideways Cases (Front)	82
Figure 4-32. RMS Mixture Fraction in 4° Backward and Sideways Cases (Side)	83
Figure 4-33. PDF Comparisons for Baseline and Empty Chamber Cases	84
Figure 4-34. PDF Comparisons for Cases with Varying Angles of Inclination	84
Figure 4-35. PDF Comparisons for Cases with Varying Directions.....	85
Figure 5-1. Burn Rate for Red Oak, Cherry and Pine	92
Figure 5-2. O ₂ Mole Fraction	93
Figure 5-3. CO and NO Mole Fraction	93
Figure 5-4. H ₂ O and CO ₂ Mole Fraction.....	94
Figure 5-5. Calculated Hydrogen:Oxygen Ratio During Burn	94
Figure 5-6. Comparison of Atomic Ratios	95
Figure 5-7. Comparison of Higher Heating Value	95
Figure 5-8. Comparison of Real Time Efficiency.....	96
Figure 6-1. Schematic of Water Vapor Dilution Experiment.....	109
Figure 6-2. Oxygen Concentrations Comparisons	109
Figure 6-3. Higher Temperature Oxygen Comparison Case.....	110
Figure 6-4. Experimental Schematic and RTFBRM	111
Figure 6-5. Comparison of Mass, Burn Rate, and Air Flow Rate	112
Figure 6-6. Comparison of O ₂ , CO, and NO.....	113
Figure 6-7. TDLAS Schematic.....	113
Figure 6-8. Chi-Squared Surface and Comparison of Raw Data with Best Fit Simulation.....	114
Figure 6-9. Comparison of Variable Fuel and Constant Fuel Formulations with TDLAS for CO ₂	114
Figure 6-10. Comparison of Variable Fuel and Constant Fuel Formulations with TDLAS for H ₂ O	115
Figure 6-11. Atomic Ratio for H, O, and N	116
Figure 6-12. Comparison of Variable Fuel HHV.....	117
Figure 6-13. Summary of Thermal Heat Rates	118
Figure 6-14. Instantaneous Real Time Thermal Efficiency Comparison.....	118

List of Tables

Table 2.1. Summary of Parameters for System Level Model	36
Table 4.1. Comparison of Total Emissions With and Without Mixing Pot [%wt]	56
Table 4.2. Summary of Statistics Across All Simulations	56
Table 4.3. Summary of Mixture Fractions at Peak Probability	56
Table 5.1. Total Emissions for Runs with Red Oak, Cherry and Pine [%wt]	92

Acronyms and Abbreviations

<i>bb</i>	BIOBLOCK®
<i>h</i>	heat transfer coefficient
<i>h_i</i>	enthalpy [<i>MJ/kg</i>]
<i>Δh</i>	heat [<i>MJ/kg</i>]
<i>lbm</i>	pounds mass
<i>m</i>	mass [<i>kg</i>]
<i>ṁ</i>	mass flow rate [<i>kg/s</i>]
<i>ṁ''</i>	mass flux [<i>kg/m² - s</i>]
<i>p</i>	pressure [<i>Pa</i>]
<i>t</i>	time [<i>hr</i>] or [<i>sec</i>]
<i>A</i>	area [<i>m²</i>]
<i>C</i>	heat capacity [<i>J/kg - K</i>]
<i>Da</i>	Damköhler number
FBR	fuel burn rate
FGM	flamelet-generated manifold
<i>G</i>	Gibbs free energy [<i>kJ/kg</i>]
<i>H</i>	total enthalpy [<i>kJ/kg</i>]
<i>L</i>	latent heat [<i>MJ/kg</i>]
<i>Le</i>	Lewis Number
<i>M</i>	normalized mass
<i>Pr</i>	Prandtl Number
NYS	New York State
NYSERDA	New York State Energy Research and Development Authority
<i>Q</i>	heat [<i>J</i>]
<i>Q̇</i>	heat rate [<i>W</i>]

RTFBRM	real time fuel burn rate monitor
S	entropy [kJ/K]
Sc	Schmidt Number
T	temperature [K]
UFGM	unsteady flamelet-generated manifold
W	watts
WFHH	wood-fired hydronic heater
Y	species mass fraction
Z	mixture fraction

Greek

α	sensitivity number
ρ	density [kg/m^3]
τ	normalized time
ϕ	equivalence ratio
σ	Stefan-Boltzmann constant [$W/m^2 - K^4$]
χ	scalar dissipation rate [$1/s$]
Δ	$\Delta F = \int \dot{F} dt$

Subscript/Superscript

<i>air</i>	air
<i>b</i>	boiler
<i>c</i>	constant
<i>comb</i>	combustion
<i>del</i>	delivered
<i>f</i>	fuel
<i>fg</i>	fuel to gas
<i>flue</i>	flue
<i>g</i>	gas
<i>gb</i>	gas to boiler
<i>i</i>	i^{th} species
<i>in</i>	in
<i>n</i>	n^{th} term
<i>o</i>	initial
<i>out</i>	out

<i>p</i>	pyrolysis
<i>peak</i>	peak, where $-\dot{m}_f$ is maximum
<i>s</i>	steel
<i>st</i>	stoichiometric limit
<i>stor</i>	storage
<i>th</i>	thermal
<i>w</i>	water
∞	ambient/far-field conditions

Executive Summary

This study has been supported by the New York State Energy Research and Development Authority (NYSERDA) to help with R&D efforts for batch run wood-fired systems used for hydronic heating applications. The focus being on the exploration of efficiency and emissions of a locally developed appliance made by Econoburn (Brocton, NY). The Econoburn boiler was installed in the UB Combustion laboratory and instrumented using several diagnostics that included: low-cost flue gas measurements, a newly developed real time fuel burn rate monitor (RTFBRM), an air flow rate monitor, water mass flow rate meters, and several thermocouples measuring both gas and water temperature flowing in and out of the boiler. The research was centered on two main areas: 1) accurate and reliable measurements of flue gas emissions using relatively low-costs sensors and 2) computational models for predicating boiler performance. The major contributions from the three-year study are: 1) a novel water-vapor correction method for improving the accuracy of flue measurements, 2) a new flue gas interface methodology that takes into account the non-homogeneous decomposition of biomass and 3) new CFD modeling tools to predict the effects of secondary burning in two-stage boilers. Further details on each of these three major contributions are summarized below.

Current flue emission technologies for residential boilers typically rely on low-cost sensor technologies and instrumentation. Many of these technologies are *in-situ* based where a sample is drawn through a system of tubes to reach the sensor at a remote location (prominent analyzer manufacturers are: Testo, Wohler, Land, *etc.*). Since water vapor is inevitably present in combustion products, an inherent characteristic with the gas sampling strategy is that the mixture changes as the sample is drawn towards the sensor and cooled. In particular, temperature and humidity changes can be significant, causing condensation, and resulting in a very different gas mixture at the sensor interface compared to the conditions in the flue. One of the contributions from this effort is developing a correction method to account for water vapor condensation in the sampling line using a secondary heated Bosch LSU 4.9 wide-band oxygen sensor in the flue. The secondary oxygen measurement allows for accurate measurements of CO and NO in the flue via the novel correction method. The details of this new approach are detailed in Ref. [1].

With the corrected flue gas measurements of CO, NO and O₂, a measurement of wood moisture content, and assuming a known constant chemical composition of the wood, then major species of combustion, CO₂ and H₂O can be determined from a chemical balance interface. Accurate determination of these species is vitally important for modeling validation and boiler design since the levels of CO₂ and H₂O largely determine the extent of reaction and overall combustion efficiency of the boiler. Preliminary comparisons

of experimental measurements using a constant fuel (CFF) chemical interface method resulted in unacceptable differences between modeling predictions and measurements. It was found that the source of these differences was largely due to the non-homogeneous decomposition of the fuel violating the CFF assumption. A variable fuel formulation (VFF) was therefore developed and detailed in Refs. [2, 3]. The new VFF methodology was validated by new independent measurements of CO₂ and H₂O using tunable diode laser absorption spectroscopy (TDLAS) showing good overall agreement. Furthermore, the data interpreted through the VFF agreed much better with modeling predictions, demonstrating the importance for accounting for the non-homogeneous fuel decomposition in combustion modeling.

The third major contribution of this study was the development of new CFD tools for the design and understanding of next generation boilers. As with most CFD combustion modeling, explicit resolution of flame structure is not possible due to the wide range of length and time scales of the problem. A subgrid scale (SGS) model is therefore required. The SGS modeling methodology developed in this research was based on the use of flamelet generated manifolds (FGM). The appeal of the FGM modeling approach is it allows for the inclusion of complex chemistry into the description of the SGS combustion processes. Exploration of existing FGM SGS models revealed them unsuitable for biomass combustion because important surface blowing effects are omitted in their formulation. A new FGM modeling methodology was therefore developed to include the effects of surface blowing and validated against exact solutions. The details of this new approach are detailed in Refs. [4-6]. System level and detailed CFD SGS models using the new FGM approach were developed and implemented for prediction of flue gas emissions showing good overall agreement. Finally, the CFD tools are used to explore design perturbations to the existing geometry of the lower chamber of the Econoburn boiler. CFD results show that improved mixing can be achieved with simple changes to the lower mixing chamber and were verified with experimental testing.

The rest of this document is organized as follows. Each chapter is dedicated to the tasks planned for this project. In Chapter 1 the boiler installation and baseline testing is outlined. In Chapter 2 the numerical modeling is discussed with the development of an analytical mass loss theory. In Chapter 3 the emissions reduction design is presented, outlining the mixing pot device. In Chapter 4 fuel sensitivity is explored by comparing measurements of BIOBLOCK (red oak), cherry cord wood, and pine 2x4s. Finally, in Chapter 5 a discussion for improving and correcting emissions measurements is presented. For ease of interpretation, each chapter is written as a self-contained unit, with appropriate introduction, results, discussion, and conclusion sections.

1 Boiler Installation and Baseline Testing

1.1 Real Time Fuel Burn Rate Monitor (RTFBRM)

1.1.1 Conventional Approach: Weigh Entire Boiler

Certification testing of wood burning boilers includes an assessment of real time fuel burn rate. A common approach is to instantaneously measure the total weight of the boiler, with fuel burning in the combustion chamber, and then monitor the total weight change to infer the time rate of change of the mass of the fuel [7, 8] This is an indirect way to assess the burn rate; and, the effects of the plumbing connections, electrical connections and exhaust flue connections raise questions about overall accuracy. Questions also arise regarding the resolution of the system. The maximum load of fuel is about 60 pounds, which is only about 3% of the loaded boiler (~2000 pounds). This not only makes it difficult to detect minute mass changes, but also even small force loading fluctuations in the boiler could significantly affect the inferred burn rate. This could help explain why (impossible) negative burn rates are sometimes observed.

1.1.2 New Approach: Real time fuel burn rate monitor design

1.1.2.1 Concept

In order to eliminate the effects of the plumbing connections, electrical connections, and exhaust flue connections on the fuel mass measurement, a more direct method is described here. This approach involved considerable design challenges and these details will be described in the following section.

1.1.2.2 System Design

The main concept of our real time fuel burn rate monitor is to directly weigh the fuel (only) while it is decomposing from pyrolysis and combustion processes. Measurements are taken by loading the fuel in a hanging basket, which is located inside the primary combustion chamber. The mass of the basket and fuel is then monitored using a National Institute of Standard and Technology (NIST) calibrated load cell, output that is collected via a data acquisition system (DAQ system) and LabVIEW software. Data is then post processed as needed. A schematic of the arrangement is shown in Figure 1-1.

1.1.3 Components

1.1.3.1 Load Cell, Load Cell Base, and Load Cell Mount

The load cell used in this design is a Stellar Technology Inc. (STI) series PNC710. The range of this load cell is 0-100 lbs., with about 3mV/V full scale output (FSO). The specific load cell (serial number 1210147) used in this system was provided with a factory calibration of 3.038 mV/V FSO with an end point linearity of 0.070% FSO.

Since the manufacturer's specified maximum working temperature of the load cell is 400°F, the load cell could not be mounted directly inside the combustion chamber. Also, the effect of smoke and other combustion residue would be detrimental to the load cell. To avoid these complications, the load cell was mounted on the outside top of the boiler. The weight of the hanging basket is transferred to the load cell by means of the low friction sliding rods and pivotable cross members shown in Figure 1-1. To compensate for the rod off-axis loading due to unavoidable fuel shifting during burning, a hemispherical head (with a 0.313 inch radius) is mounted on the load cell, to provide a continuous point of contact between the upper cross member and the load cell. This eliminates possible torque applied to the load cell, which is not desirable for optimal operation.

As specified by the manufacturer, in order to yield the best performance, the load cell should be mounted on a secure platform which is free from drastic temperature change. This was a potential challenge to the installation. The load cell was mounted to a base provided by the manufacturer, which ensures an even load distribution at the bottom of the load cell. To achieve a secure mounting for accurate reading, the load cell base needed to be directly mounted onto the boiler, however, heat from the boiler plate would have an undesirable effect on the load cell reading, especially during the transient heating and cooling of the boiler.

To address this issue, an insulated platform was designed. It consists of a top plate, an intermediate plate and a tube spacer. The load cell was mounted on the top plate, which was connected to the intermediate plate by the tube spacer. The intermediate plate, see Figure 1-2, has been relieved of excess material as much as possible, in order to minimize thermal conduction from the stay to the rest of the platform. The intermediate plate was fastened to the boiler using a tapped hole in a central top stay (see Figure 1-1). All of these components were encased in a stainless tube (tube spacer) shown in Figure 1-2. Stainless steel was used because its thermal conductivity is considerably less than that of steel, and it has the additional advantage of being corrosion resistant. In addition, the air space in the cavity was filled with the same fiberglass insulation as that used to insulate the boiler. The top plate is held with four screws, which allow

easy removal, during installation and easy removal in the event of an emergency. Figure 1-3 shows an assembled load cell mount with the boiler insulation replaced, prior to installation of the load cell.

To prevent an accidental high impact load, a safety collar was added around the load cell. The load cell is accessible for measurement when the upper cross member is in line with the undercuts made into the collar. In “safe” mode, the upper cross member is blocked from contact with the load cell by the safety collar. A photo of the configuration of the safety collar is shown in Figure 1-4. With this design, the safety collar can be easily activated by means of twisting the collar. The procedure for activating and deactivating the safety collar was integrated into the operating protocol of the boiler.

1.1.3.2 Sliding Rods

Based on an optimal combination of strength, rigidity, and available space in a boiler stay, two 0.25 inch diameter ground rods were selected as sliding rods, for their tight tolerance and smooth surface finish.

One unique challenge for the RTFBRM design is to penetrate through the water jacket without leaking water. The water jacket is a layer of water surrounding the primary and secondary combustion chambers. With very careful drilling, the stays were exploited as a leak proof barrier allowing us to penetrate the water jacket without leakage. The stays are steel rods welded between the inner and outer boilerplates to provide structure support for the water jacket, especially under thermal stress. They are 0.75 inches in diameter and 3 inches long. Using a magnetic base drill press and extreme care, two boiler stays were successfully drilled through. The arrangement is shown in Figure 1-5.

To obtain a smoke-tight seal between the hole in the stays and sliding rods, Swagelok fittings were modified as packed fittings. A self-centering washer was made, along with the Swagelok fitting itself, to contain graphite filled carbon fiber yarn packing material. The tightness of the packing material is adjustable by turning the locking nut screwed onto the fitting, which allowed a balance between minimum friction and a smoke-tight seal.

1.1.3.3 Hanging Basket

The horizontal dimensions of the hanging basket (installed inside the primary combustion chamber) are 15 inches by 18.75 inches. The hanging basket frame was constructed using welded 1x1x3/16 angle iron, and an expanded sheet metal bottom. The basic structure of the hanging basket and its assembled view is shown in Figure 1-6 and Figure 1-7. The clearance, nominally 1 inch allows adequate air circulation through and around the basket, and minimum flame distortion. Preliminary testing revealed that containment walls were

needed on the basket to prevent the fuel from hitting the sidewalls of the combustion chamber. Steel rods 3/16 inch in diameter, spaced 2.25 inches apart were added to the sides of the basket, to prevent fuel from falling onto the boiler sides, while additionally, minimizing radiative interference from the burning fuel to the combustion chamber walls.

The hanging basket was connected to a lower cross member, which is linked to the upper cross member by means of the sliding rods. The system is designed to automatically adjust, level and center itself to compensate for inevitable imbalances from the burning process. This is achieved by adding slotted holes and sliding rods to both the lower and upper cross member supports.

The basket was also designed to hold approximately 64 lbs. of SWI BIO BLOCK® fuel. This fuel was chosen due to its consistent weight (2 lbs.) and moisture content (~ 8%).

1.1.3.4 Lift System for Lifting and Lowering Basket

For ease of loading fuel into the hanging basket, a lifting device was developed and installed on top of the boiler. The lift system consists of a gantry constructed from structural steel, a precision positioning winch, two pulleys, 3/16-inch cable and a hook (see Figure 1-8).

The gantry provided a solid frame that holds the weight of fuel and hanging basket. It is connected directly to the top of the boiler to ensure strong structural support.

The winch, pulley and cable operate together transforming the operator's winding motion to the vertical motion of the hanging basket. A precision positioning winch has been used here to allow the operator to accurately position the basket.

The upper cross member is connected to the lift system via a hook bent from ¼ inch diameter steel rods. The hook is detachable and does not remain connected when the system is in operation. This will prevent possible interference and resultant error in measured data introduced by the lift system.

1.1.4 General Operation of RTFBRM

The RTFBRM operates by accurately measuring the mass of the basket and its contents over the entire duration of any particular boiler burn. An operating protocol has been prescribed to ensure the optimal function of the RTFBRM during a run, consisting of the following steps:

- Before any burn a clean set of sliding rods is installed. The old rods, contaminated from the combustion residue, are cleaned with industrial grade Scotch-Brite™ and solvent.
- The high temperature graphite filled carbon fiber yarn packing material within the stays is checked and replaced if necessary.
- Verification of free-and-clear support rod travel
- The basket is raised and loaded with the desired amount of fuel (paper, kindling, BIO BLOCKS®), in a prescribed pattern.
- The paper and kindling is ignited in two locations.
- The basket is immediately lowered carefully, while the safety collar is rotated to the “measure” position before the upper cross member rests onto the load cell.

These steps initialized the RTFBRM. During the course of the burn, the boiler is operated at the manufacturer’s suggested set points with the RTFBRM remaining uninterrupted by outside influence until reaching both an internal water temperature (~120-130 °F or below) and a fuel mass (1-2 lbm or below) indicating nearly complete fuel consumption.

1.1.5 Results

Comparisons of the University at Buffalo (UB) mass data (RTFBRM) to the Brookhaven National Laboratory (BNL) mass data (full boiler mass measurement method) are presented. The fuel load for the UB data was 16 BIOBLOCKS® (~ 8.3% dry-basis moisture), approximately 32 lbm of wood fuel which is considered a half load compare with the maximum capacity suggested by the boiler manufacturer. The duration of burn for 16 BIOBLOCKS® was approximately 2 hours and 18 minutes, with testing terminated when only small pieces of smoldering coal were left in the basket and based on the criterion mentioned in the previous section. Results of the RTFBRM show a mean and maximum fuel consumption rate of 13.3 lbm/hr and 27.5 lbm/hr, respectively. Figure 1-9(a) and Figure 1-9(b) show the mass and rate of mass loss vs. real time for both UB’s half load BIOBLOCK® run and BNL’s full load cord wood run, respectively. The BNL test took approximately 3 hours and 12 minutes to reach a minimal remaining mass. It is important to note that the presented BNL data has been extracted from their report [9] and is a representation of their overall fuel mass trend. The actual raw data includes several outlier data points that were not captured in the representation shown in Figure 1-9(a) and Figure 1-10(a). Each set of mass data was differentiated using a global fifth order polynomial curve fit to find the rate of mass loss. Figure 1-9(a) shows the compared UB and BNL trend for the rate of mass loss. The BNL data shows a similar trend with a mean and maximum fuel consumption rate of 18.1 lbm/hr and 32.1 lbm/hr, respectively. Since the loads and burn durations of the two data sets are different, normalized mass and time measures were developed.

Figure 1-10(a) shows the instantaneous normalized fuel mass vs. time for the UB RTFBRM and the BNL mass measurements. The normalized mass is defined as the mass divided by the initial mass. Normalized time is defined as the time divided by the time at the peak rate of mass loss. Normalized mass loss rate is defined as the mass loss rate divided by the peak mass loss rate. Both qualitative and quantitative agreement between the UB and BNL data is quite good using the normalized scaling. This scaling has the potential of reducing data for a given boiler for different fuels, initial loading, and measurement methods. This scaling will be further explored in the future.

From the analysis of the mass loss trend and, in particular the rate of mass loss, it is possible to derive additional details of the boiler process. For example, instantaneous energy release rates can be calculated and plotted as a function of time. These trends, which can be plotted for various fuels, show the amount of energy released at any moment during a burn based on the mass burn rate and the higher or lower heating value (HHV, LHV) of the fuel. For the purpose of our research, the LHV was chosen as it neglects the heat recovered when water vapor condenses. This assumption is based primarily on the fact that the combustion gasses are very hot and condensation is not likely to happen until reaching a considerable distance through the flue stack, beyond our range of analysis. Figure 1-11, presents the instantaneous energy release rates assuming five values of heating values corresponding to several types of common wood fuels with different moisture contents, as well as methane. The exact heating value of the BIOBLOCKS[®] is not precisely known but is expected to be close to that of wood chips. As shown, the peak instantaneous energy release corresponding to the maximum mass loss rate of the fuel. The time of the peaks likely also corresponds to the point in time when the fuel flame area is greatest indicating the largest heat input into the boiler/water system.

Figure 1-11 also contains a table showing the integrated energy released over the entire burn. This value is derived from the instantaneous energy release curves by numerically integrating the energy input to the boiler over the entire duration of a burn. These values represent the total energy input into the system for the various fuels. Knowing the total energy input into the boiler system will be an essential consideration when calculating the boiler's efficiency. Comparing these values to those found in the BNL certification testing report [9], BNL reports approximately 450,000 BTU energy input. The values reported in Figure 1-11 are within range given the difference in burn duration and fuel load.

1.1.6 Conclusions

A RTFBRM has been successfully constructed, installed, and tested. It has been intentionally designed to minimize functional interference of typical boiler operation. The results of the RTFBRM show a monotonic

decrease in fuel mass leading to reliable estimates of mass loss rate. Preliminary results of the RTFBRM show a working concept that has been developed with National Institute of Standard and Technology traceable calibrations of instruments. Proper operating and safety protocols have been enacted to ensure consistent and repeatable measurements as well as adequate protection of the sensitive instruments and their operators. In the future, possible improvements or modifications to the design will be ongoing as issues may develop but the current overall design has shown to be effective for its engineered purpose.

1.2 Baseline Testing of Boiler and Monitoring Equipment

1.2.7 Introduction

The Environmental Protection Agency (EPA) has defined specific regulations in the New Source Performance Standard (NSPS) for wood burning appliances including wood stoves, masonry heaters, pellet-burning heaters, and hydronic heaters. These regulations will require the manufacturer to have their unit tested at an EPA accredited testing facility. The EPA regulation limits are based on the best-of-class, demonstrated technology found at the time. However, to identify the best, an accurate and repeatable procedure must be defined for performance characterization. The original Method 28 for Outdoor Wood-burning Hydronic Heaters (OWHH) was developed for this purpose. Performance characterization of any wood burning hydronic heater requires accurate monitoring of the fuel loss, inlet and outlet temperatures of any working fluid, and emissions measurements from the exhaust. With these measurements comes a vast array of unknowns and assumptions that must therefore be made when characterizing systems performance.

The original NSPS included standards for boiler performance, of which the revised EPA Method 28 WHH defined an operating protocol for testing boiler emissions and their delivered efficiency (the heat delivered through a heat exchanger divided by the net fuel heat input). In Method 28, four test categories were described based on running the boiler in specified heat output ranges: Cat. I – boiler is run at a heat output of 15% or less of the manufacturer's rated heat output capacity, Cat. II – heat output of 16% to 24% of the manufacturer's rated heat output capacity, Cat. III – heat output of 25% to 50% of the manufacturer's rated heat output capacity, and Cat. IV – heat output of the manufacturer's rated heat output capacity. To implement these categories the heat exchanger limits the amount of heat removed from the boiler hot water, resulting in the boiler control reaching peak water temperature and turning off the blower feeding the primary combustion chamber. This halting of the blower significantly reduces combustion efficiency and increases burn time. Brookhaven National Laboratory submitted a letter to the EPA proposing a major modification of the Method 28 procedure, where thermal storage is used in the testing (as it would in a

residential system) so that the boiler can run at full output, steady-state (and therefore its highest efficiency) while charging the thermal storage tank. The testing categories still apply in the sense that the heat is removed from the thermal storage tank at the specified category rates. This simple modification has the advantage of allowing the boiler to run at high-burn-rates, avoiding water overheating and a high emission, slow-burn state.

There are few published studies pertaining directly to the testing of domestic wood fuel gasification boiler systems. This study introduces a novel method of solid fuel mass monitoring, and uses industry standards for temperature, mass, and emissions measurements. In section 1.2.8, the methods of the experiment are presented with all major components detailed. Section 1.2.9 presents a description of the efficiency definitions used. Finally, section 1.2.10, presents results and discussions of the data and calculations, which prove to be comparable to similar tests by accredited and national laboratories.

1.2.8 Experimental Methods

A testing facility was designed for the Econoburn EBW-200 wood-burning hydronic gasification boiler. The first component was detailed in the previous task report for the real time fuel burn rate monitor as a way to monitor in real time the fuel mass while isolating that measurement from outside interference. Real time temperatures are recorded at all water inlets and outlets for determination of heat losses using National Instruments data acquisition equipment and software. Additionally, exhaust flue emissions variables (exhaust temperature, CO₂, O₂, CO, NO, NO_x) are recorded to help understand the combustion characteristics and combustion efficiencies. A Testo 330-2 LL meter is used for this purpose with readings taken at 1 Hz. Other data acquisition is recorded at 2 Hz frequency. Figure 1-12 shows a schematic of the full experimental setup, representing the major components of the facility and the necessary constituents to characterize general boiler performance.

The experimental set-up has been designed to easily and accurately measure real time fuel mass (detailed in section 1.1). Measurements of water inlet and outlet temperatures are taken using Omega type J transition joint thermocouple probes with a stainless steel sheath (TJ144-CASS-116U-6). The location of all major experimental components are shown in Figure 1-12 below. There are two water flow loops that are used. The first when pump 1 (P1) is on and pump 2 (P2) is off circulates the hot water through the boiler until the water temperature reaches 150°F. The second loop where P2 is on and P1 is off, is the load loop where the heat is allowed to transfer to the cold city water via the heat exchanger. The heat rate is monitored by recording the water inlet and outlet temperatures as well as the water flow rates, providing a detailed trend

of the boiler supplied heat load. This trend can be integrated over the full duration of the burn to find the total heat delivered to the water (discussed in the following section).

Testing of the boiler is conducted using strict protocols to ensure the safety of students and reduce run-to-run variations of measurement noise. To summarize the testing procedure, laboratory exhaust fans are turned off and doors closed to allow sufficient flue draft. Data acquisition instruments are turned on, including the emissions probe. The RTFBRM hanging basket rods are cleaned and replaced if necessary, and the viewing windows are cleaned. Wood kindling, newspaper and BIOBLOCKS[®] are carefully placed into the basket for the initial cold start run. The BIOBLOCKS[®] arrangement in the basket follows the procedure visualized in Figure 1-13. The Testo gas analyzer (330-2 LL) is placed in the flue stack approximately 3 feet from the back of the boiler. Data acquisition is initialized and the newspaper/kindling is ignited with a propane torch. As the water temperature and flue temperature begin to rise the damper is left open until a draft can be sustained (reaching approximately 300°F, read by the Testo meter) the burn concludes when the water temperature, stack temperature, and fuel mass all indicate a completed burn. As defined in the previous section: fuel mass reaches 1-2 lbs or below, the internal water temperature is approximately 125°F, and (recently added) flue gas temperature falls below 150°F. Modifications are continuously made as improved methods are discovered.

1.2.9 Performance Characterization: Efficiency Definitions

There are numerous ways in which efficiency can be described. Given the various types of efficiency and definitions used, Nussbaumer & Good 1998 [10], described a method for the determination of combustion efficiency in biomass furnaces which aimed to make transparent all assumptions and details of the derivation. Nussbaumer's method uses the flue gas composition to calculate the chemical and thermal losses contained in the exhaust. Similar to the method presented in CAN/CSA B415.1-92 [11] and CAN/CSA B415.1-10 [12] however Nussbaumer neglects hydrocarbon production and soot, an assumption that ideally makes sense given the secondary gasification chamber's purpose of burning the volatiles initially produced by the biomass combustion in the primary chamber.

The boiler's thermal efficiency (η_{th}) is defined as the ratio of the heat rate delivered from the boiler divided by the amount of heat produced by the solid fuel combustion. This is the basic definition described in Method 28 as the delivered efficiency and the definition used by Kang *et al.* 2013 [13] in their development of a wood-pellet boiler performance test facility.

Prior definitions lack a full description of many of the transfer processes that take place in a boiler, to fully define the boiler's thermal efficiency. The two internal transfer processes describe the combustion and heat transfer within the boiler, bridging the divide between what is commonly referred to as the direct (thermal efficiency, η_{th}) and indirect (stack loss efficiency, η_{SL}) methods for characterizing boiler efficiency.

The combustion efficiency (η_{comb}), physically representing the degree to which the combustion of the fuel approaches complete combustion, is stated in Equation 1-1. The heat transfer efficiency (η_{ht}) represents the degree to which available heat transfers to the water, stated in Equation 1-2.

$$\text{Equation 1-1} \quad \eta_{comb} = \frac{\dot{Q}_{comb}}{\dot{Q}_{comb,max}}$$

$$\text{Equation 1-2} \quad \eta_{ht} = \frac{\dot{Q}_{del}}{\dot{Q}_{av}}$$

where,

$$\text{Equation 1-3} \quad \dot{Q}_{av} = \dot{Q}_{comb} - \dot{Q}_{stack}$$

$$\text{Equation 1-4} \quad \dot{Q}_{del} = \dot{m}_w C_{p,w} (T_{b,o} - T_{b,i})$$

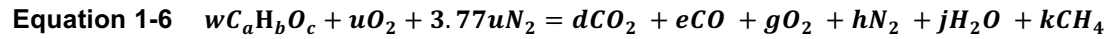
$$\text{Equation 1-5} \quad \dot{Q}_{comb,max} = \dot{m}_f CV$$

The value CV defines either the net or gross calorific value, where net calorific value (NCV) is the amount of heat released during the combustion of a specified amount of that substance neglecting the energy lost by the state change of water vapor. Gross calorific value (GCV) is defined similarly however additionally assuming the energy in the water vapor returns to its liquid state, thereby reclaiming the latent heat from the water vapor. The time dependent variables \dot{m}_f and \dot{m}_w are the rate of mass flow for the solid fuel and the boiler water respectively. The heat capacity ($C_{p,w}$) and inlet ($T_{b,i}$) and outlet ($T_{b,o}$) water temperatures are used to determine the delivered heat rate from the boiler. It is also possible to use the emissions data to approximate the heat loss from the exhaust gasses.

Determining boiler efficiency using the rate of heat loss through the flue is known as the stack loss method (SLM) and can be directly related to the thermal efficiency when taking the internal transfer processes into account. The stack loss efficiency uses the heat lost from the exhaust to determine the heat transferred to the water. The version of the stack loss method most commonly referenced and used by BNL is that of CAN/CSA B415.1-10 (assumed identical to CAN/CSA B415.1-92 [11] used for this study). To calculate

this efficiency, it is important to have an accurate approximation of the chemical species contained in the combustion products, i.e. emissions variables. Given the vast array of configurations for exhaust species concentrations, which depend on the boiler, fuel, moisture content...etc., many variations of the same method exist.

The SLM takes as input, the flue temperature, ambient air temperature, O₂%, CO₂%, CO%, mass change, and moisture content information. Using the chemical balance shown below in Equation 1-6 it approximates the sensible and latent heat losses associated with each product species including that contained in the fuel moisture content. By summing the total losses from each species over a 10 minute averaged time block and knowing the mass of fuel consumed over that time, the stack loss efficiency (η_{SL}) is defined as Equation 1-8.



$$\text{Equation 1-7 } \dot{Q}_{stack} = \Delta m_{f,10min} \left[\sum_{i=1}^7 \dot{n}_i (h_{i,T_{stack}} - h_{i,T_{amb}}) + \dot{n}_{CO} \Delta h_{CO,comb} + \dot{n}_{H_2O} \Delta h_v + \dot{n}_{CH_4} \Delta h_{CH_4,comb} \right]$$

$$\text{Equation 1-8 } \eta_{SL} = 1 - \frac{\dot{Q}_{stack}}{\dot{Q}_{comb}} = \frac{\dot{Q}_{av}}{\dot{Q}_{comb}}$$

The coefficients a, b, c describe the fraction of atoms in the fuel components. Coefficients w, u, d, e, g, h, j, k represent the moles of that species per 100 moles of dry flue gas, or molar fraction. The change in dry fuel mass for that 10 minute interval is defined as $\Delta m_{f,10min}$, the molar flow rate per species is \dot{n}_i . Species enthalpy at stack temperature ($h_{i,T_{stack}}$), species enthalpy at ambient temperature ($h_{i,T_{amb}}$), the latent heats for carbon monoxide, water, and methane ($\Delta h_{CO,comb}, \Delta h_v$, and $\Delta h_{CH_4,comb}$) respectively, define the method.

Finally, it can be shown that the thermal efficiency (η_{th}), see Equation 1-9, equals the stack loss efficiency (η_{SL}), provided, the combustion (η_{comb}) and heat transfer (η_{ht}) efficiencies are unity.

Equation 1-9
$$\eta_{th} = \frac{\dot{Q}_{av}}{\dot{Q}_{comb}} \frac{\dot{Q}_{del}}{\dot{Q}_{av}} \frac{\dot{Q}_{comb}}{\dot{Q}_{comb,max}} = \eta_{sl}\eta_{ht}\eta_{comb} = \frac{\dot{Q}_{del}}{\dot{Q}_{comb,max}}$$

This relation provides a quantifiable method of characterizing the major processes and overall boiler efficiency.

It should be noted, an augmented thermal efficiency ($\eta_{th,BNL}$) has been defined by BNL [7] that attempts to account for the additional heat stored within the boiler steel and water, and the thermal storage tank (for the category I test). For the efficiencies reported in this document, heat storage is not accounted for since these quantities do not lend themselves to be easily calculated in real time due to uncertainties in temperature distribution within the boiler. The augmented thermal efficiencies for these tests are reported in the results section and are comparable to those calculated by BNL.

1.2.9.1 Emissions Measuring

During run time the Testo probe is placed within the flue gas for the entirety of the run allowing for the capture of emissions during three important phases: startup, peak-performance, and cool-down. During startup, the emissions of CO are at their peak as the fuel is ignited and temperatures are relatively low. As the boiler heats up and transitions into its peak-performance stage, which corresponds to the hottest part of the run, CO emissions decrease and NO and NO_x emissions increase due to the increase in temperature. Finally, as the boiler cools due to the lack of additional fuel, NO and NO_x emissions begin to drop and CO emissions come up slightly. It is important to include all emissions during the three different run time stages in order to obtain an overall understanding of the emission footprints of gasification wood boilers.

1.2.10 Results and Discussion

1.2.10.1 Fuel Mass Monitoring

Mass loss rate in solid fuel biomass boiler can be a difficult metric to monitor accurately. Typically a scale is placed under the entire boiler and measured over the course of a burn [7, 8]. A potential downside of this approach is that plumbing, electrical, exhaust connections, and scale resolution may cause inaccurate measurements and negative burn rates. To alleviate this uncertainty a real time fuel burn rate monitor has been developed. Results from the RTFBRM, shown in Figure 1-14, clearly demonstrate a monotonic decrease in mass. The results also agree favorably to those from BNL.

Figure 1-14 shows the instantaneous normalized fuel mass vs. time for the UB RTFBRM and the BNL mass measurements. The normalized mass is defined as the mass divided by the initial mass. Normalized time is defined as the time divided by the time at the peak rate of mass loss. Normalized mass loss rate is defined as the mass loss rate divided by the peak mass loss rate. Both qualitative and quantitative agreement between the UB and BNL data is quite good using the normalized scaling. This scaling has the potential of reducing data for a given boiler for different fuels, initial loading, and measurement methods. Currently under analysis, initial results show promise for the development of a closed form analytical expression describing the change in fuel mass with respect to time for a specified set of conditions.

1.2.10.2 Efficiency

Integrated thermal efficiencies have been calculated for a full 32 BIOBLOCK[®] run with a hot start in this facility with the thermal efficiency of $\eta_{th} = 66.5\%$ at GCV and an augmented thermal efficiency of $\eta_{th,BNL} = 61.7\%$ at GCV. Typically, the delivered efficiency would be lower by a small percentage; however, in this case the initial boiler temperature was higher than the final boiler temperature accounting for that discrepancy. For a similar run with cord wood from BNL [9] they calculated a $\eta_{th,BNL} = 57\%$ augmented thermal efficiency. Intertek Labs running under the methods of the original Method 28 OWHH calculated a range of thermal efficiencies from $\eta_{th} = 47\%$ to 72% for categories I through IV for Econoburn's EBW-150 unit, these results show an initial agreement of overall magnitude, to those from accredited and national labs.

Real time efficiencies, possible with the SLM approach, have been calculated for a half load BIOBLOCK[®] run with a cold start. As would be expected with the stack loss method the efficiency is typically higher than overall delivered or total efficiency for a specific run since these combustion efficiencies fail to account for heat transfer and combustion losses other than those from the flue. Figure 1-16 shows a comparison of stack loss efficiencies calculated for a half BIOBLOCK[®] load and a full cord wood load both with a cold start. The time was normalized by the time to peak burn rate as used in Figure 1-15 as described previously. While initial impressions indicate a somewhat incongruous overall trend, differences in fuel and startup procedures could account for the difference. The magnitude of the efficiencies between both cases are acceptably similar and given the load difference the duration at higher efficiencies is consistent with expectations.

1.2.10.3 Emissions

Figure 1-17 shows plots of the Carbon monoxide (CO), oxygen percentage (O₂) and temperature versus time during a boiler run containing 60 lbs. of BIOBLOCKS[®]. A comparison is made to a similar BNL run for a full load cord wood burn with a cold start. It is interesting to note the difference in magnitude of the CO readings with much higher CO for the BIOBLOCKS[®], possibly due to the method of measurement (Testo meter vs dilution tunnel) and the type of fuel used in the burn. The oxygen shows at the beginning of the run to be the expected ~21%, then continues to decrease to a minimum of 6% when the fuel is at its peak burn rate, similarly seen in the BNL data. After peak burn rate is achieved, the oxygen in both cases continue to rise back to the starting 21% concentration. CO has peak values when O₂ content is at its lowest in the beginning of the run. The stack temperature shows a similar trend to that of the burn rate and the magnitude of the stack temperature is proving to be a reasonable gauge of run-to-run burn quality, since higher temperature promotes both reduced emissions and increased heat transfer. Also, comparing the stack temperature to the stack loss efficiencies in Figure 1-16, it is evident that the start-up burn time or the time it takes to reach peak temperature is higher for BIOBLOCKS[®] than it is for cord wood. Leading to the comparison of overall run duration, from the comparison, the UB sample duration is longer than that of BNL, this could be due to several factors, ranging from fuel type or loading procedure, to a difference in criterion for run termination. Regardless of this fact, the data compared to BNL show a similar overall trend for CO, O₂, and stack temperature, providing significant insight into the behavior of the fuel and boiler.

1.2.11 Conclusions

Data measurements of full ~60 lb. loads of BIO BLOCKS[®] for boiler runs of categories I and IV, as defined by the EPA in Method 28 WHH, show clear trends associated with batch runs. Mass loss rate, temperatures, and thermal efficiencies as well as emissions data collection have been measured. Mass loss trends are clearly smooth and show a monotonic decrease as expected. Efficiencies calculated under several methods have been shown to compare well with those calculated at accredited labs and Brookhaven National Lab. Emissions compared with those taken under similar run loads and conditions at BNL show similar overall trends.

Figure 1-1. Schematic of RTFBRM Showing Front and Side View

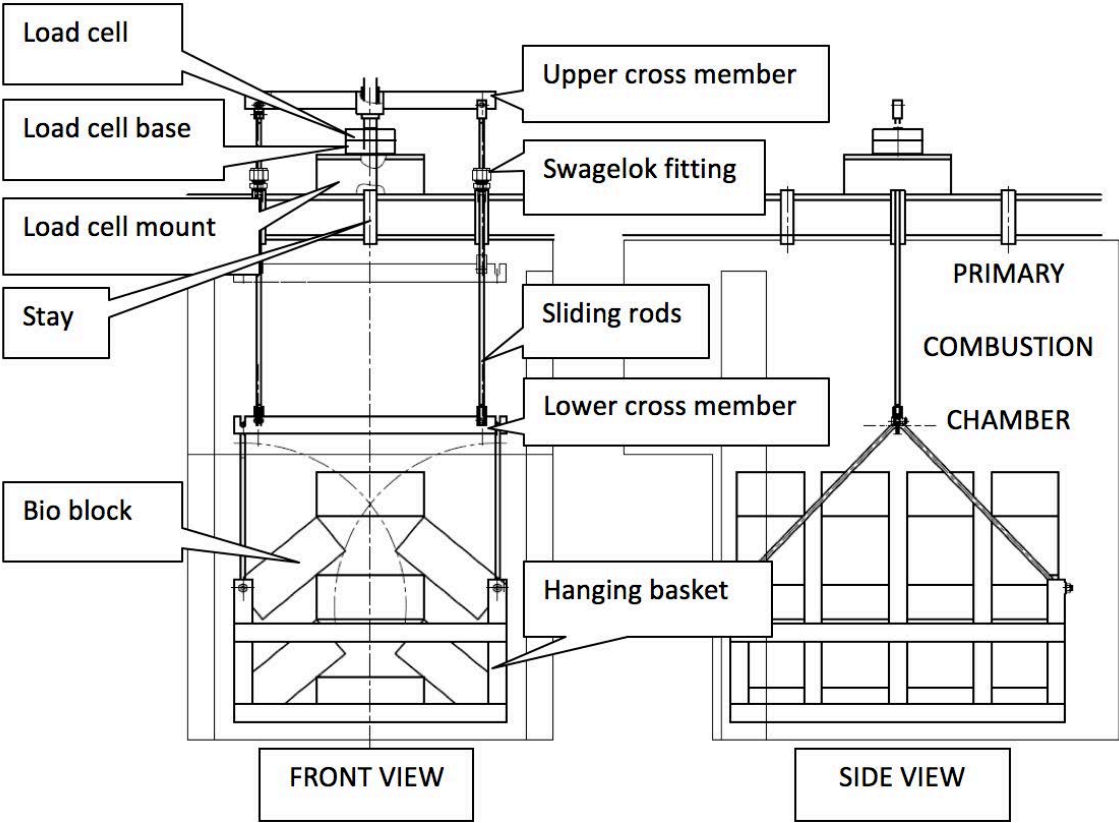


Figure 1-2. Load Cell Mount Showing Intermediate Plate and Tube Spacer without Insulation

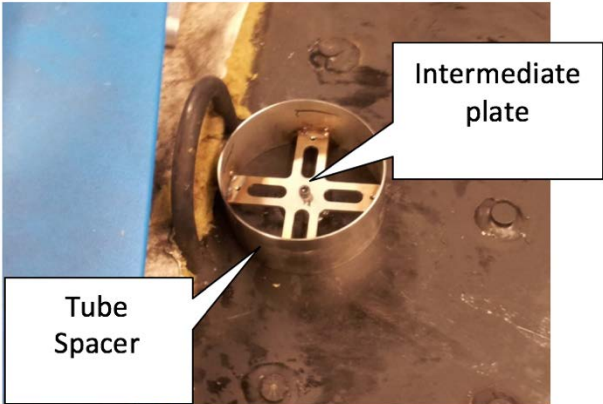


Figure 1-3. Load Cell Mount Assembly with Insulation

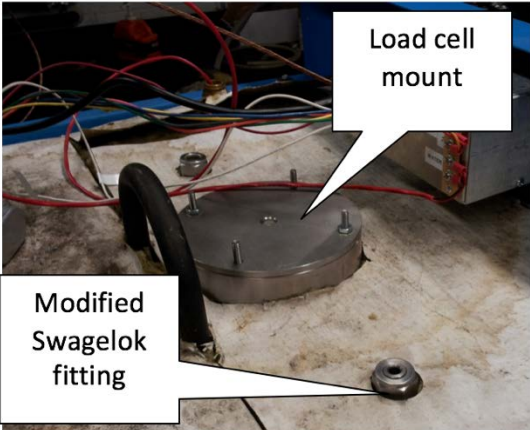


Figure 1-4. Safety Collar on RTFBRM with Upper Cross Member Assembly

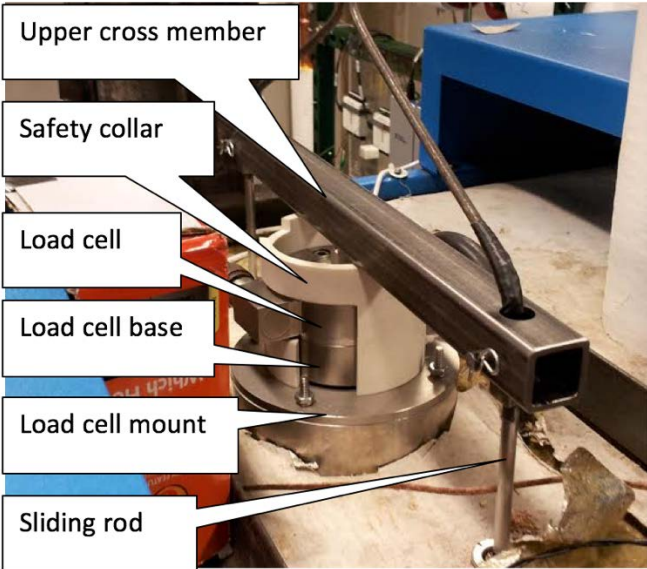


Figure 1-5. Drawing of Stay Arrangement of Boiler for Sliding Rod

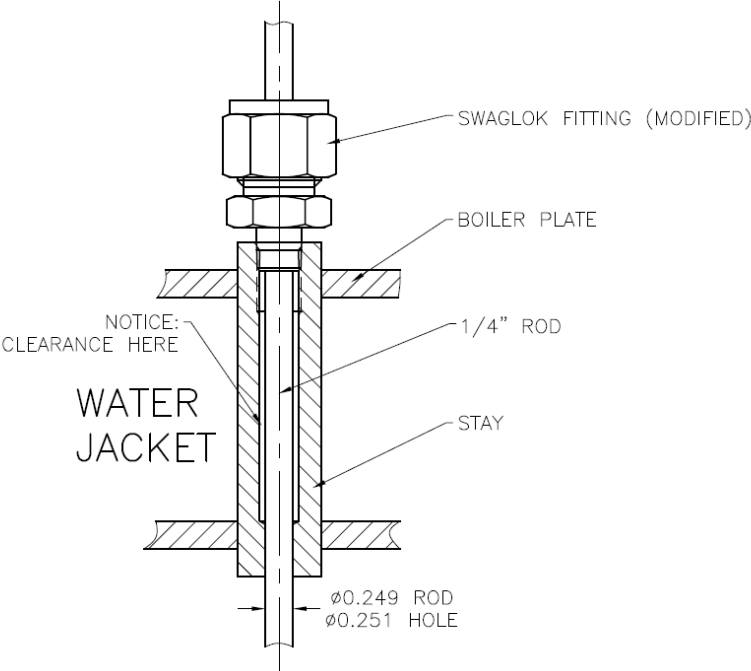


Figure 1-6. RTFBRM Hanging Basket

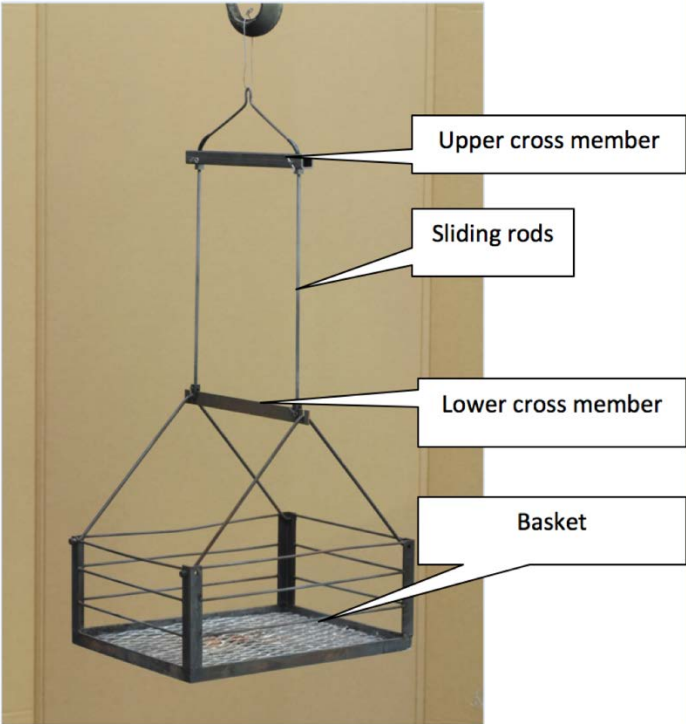


Figure 1-7. Inside View of Primary Combustion Chamber with Hanging Basket



Figure 1-8. Hanging Basket Lift System Mounted On Boiler

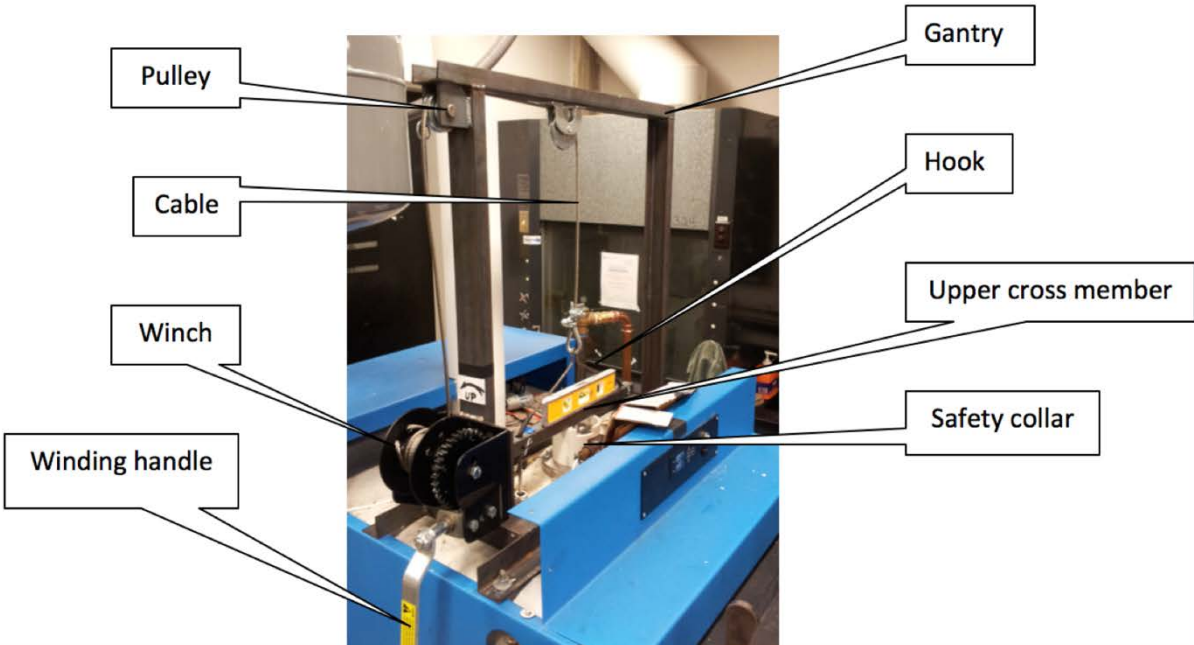


Figure 1-9. RTFBRM Mass Loss and Burn Rate Results

RTFBRM results showing (a) fuel mass vs time and (b) rate of mass loss vs time compared with BNL data.

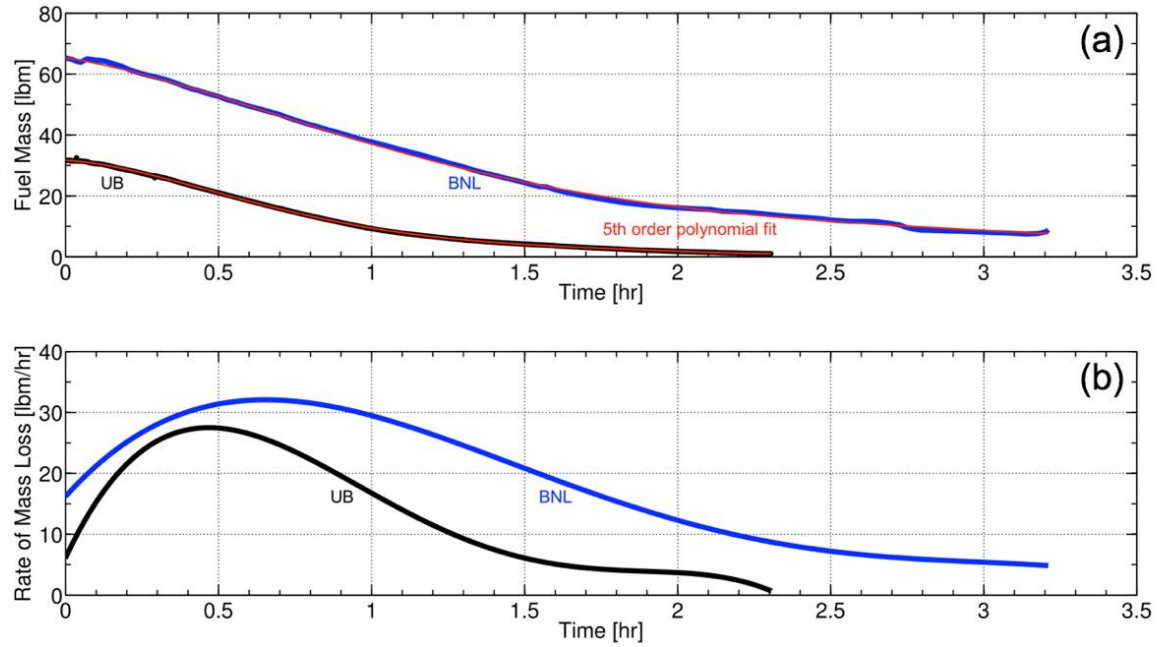


Figure 1-10. Normalized RTFBRM Mass Loss and Burn Rate Results

Normalized RTFBRM results showing (a) normalized fuel mass vs. normalized time (b) normalized rate of mass loss vs. normalized time compared with BNL data.

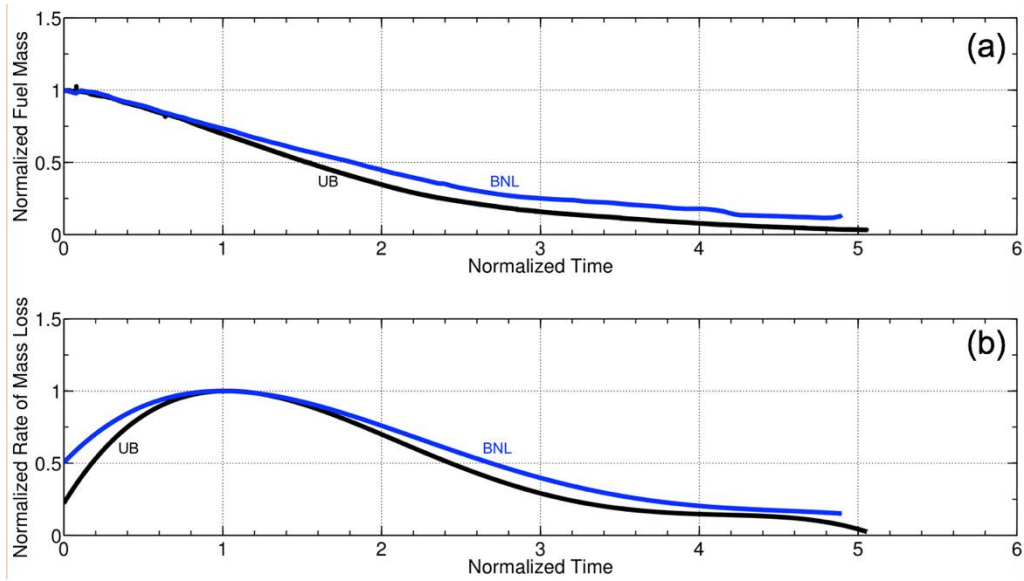


Figure 1-11. Instantaneous Heat Release Rates for Various Fuels

Instantaneous heat release rates for various fuels and moisture contents (dry-basis) using results from the RTFBRM half BIO BLOCK® load (LHV of each fuel was used). The table shows the integrated energy release over the duration of the run shown for each type of fuel. These values represent the total energy input into the system by the various fuels.

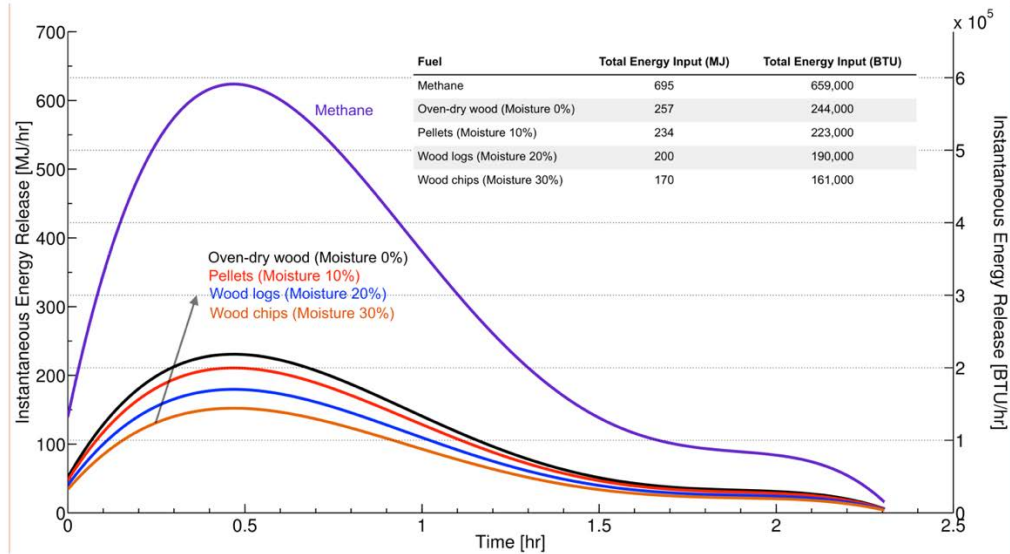


Figure 1-12. Boiler Experimental Schematic

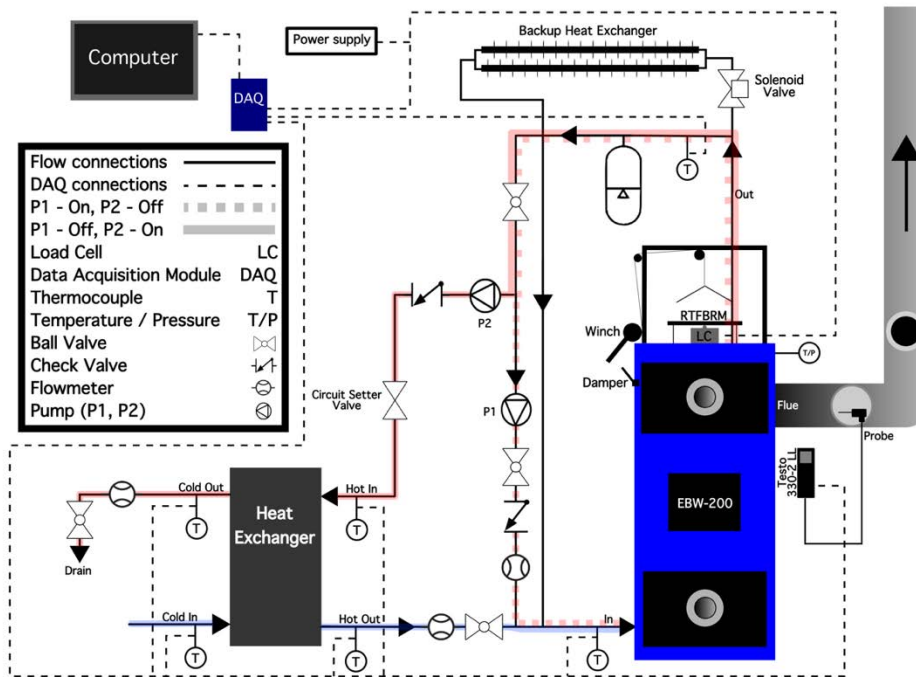


Figure 1-13. Arrangement of BIOBLOCKS in Primary Chamber



Figure 1-14. RTFBRM Results Comparison of Data

RTFBRM results showing (top) fuel mass vs. time and (bottom) rate of mass loss vs. time for a full and half load run (60 lbs. BIOBLOCKS[®] and 30 lbs. BIOBLOCKS[®] respectively) compared with a BNL Cat I run with ~65lbs cord wood.

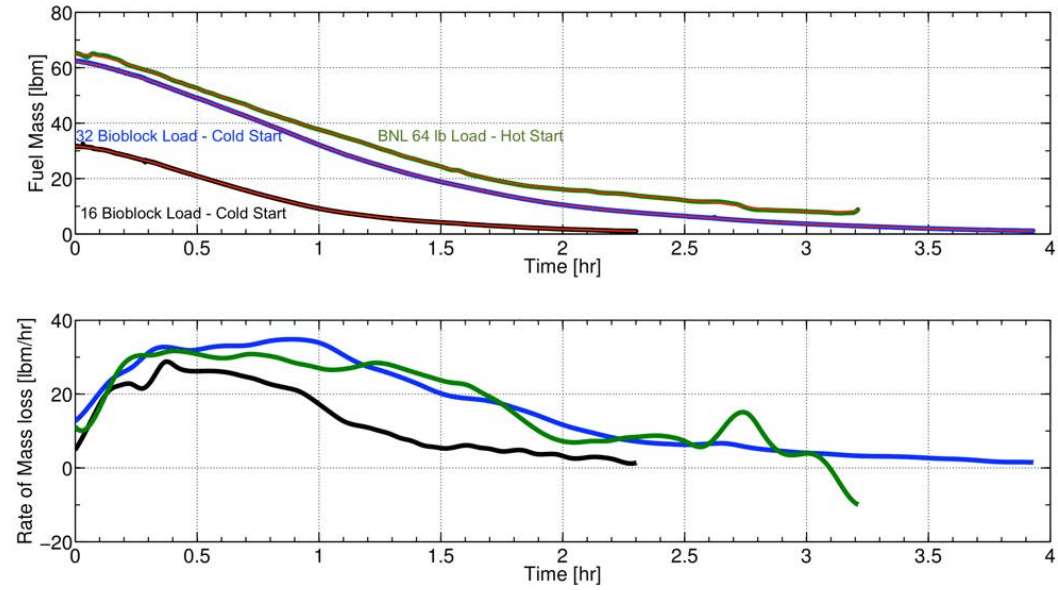


Figure 1-15. Normalized RTFBRM Comparison of Data

Normalized RTFBRM results showing (top) normalized fuel mass vs. normalized time (bottom) normalized rate of mass loss vs. normalized time for a full and half load run compared with BNL [9] full load run.

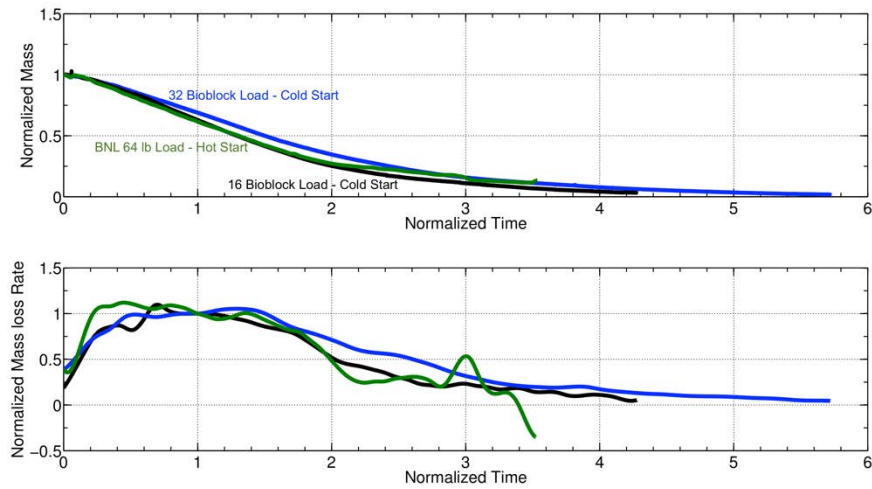


Figure 1-16. Stack Loss Efficiency Comparison

Stack loss efficiency for a 16 BIOBLOCK[®] burn with a cold start compared to a Category I cold start from BNL.

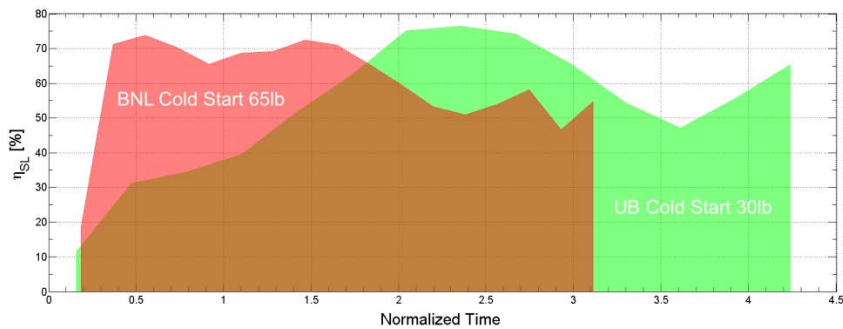
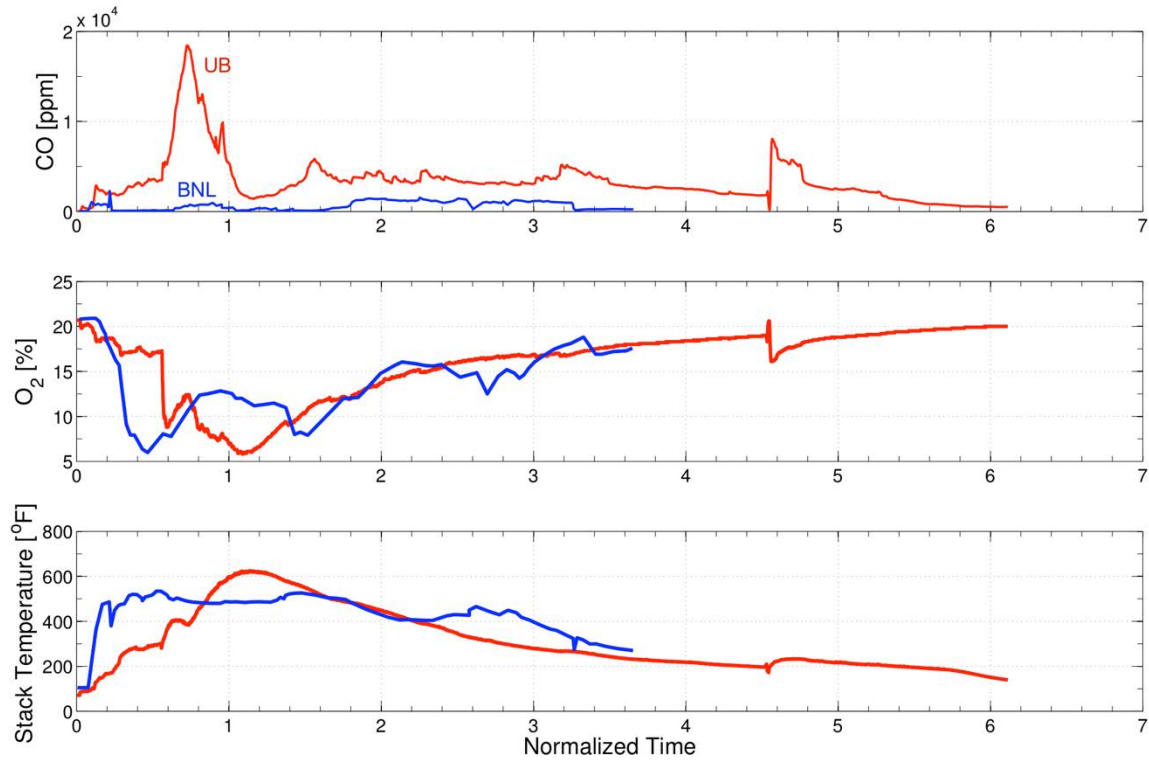


Figure 1-17. Emissions Comparison

Emissions comparison of CO, Oxygen, and flue temperature for full load cold start with BIOBLOCKS[®] (UB) and cord wood (BNL) The time has been non-dimensionalized in a similar manner to Figure 1-16.



2 Numerical Modeling and Combustion Optimization

2.1 Introduction

The World Health Organization estimates that over three billion people rely on wood and other traditional solid fuels for cooking and heating [14]. In particular, from the roughly 100 EJ/a of sustainable global biomass energy potential available today, 40 EJ/a is used for energy and 60% of that is used only in Asia where demand far exceeds supply [15-19]. With diminishing fossil fuel resources, biomass is expected to account for up to 30% of the world's annual demand for energy by 2050 [15]. The growing demand for hydronic heaters and other wood burning appliances has sparked an effort to provide stricter guidelines on the certification of these systems. The United States Environmental Protection Agency has recently defined new regulations for wood burning appliances including wood stoves, masonry heaters, pellet-burning stoves, and hydronic heaters [8]. Newer wood-fired systems are often equipped with a water jacket hydronic system to improve heat transfer efficiencies and to be compatible with existing hot-water heating systems.

A recent review on the use of biomass for boilers was done by Saidur *et al.* [20] and may be grouped into pellet [21, 22], wood chips [22, 23], cord wood, wood briquettes [24], and coal [25] based systems. For pellet and wood chip feed systems, the fuel flow rate is controlled, allowing for quasi-steady-state operation. Consequently, efficiencies and emissions are better understood and controlled. Less is known about cord wood systems since they are run as a completely unsteady batch process.

The purpose of this study is to experimentally explore the performance of a two-stage, downdraft, hydronic heater system and to confirm the results by developing a system level model to estimate thermal and combustion performance as a first approximation. This permits a general check on the internal consistency of the measurements as well as providing general guidance for future endeavors.

2.2 Experiments

2.2.1 Hydronic Heater Setup and Operation

A test facility is developed for this WFHH, similar in basic approach to that of Kang *et al.* [13]. Figure 2-1 shows (a) the front and (b) a cut-away of the Econoburn EBW-200 WFHH used in this study. The testing facility (Figure 2-1c) consists of the WFHH, primary and secondary water circulation loops, and heat exchanger. Early during a run, P1 is on and P2 is off to circulate the hot water through the boiler until reaching $150^{\circ}F$ (339 K). After the water comes to temperature, the second load loop (P2) is activated and

P1 is turned off. The load loop contains a 300,000 BTU/hr. (87.9 kW) counterflow heat exchanger to transfer heat from the boiler to a cold thermal sink. The heat rate is monitored by recording the water temperatures and flow rates, providing a detailed trend of the supplied heat load.

2.2.2 Fuel Burn Rate Measurement and Fuel Type

Performance characterization of a WFHH requires accurate monitoring of the instantaneous fuel burn rate (FBR), inlet and outlet temperatures of any working fluid, and emissions measurements from the exhaust. Figure 2-2a shows the RTFBRM assembly consisting of a basket suspended by two rods. The upper cross member rests on a piezoelectric based compression load cell shown in Figure 2-2b. The pancake load cell (Stellar Technology) is thermally insulated to avoid any biases induced from thermal gradients.

To minimize run-to-run variation, BIOBLOCKS[®], manufactured by Summit Wood Industries, are used. The blocks are made from 100% hardwood chips (primarily red oak). The moisture content (8.3% dry-basis by mass) and density (1.15 g/cm^3) of the blocks were measured in accordance with ISO standard 3130. A full load run requires 32 blocks (~62 lbs., 28 kg) to conform to current testing standards. Figure 2-2c shows the loading sequence of the BIOBLOCKS[®] fuel. Ignition of the fire is made in four locations (each side of the packed fuel load) using a propane torch. Consistent run terminations are achieved when flue exhaust: temperatures fall below 200°F (366 K), O_2 content is greater than 19% and CO is less than 1000 ppm.

2.2.3 Emission Measurements

During the boiler run, exhaust flue emissions measurements are recorded using a Testo 330-2 LL gas analysis meter. The analyzer takes measurements of the O_2 , CO , NO , pressure, and temperature from the center of the exhaust stream.

The CO_2 recorded by the Testo analyzer is estimated from the O_2 measurement and limited by the maximum theoretical value of CO_2 based on the fuel composition at the stoichiometric limit. It is therefore subject to interpretation and inaccurate for some conditions. To avoid this problem, a method is developed to determine the flue gas composition given the direct measurements of CO, NO, and O_2 . In this approach, the wood fuel is assumed to have the general composition $C_xH_yO_wN_z$ and burn according to the overall reaction: $C_xH_yO_wN_z + a(O_2 + 3.76 N_2) + b H_2O \rightarrow c CO_2 + d H_2O + e H_2 + f CO + g NO + h O_2 + i N_2$, where x, y, w, and z are assumed to be 1.0, 1.7, 0.72, and 0.001, respectively, which is representative of red oak [26] and is consistent with preliminary energy dispersive X-ray spectroscopy (EDS) results performed on a small sample of the BIOBLOCKS[®] fuel. The coefficient $b = 0.11214$ is

determined from the moisture content and the measured values of CO , NO , O_2 , given in mole fractions, are used to solve for the remaining twelve unknowns. The coefficients a, c, d, e, f, g, h, and i, along with the mole fractions of each species on the right-hand side (excluding those measured) are determined from the four atomic balance equations, seven equations relating moles to mole fraction ($X_i = a_i/N_{TOT}$), and closure is obtained by enforcing mole fractions to sum to unity. The resulting calculation provides the concentrations of all species (CO_2 , H_2O , H_2 , CO , NO , O_2 , and N_2) in the flue exhaust. It is assumed through this analysis that the wood moisture content evolves uniformly over the entire burn; however, it is more likely the full moisture content is evaporated within the first half of the burn time. This assumption would lead to a greater discrepancy in predicted gas concentration in early time where the rate of moisture release is greatest. Additionally, the dry-based gas concentrations measured by the Testo in the flue during this time would show a greater deviation to actual concentrations. A correction strategy would be required to account for this removed moisture during gas analysis measurement.

2.2.4 Combustion Chamber Measurements

Two instrument cluster cells have been designed for the upper and lower port holes. Figure 2-3 shows one of the cluster cells with a layout of the various gauges. These cells are designed to measure wall and gas temperature, oxygen concentration, wall heat flux, and gas pressure. Oxygen sensors in the instrument cluster cells are Bosch LSU 4.9 heated ZrO_2 lambda sensors, capable of measuring the gas mixture in an uncondensed (water vapor) state. For this study, only the primary chamber O_2 and gas temperatures are presented.

2.3 System Level Modeling

A system level model of boiler performance is developed based on quasi-steady flow assumptions and well-stirred reactor theory. In this approach, energy conservation equations are derived for the boiler (steel + water = b), solid fuel (f) and gas phase (g) systems,

$$\text{Equation 2-1} \quad m_g C_g \frac{dT_g}{dt} = \dot{Q}_{fg} + \sum_{fuel} \dot{m}_{g,i} h_i - \dot{Q}_{gb} + \dot{Q}_{air} - \dot{Q}_{flue}$$

$$\text{Equation 2-2} \quad m_b C_b \frac{dT_b}{dt} = \dot{Q}_{gb} - \dot{Q}_{del}$$

$$\text{Equation 2-3} \quad m_f C_f \frac{dT_f}{dt} = -\dot{Q}_{fg} + \dot{m}_f L_p$$

Where, $\dot{Q}_{del} = C_w \dot{m}_w (T_{w,out} - T_{w,in})$, is the delivered heat to the thermal load (heat exchanger) which is experimentally determined from measurements of the water temperature and flow rate going in ($T_{w,in}$)

and out ($T_{w,out}$) of the boiler. The quantities \dot{Q}_{fg} , \dot{Q}_{gb} , and \dot{Q}_{flue} represent the energy rates from the fuel to the gas, from the gas to the boiler, and that flowing out the flue, respectively. The heat transfer from the gas to the boiler is modeled using a mixed convective and radiative condition assuming black surfaces: $\dot{Q}_{gb} = A_{gb} [h_{gb} (T_g - T_b) + \sigma (T_g^4 - T_b^4)]$ where h_{gb} is the heat transfer coefficient across the gas-boiler interface where area is A_{gb} , and $\sigma = 5.567 \times 10^{-8} \text{ W/m}^2 - \text{K}^4$ is the Stefan-Boltzmann constant. The heat flow from the fuel to the gas can be expressed as $\dot{Q}_{fg} = A_{fg} [h_{fg} (T_f - T_g) + \sigma (T_f^4 - T_g^4)]$ over the fuel-gas interface area A_{fg} at wood temperature, T_f . In Equation 2-3, L_p is the latent heat of pyrolysis and \dot{m}_f is the total fuel mass loss rate that is experimentally measured. Ash in oak is typically less than 0.5% by mass of the dry fuel [27], and by ignoring this small fraction the mass flow rate of the fuel into the gas phase can be written as: $-\dot{m}_f = \sum_{fuel} \dot{m}_{g,i}$. Substituting this relation into the second term in Equation 2-1 results in: $\sum_{fuel} \dot{m}_{g,i} h_i = -\dot{m}_f \sum_{fuel} Y_i h_i (T_p)$ where Y_i are the mass fractions of the pyrolysis gases and h_i is the enthalpy of the i^{th} species at the wood pyrolysis temperature, T_p . The energy flow of gases in and out of the heater are defined as: $\dot{Q}_{air} = \dot{m}_{air} h_{air}$ and $\dot{Q}_{flue} = \dot{m}_{flue} \sum_{flue} Y_i h_i (T_g)$, respectively, where \dot{m}_{flue} is the total flue exhaust gas flow rate defined as: $\dot{m}_{flue} = \dot{m}_{air} + \dot{m}_f$.

The composition of pyrolysis products and flue gases are determined using local chemical equilibrium by minimizing the Gibbs function, $G = H - TS$, for a multiphase (solid-gas) system [28, 29]. Required atomic ratios of molecules are established from an assumed wood composition, $CH_{1.7}O_{0.72}N_{0.001}$, corresponding to red oak. The composition of the pyrolysis products are assumed to consist of $CO, CO_2, H_2O, H_2, CH_4$, and $C(solid)$ [30-32] and are a function of an assumed wood pyrolysis temperature. Figure 2-4 presents pyrolysis products versus assumed pyrolysis temperature and shows the char produced varies little over the temperature range of 500 – 800 K. For the model predictions, a wood pyrolysis temperature of 700 K is selected resulting in pyrolysis product yields of $Y_{CO} = 0.007, Y_{CO_2} = 0.3086, Y_{H_2O} = 0.291, Y_{H_2} = 0.0109, Y_{CH_4} = 0.1096, Y_{C(solid)} = 0.2724$ (and very small traces of C_3H_8). The char yield from this estimate compares favorably to measured char yields found in literature [27, 30]. Emission predictions are found to be insensitive to the selection of T_p between 500 and 800 K. For the flue gases, the pyrolysis products are augmented with a known air flow rate, $\dot{m}_{air} = 3.02 \text{ kg/min}$. The flue gases are assumed to be composed of the same species as the pyrolysis products but with $Y_{CH_4} = Y_{C_3H_8} = Y_{C(solid)} = 0$, *i.e.* due to complete combustion within the “stirred-reactor”.

Since the thermal inertia of the solid fuel is small relative to that of the boiler, the fuel is assumed to be at its pyrolysis temperature, therefore $\frac{dT_f}{dt} \approx 0$. Equation 2-3 $m_f C_f \frac{dT_f}{dt} = -\dot{Q}_{fg} + \dot{m}_f L_p$ is approximated to, $\dot{Q}_{fg} = \dot{m}_f L_p$, and used to simplify Equation 2-1 to,

$$\text{Equation 2-4} \quad m_g C_{v,g} \frac{dT_g}{dt} = \sum_{fuel} \dot{m}_{g,i} h_i - \dot{Q}_{gb} + \dot{Q}_{air} - \dot{Q}_{ftue} + \dot{m}_f L_p$$

With \dot{m}_f and \dot{Q}_{del} given from the experimental data, Equation 2-2 and Equation 2-4 are integrated in time using a semi-implicit time marching scheme [33].

2.4 Results and Discussion

2.4.5 Solid Fuel Mass Loss and Mass Loss Rate

Figure 2-5a presents the measured fuel mass as a function of time for all runs. The data is presented with various run conditions including three half load runs and one warm start (where the fuel is ignited by the hot coal bed). The mass loss is filtered and fitted using a second order, low-pass Butterworth filter and cubic spline interpolation which is then piecewise differentiated to compute the FBR ($-\dot{m}_f$). Figure 2-5b presents the results of these operations showing a repeatable peak burn rate at $\sim 30 - 60$ minutes depending on initial load size.

Data reduction of the FBR measurements is achieved using an analytical analysis of the burn rate expressed as: $\dot{m}_f = -\dot{m}_f'' A_{fg}$ where \dot{m}_f'' is the mass flux of pyrolysis products and $A_{fg} \approx (m_f/\rho_f)^{2/3}$ is the pyrolysis surface area (char is assumed to oxidize as soon as it is formed). During the burning process it is hypothesized that the A_{fg} decreases with time due to the reduction in fuel while \dot{m}_f'' increases in time due to the increase in heat flux to the pyrolysis surface. The product combination of these two trends will therefore lead to a local maximum in burn rate - consistent with the experimental observations. Substituting \dot{Q}_{gb} and \dot{Q}_{fg} from Equation 2-2 and Equation 2-3, respectively, into Equation 2-1, and enforcing the condition that the thermal inertia of the gas and fuel are small relative to the boiler, Equation 2-2 becomes,

$$\text{Equation 2-5} \quad m_b C_b \frac{dT_b}{dt} = \dot{m}_f L_p - \dot{Q}_{del} + \sum_{fuel} \dot{m}_{g,i} h_i + \dot{Q}_{air} - \dot{Q}_{ftue}$$

Since changes in sensible energy are small relative to changes in chemical energy content, the last three terms on the right-hand side of Equation 2-5 are simplified to: $\sum_{fuel} \dot{m}_{g,i} h_i + \dot{Q}_{air} - \dot{Q}_{ftue} \approx -\dot{m}_f \Delta h_{comb}$, where Δh_{comb} is the heat of combustion of the pyrolysis products. Integrating Equation

2-5 from the initial state of when the wood first starts to decompose ($T_{b,o}, m_{f,o}$) to an arbitrary time, t , results in the following relation,

$$\text{Equation 2-6} \quad T_b(t) - T_{b,o} = (m_o - m_f(t)) \frac{\Delta h'_{comb}}{m_b C_b} - \frac{\Delta Q_{del}}{m_b C_b}$$

where $\Delta Q_{del} = \int \dot{Q}_{del} dt$ is the total heat delivered and $\Delta h'_{comb} \equiv (\Delta h_{comb} - L_p)$ is the effective heat of combustion. With the wood assumed to be at its pyrolysis temperature, the mass flux of gases can be expressed as: $\dot{m}_f'' \approx h(T_b - T_d)/L_p$ where T_p is the previously defined wood pyrolysis temperature and h is an (unknown) convection coefficient. Substituting Equation 2-6 into the fuel mass flux, along with the approximation, $A_{fg} \approx (m_f/\rho_f)^{(2/3)}$, results in a single, non-linear, ordinary differential equation for the non-dimensionalized fuel mass (M_f),

$$\text{Equation 2-7} \quad \frac{dM_f}{d\tau} = -M_f^{\frac{2}{3}} (\alpha - M_f)$$

where $M_f \equiv m_f/m_{f,o}$, $\tau \equiv t/t_c$ and $\alpha \equiv 1 + [m_b C_b(T_{b,o} - T_p) + \Delta Q_{del}(\tau)]/(\Delta h'_{comb} m_o)$. The quantity t_c represents a characteristic time scale and is defined as: $t_c \equiv m_b C_b / [A_o h(\Delta h'_{comb}/L_p)]$ where $A_o = 6(m_o/\rho_f)^{(2/3)}$ is the initial fuel surface area. This is taken as a first approximation of the fuel surface area assuming a cubic shape, where block to block proximity (decreases effective surface area) and fuel fragmentation (increases effective surface area) are left unquantified. Taking the derivative of Equation 2-7 with respect to τ and setting the result equal to zero results in a condition for when the peak mass loss rate will occur: $(M_f)_{\tau_{peak}} = 2\alpha/5$. In order for the mass flux to be positive then, $T_{b,o} > T_d$, therefore α must always be greater than unity. During the early phases of the burning process, ΔQ_{del} is equal to zero since the water in the boiler is only recirculated by P1 therefore there is no thermal load (see Figure 2-9a). Using this assumption, Equation 2-7 may be analytically integrated to get a closed form, inverse solution for M_f , in terms of τ and α ,

$$\text{Equation 2-8} \quad \tau = \frac{\ln \left(\frac{\left(\alpha^{\frac{2}{3}} + 3\sqrt{\alpha} + 1 \right) \left(3\sqrt{\alpha} - 3\sqrt{M(\tau)} \right)^2}{\left(3\sqrt{\alpha} - 1 \right)^2 \left(\alpha^{\frac{2}{3}} + M(\tau)^{\frac{2}{3}} + 3\sqrt{\alpha} 3\sqrt{M(\tau)} \right)} \right) - 2\sqrt{3} \tan^{-1} \left(\frac{\sqrt{3} 3\sqrt{\alpha} \left(3\sqrt{M(\tau)} - 1 \right)}{2\alpha^{\frac{2}{3}} + 3\sqrt{\alpha} + \left(3\sqrt{\alpha} + 2 \right) 3\sqrt{M(\tau)}} \right)}{2\alpha^{\frac{2}{3}}}$$

Figure 2-6 presents comparisons of normalized mean measured fuel and mass loss rate data to the model where the results of Figure 2-5 are re-plotted in terms of M_f and τ . For each data set, α is determined by identifying the value of M_f corresponding to the peak mass loss rate ($M_{f,max}$), i.e., $\alpha = (5/2)M_{f,max}$. This typically corresponds to $\alpha \approx 1.6$. Substituting in $M_f = (2/5)\alpha$ and the value of α into Equation 2-8

provides the non-dimensional time corresponding to the peak mass loss rate, $\tau_{max} = t_{max}/t_c \approx 0.5$. Comparing this result to time measured (t_{max}) results in an estimated value of $t_c \approx 1.39 \text{ hr}$ which can be thought of as a characteristic response time of the coupled boiler and solid fuel system. This response time represents the “elbow” of the original data mass loss curve and is often referred to by the WFHH industry as the “steady-state” portion of the burn rate curve. Figure 2-6b shows the mass loss rate measurements replotted in terms of \dot{M}_f and τ . As shown, the measurements collapse over the early time indicating the model and measurements are self-consistent. At later times, deviations are observed when the model is expected to break down when \dot{Q}_{del} is no longer negligible; however, the following empirical curve fit is applicable,

Equation 2-9
$$M_f(\tau) = 13.279 \times 10^{-4} \tau^8 - 17.659 \times 10^{-3} \tau^7 + 82.516 \times 10^{-3} \tau^6 - 11.082 \times 10^{-2} \tau^5 - 32.671 \times 10^{-2} \tau^4 + 1.3025 \tau^3 - 1.3726 \tau^2 - 0.2164 \tau + 1.0031$$

and is shown as the best-fit mean (Figure 2-6, red line). This empirical fit could serve as a natural starting point for characterizing and reducing data for a new boiler/fuel system that has a similar heat load apparatus.

2.4.6 Emissions

2.4.6.1 Time Trends

Emissions and temperature predictions from the system level numerical model are compared to measured data in Figure 2-7 showing (a) exit flue and primary chamber gas temperatures, (b) exhaust and primary chamber O_2 and (c) CO_2 concentrations for three full-load boiler runs. Input parameters are summarized in Table 2.1.

Figure 2-7 shows (a) the primary chamber gas temperature reaches a higher magnitude at peak burn rate compared to the temperatures downstream at the flue and those predicted by the model (corresponding to the exit/flue). The variation in temperatures in the range from $0 < \tau < 1$ imply the early effects of mixing within the primary chamber, compared to the smooth trend seen in the measured flue temperatures. The sudden change in trend seen in the measured flue temperatures at approximately $\tau = 0.25$ is due to closing the damper in the upper chamber, forcing the flow of exhaust gases into the secondary chamber and effectively increasing the thermal capacitance experienced by the gas stream. Oxygen concentration in the primary chamber is expectedly lower due to the split of the air stream into the primary and nozzle locations. During the ramp up of the FBR there is a corresponding increase in gas temperatures and CO_2 while a decrease in O_2 is observed. Run-to-run variations in the modeling and data are due to slight differences in the time dependent heat transfer load, \dot{Q}_{del} . Overall, the agreement between the model predictions and data

is reasonable with the model reproducing the same dependency on the heat transfer load. Differences between experimental and model predictions are largely due to two reasons. The first is the well stirred reactor assumption where the extent of combustion is over-predicted resulting in higher predicted values of temperatures and CO_2 and an under prediction of O_2 . In reality, burning rate of the pyrolysis gases will be highly dependent on the rate of turbulent mixing in the primary and secondary chambers for which the current model does not take into account. The second reason for differences is the non-homogeneous heat transfer path present in the experiments that is not accounted for in the model resulting in a predicted lag in the peak temperature, CO_2 , and O_2 . As shown in Figure 2-7, the difference in the peak temperature is approximately $\Delta \tau \approx 0.5$, corresponding to a physical time of approximately 42 min. Using the definition of t_c with $\Delta h'_{comb} = 19.9 \text{ MJ/kg}$, $L_P = 6.73 \text{ MJ/kg}$ for red oak and $m_b = (m_s + m_w) = 1053 \text{ kg}$, $C_b = \frac{m_s C_s + m_w C_w}{m_b} = 1036.7 \text{ J/kg} \cdot K$ then a convection heat transfer coefficient of $h = 146 \text{ W/m}^2 \cdot K$ is determined. This convection coefficient can be used to compute an estimated boiler thermal response time of $\tau_b = m_b C_b / (h A_b) = 35 \text{ min}$ which is in good agreement to the observed thermal time lag. Considering the ratio of fuel to boiler heat capacity $(m_f C_f) / (m_b C_b) = 0.035$, the effect of the fuel thermal inertia is neglected over that of the boiler.

2.4.6.2 State Maps

To explore the operating conditions of the boiler, three dimensional emission state-maps are constructed [34, 35] from the experimental data and model predictions as a function of temperature and equivalence ratio (ϕ) - analogous to those used in the automobile industry to identify favorable combustion trajectories [36-38].

Figure 2-8 shows a comparison of state maps for major species (O_2 , CO_2 , and H_2O). For each case, surfaces are constructed using all of the experimental data along with associated model predictions. For all cases, a representative combustion trajectory is added (black line) showing a typical time history of emissions.

The overall trends and magnitude within the $T - \phi$ space is similar and consistent with the time history predictions (Figure 2-7). As expected using equilibrium theory, the major species vary little with temperature since they are energetically stable at lower temperatures. The emission data from the experiments, however, shows much more variation, which is largely due to the presence of turbulent mixing as the flow progresses through the chambers of the boiler.

2.4.7 Thermal Efficiency

Thermal efficiency is often expressed in terms of total (integrated) heat delivered (ΔQ_{del}) divided by the total caloric chemical energy available (ΔQ_{comb}) of the fuel used, *i.e.*, $\bar{\eta}_{th} = \Delta Q_{del} / \Delta Q_{comb}$, where a single efficiency is reported per fuel charge [8]. While this definition provides an estimate of the average efficiency of a boiler, it is limited since important transient information is lost. The missing time dependent information is useful for not only understanding the boiler dynamics but also as an input parameter for developing boiler control strategies. An *instantaneous thermal efficiency* (η_{th}) is therefore desirable. The practical calculation of it is problematic, often resulting in computed values of η_{th} greater than unity. The fallacy using this definition is it assumes the boiler is running at “steady-state” and the unsteady heating of the boiler (steel and water jacket) is not taken into account. Since the thermal inertia of most boilers is large relative to the heat produced, ignoring the thermal inertia of the boiler results in large errors in η_{th} . To circumvent these challenges, an alternative definition of η_{th} is desirable that accounts for the rate of heat transfer into thermal storage (\dot{Q}_{stor}): $\eta_{th} = (\dot{Q}_{del} + \dot{Q}_{stor}) / \dot{Q}_{comb}$ where $\dot{Q}_{comb} = (|\dot{m}_f| \Delta h'_{comb})$ is the heat produced from combustion.

The term $\dot{Q}_{stor} = C_b m_b (dT_b/dt)$ represents the instantaneous heat transferred to the boiler. Figure 2-9a shows the \dot{Q}_i 's versus τ for a typical boiler run. \dot{Q}_{del} and \dot{Q}_{stor} are inversely proportional indicating the heat rate delivered from the water is coming from the boiler heat capacitance - rather than from the heat generated from combustion. For $\tau > 3$, $\dot{Q}_{comb} \rightarrow 0$, as the fuel burns out occurring while as much of the heat load is removed from the boiler water jacket as possible.

While the η_{th} definition with a storage term is appealing, practical challenges remain with the measurement (and interpretation) of dT_b/dt since the boiler isn't truly thermally homogeneous, resulting in $\eta_{th} > 1$ at certain times during the burn. To reduce these problems and still provide time dependent information, an integrated thermal efficiency is defined: $\bar{\eta}_{th} \equiv (\Delta Q_{del} + \Delta Q_{stor}) / \Delta Q_{comb}$, where $\Delta Q_i \equiv \int \dot{Q}_i dt$. Figure 2-9b presents these terms for the same boiler run as in (a). The corresponding ΔQ 's are much smoother and physically realizable over the entire boiler experiment. Use of these terms for defining $\bar{\eta}_{th}$ is presented in Figure 2-9c for three data sets and shows a reasonable collapse with $\bar{\eta}_{th}$ having a nearly linear increase over the range of $1 < \tau < 2$ and attains a final value of approximately 55% - consistent with thermal efficiencies commonly reported for these devices [8].

2.5 Conclusions

A novel approach for measuring instantaneous solid fuel mass and burn rate is presented. A new analytical model of mass loss rate is developed that results in a non-dimensional consolidation of mass loss rate data during the early phases of burning and explains the existence of the maximum mass loss rate as a competition between the increase in heat flux to the fuel surface and decrease in fuel surface area with time.

A single chamber lumped system level model is created to estimate exit gas temperatures and emissions species concentrations using a gas phase equilibrium model working under well-stirred reactor assumptions. The model predicts gas temperatures in close agreement with measured experimental trends as well as reasonable predictions of major species concentrations. State map contours are developed to describe the path of the emissions over a typical burn. Comparisons of experimental data and model (equilibrium) predictions show similar overall trends and compare well in magnitude for major species (O_2 , CO_2 , and H_2O).

Finally, a method for examining the unsteady progression of the overall thermal efficiency is presented by including the thermal inertia and integrating the value from time zero to each respective point in time. The result is a temporal progression of the integrated thermal efficiency leading to the final and overall thermal efficiency. The results indicate a linear growth rate of efficiency in the range of $1 < \tau < 2$ and reaching an asymptotic value ranging from 48% to 55% corresponding to that reported in testing of two-stage hydronic heaters [39].

Table 2.1. Summary of Parameters for System Level Model

Parameter	Value
m_b	1054 kg
m_s	898 kg
m_w	155 kg
m_o	28 kg
L_p	6.73 MJ/kg
$\Delta h'_{comb}$	19.9 MJ/kg
$\Delta h'_{comb}/L_p$	2.96 [30]
h_{gb}	146 W/m ² · K
T_p	700 K
Moisture content	8.3%
A_{fg}	0.504 m ²
A_{gb}	3.513 m ²
ρ_f	1150 kg/m ³
C_f	1360 J/kg · K
C_b	1037 J/kg · K
C_s	490 J/kg · K
C_w	4188 J/kg · K

Figure 2-1. Econoburn Boiler, Internal View, Schematic

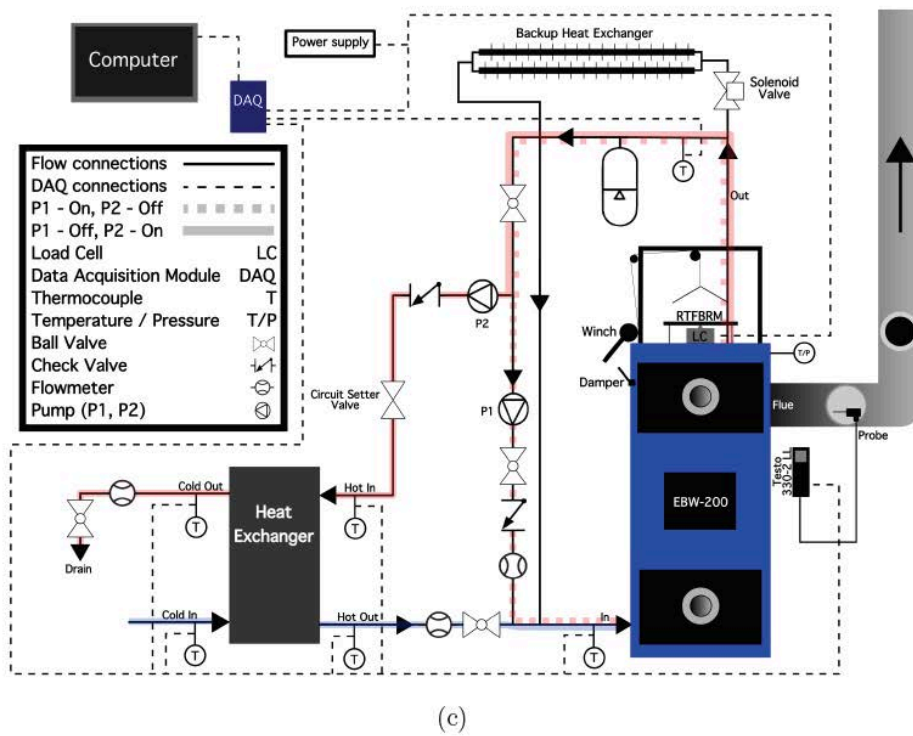
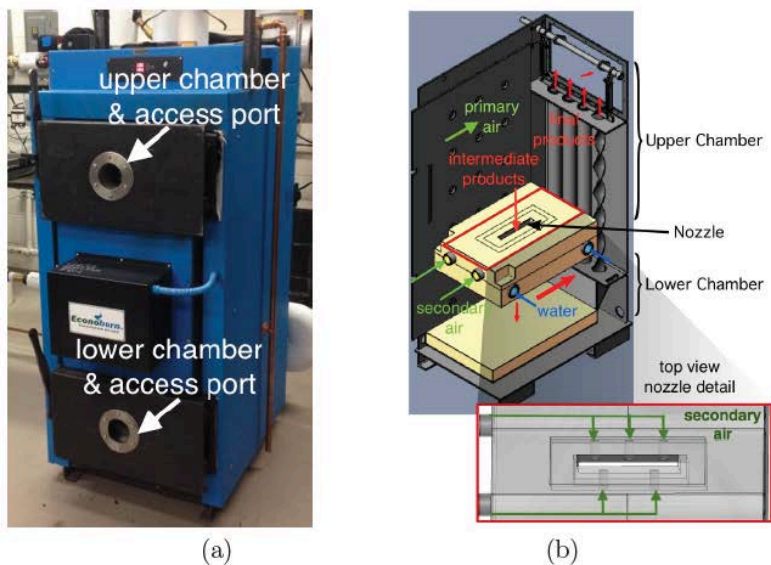
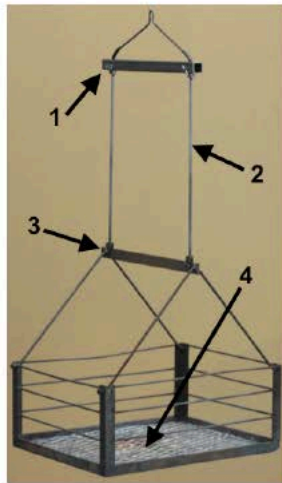


Figure 2-2. RTFBRM and Fuel Loading Configuration

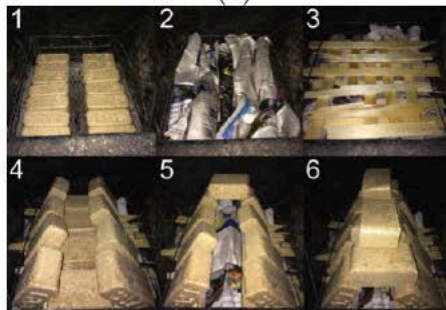
Real time fuel burn rate monitor showing views of (a) basket assembly with (1) upper cross member, (2) sliding rods, (3) lower cross member, (4) basket, (b) piezo-electric compression cell and (c) fuel loading sequence consisting of: 2 rows of seven blocks (step 1), newspaper (step 2), kindling organized in grid pattern (step 3), pyramid construction (step 4), additional newspaper inside pyramid (step 5) and additional block to cover pyramid (step 6).



(a)



(b)



(c)

Figure 2-3. Instrument Cluster Cell

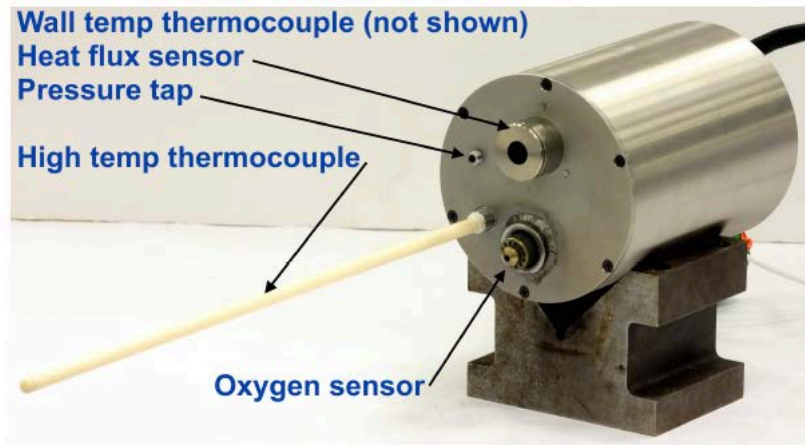


Figure 2-4. Pyrolysis Products as a Function of Pyrolysis Temperature

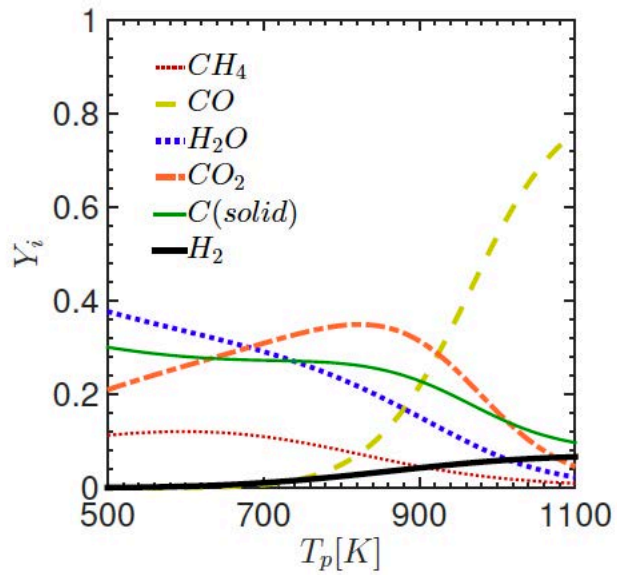
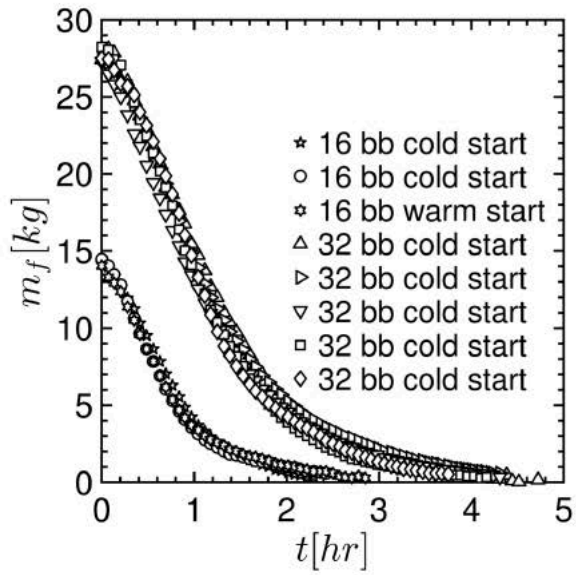
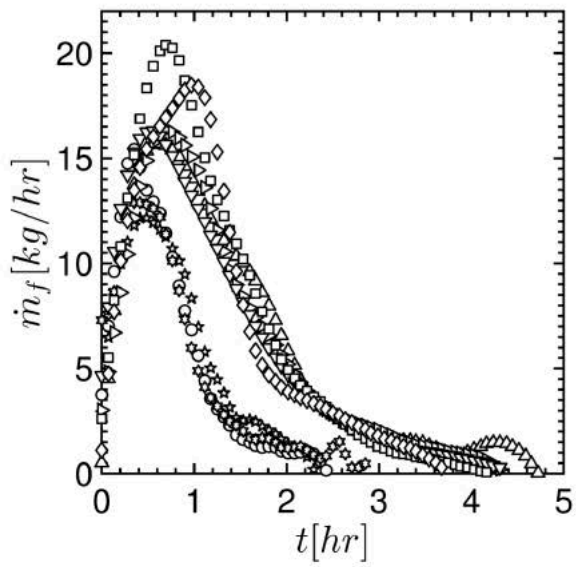


Figure 2-5. Comparison of Mass (a) and Burn Rate (b) for Cases



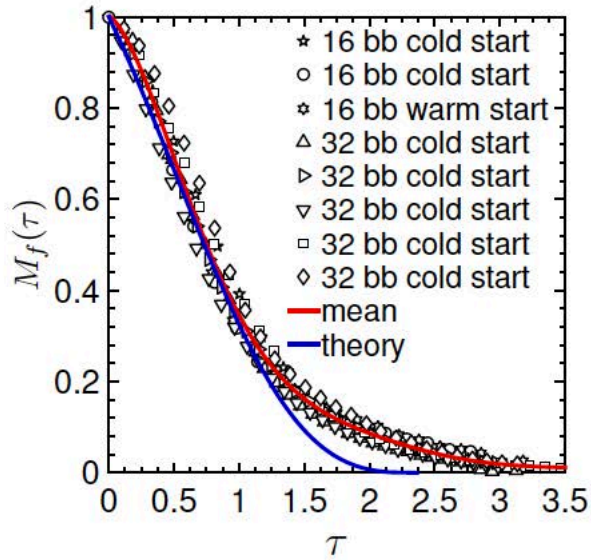
(a)



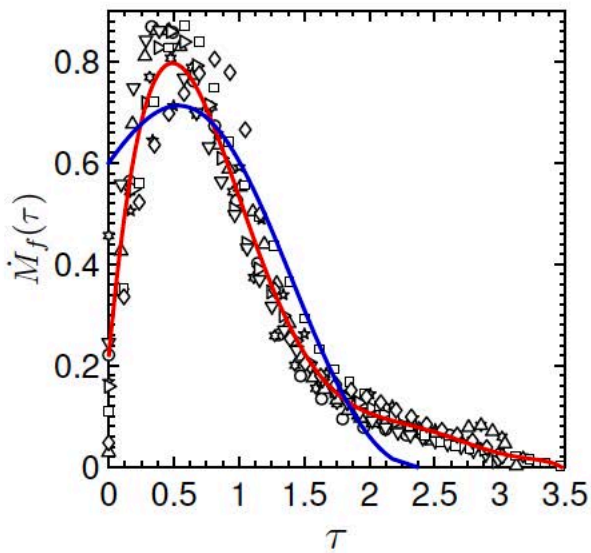
(b)

Figure 2-6. Comparison of Normalized Mass and Burn Rate

Comparison of model normalized data (symbols) with mean trends (red lines) for with theoretical fit (blue lines) for (a) solid fuel mass (M_f) and (b) fuel mass loss rate (\dot{M}_f).



(a)



(b)

Figure 2-7. Comparison of Characteristic Runs for System Level Model to Data

Comparison of three characteristic runs showing time dependent trends of (a) gas temperature, (b) O_2 and (c) CO_2 concentrations from relevant experimental data and the system level model.

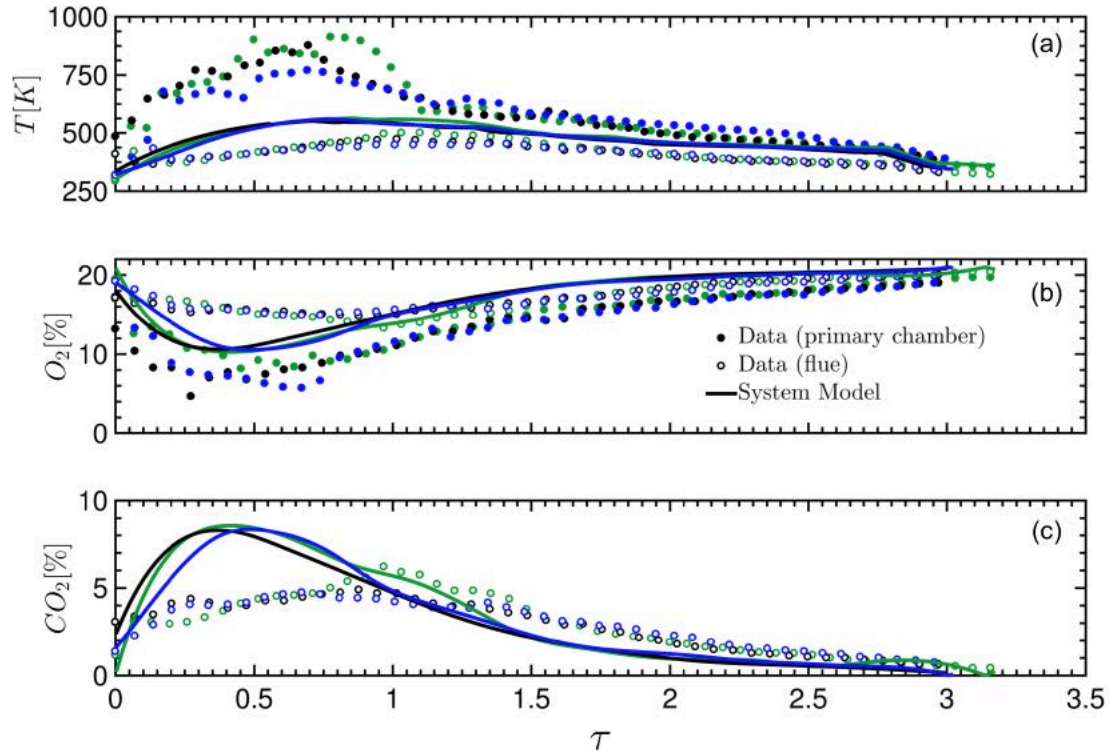


Figure 2-8. Emissions State Maps for Major Species

Emission state maps for major species O_2 (a, b), CO_2 (c, d), and H_2O (e, f) from experimental results (left) using all data compared with results from the system level model (right) using well-stirred reactor and gas phase equilibrium theory. Black arrows represent a typical path for a full duration burn.

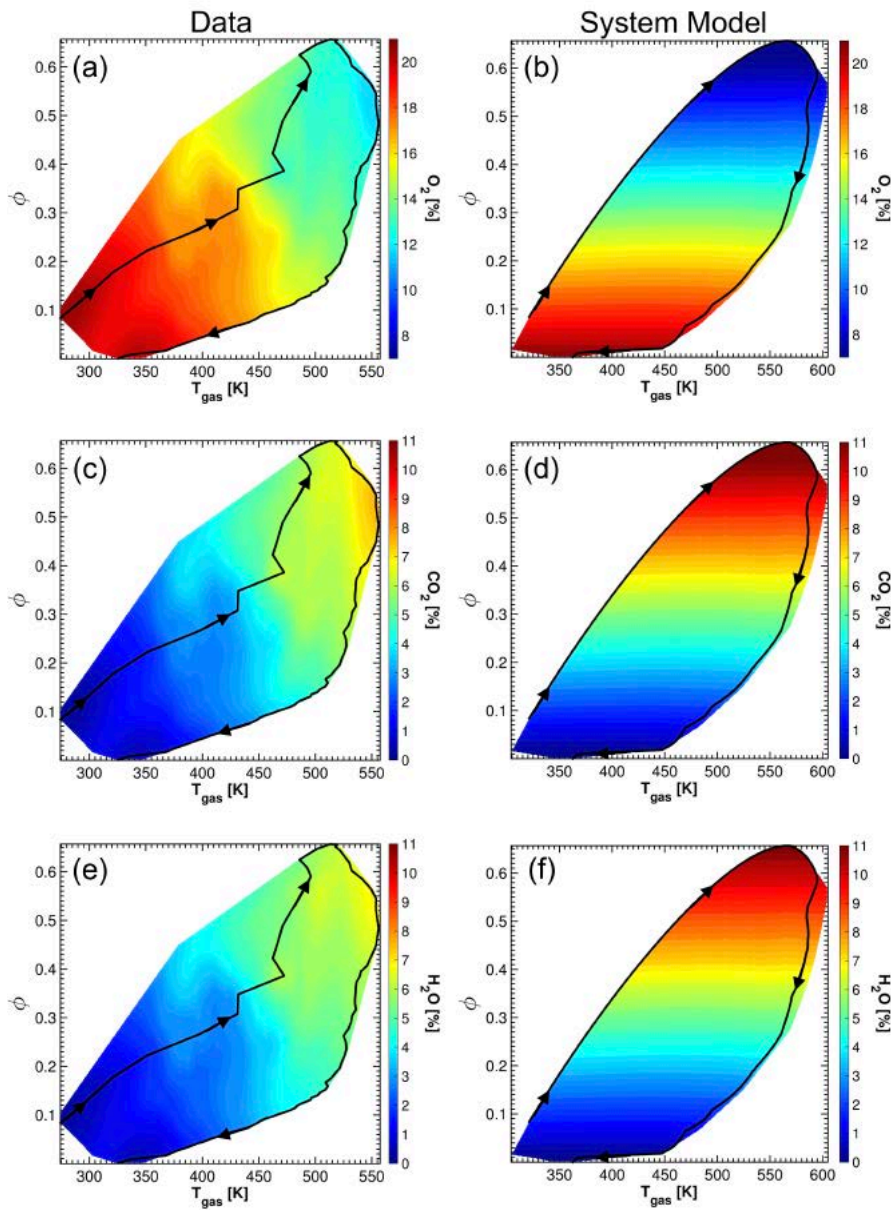
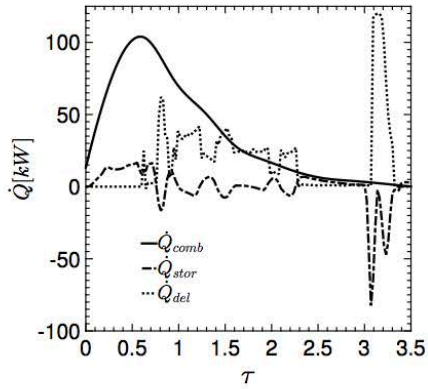
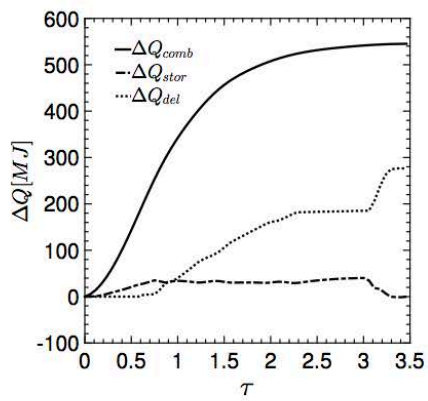


Figure 2-9. Summary of Thermal Efficiency Calculation

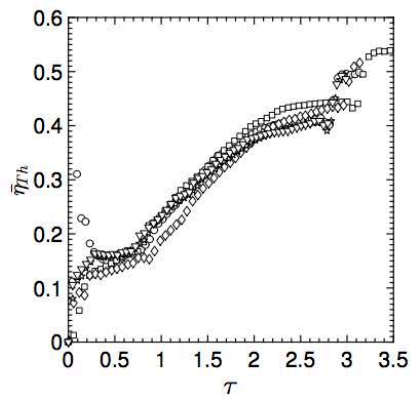
Summary of thermal efficiency calculations showing (a) \dot{Q}_{comb} , \dot{Q}_{stor} , and \dot{Q}_{del} , for a single case, (b) ΔQ_{comb} , ΔQ_{stor} , and ΔQ_{del} for the same case, and (c) $\bar{\eta}_{th}$ for five different cases.



(a)



(b)



(c)

3 Emission Reduction Design and Testing

3.1 Introduction

Given the world's high demand for renewable energy resources, CO_2 neutral biomass fueled systems are experiencing an increase in popularity. European companies have been developing this technology for several decades and exhibit a considerable improvement in thermal efficiency and emissions output compared with similar American designs. This is in part due to strict European regulations forcing rapid technological advancements. The United State Environmental Protection Agency's incremental regulatory revisions to reduce maximum emissions levels are helping to spur developments on this front. For the northeast US, emissions from wood-fired heaters are one of the leading sources of reduced air quality. To provide stricter guidelines on the certification of these systems, the EPA has recently defined specific new regulations for wood burning appliances including wood stoves, masonry heaters, pellet-burning stoves, and hydronic heaters [8]. Reduction in harmful pollutants resulting from the combustion of wood based biomass materials is the primary goal of many research endeavors.

In this study, experimental measurements were taken to compare a baseline case to the augmented case, testing the emissions reduction device. A mixing pot, placed in the secondary chamber is used to augment the secondary flow. This mixing pot, is constructed of fiberboard material capable of withstanding very high temperatures. It's intended as a potentially inexpensive after-market design change to increase the combustion efficiency without a costly change to the boiler manufacturing process. Observation of other heater designs, such as the European Fröling cord wood heater, demonstrates a similar approach where the secondary flow is injected asymmetrically into a ceramic tube, promoting a swirl that increases turbulent mixing and residence time. In a similar form the mixing pot used in this study provides insulation from the direct contact of the hot gas on the cooler chamber walls (effectively halting further oxidation of species), while also increasing residence time. Measurements of gas temperature and emissions (CO , NO , and CO_2) are compared along with total integrated emissions calculated for each run. Experimental results only provide limited insight on the effects of the device.

Computational simulations were conducted to better understand turbulent mixing in the secondary chamber of the Econoburn EBW-200 boiler. The technical approach was based on the use of a computational framework developed by DesJardin and co-workers that solves the governing equations describing turbulent reacting fluid flows in complex geometries using Computational Fluid Dynamics (CFD). The downstream mixing of fuel and air in the secondary combustion chamber was explored by modifying the chamber geometry. The baseline design of the EBW-200 system features an impact plate used to encourage

mixing of pyrolysis gases. An alternative method using a mixing pot was explored experimentally, which resulted in increased gas temperatures and reduced CO emissions. Cold-flow CFD simulations of the mixing pot were conducted to provide physical insight into this process. Additional CFD simulations were done to explore the fundamental role of the impact plate geometry on turbulent mixing. Several configurations were compared by varying angles and directions of the impact plate.

This report is organized as follows. Section 4.2 will detail the experimental setup. Section 4.3 will discuss the design selection of the mixing pot. Section 4.4 will discuss the modification of the boiler with the mixing pot and experimental and computational results. Section 4.5 will address the computational analysis of the impact plate geometry. Finally, section 4.6 will summarize the findings from these tasks.

3.2 Experimental Setup

The test facility previously discussed in [40] is used in this study where an Econoburn EBW-200 wood-fired hydronic heater is instrumented. The setup consists of primary and secondary water circulation loops and a heat exchanger to expel heat. Figure 3-1(a) shows the boiler setup, where the load loop contains a 300,000 BTU/hr. (87.9 kW) counterflow heat exchanger to transfer heat from the boiler to a cold thermal sink. The heat rate is monitored by recording the water temperatures and flow rates, providing a detailed trend of the supplied heat load.

To minimize batch-to-batch variability associated with boiler operation, BIOBLOCKS[®] are used as the primary fuel source. As described above, the standard loading configuration has been adopted to produce a repeatable burn [40].

Blower air flow rates are measured using a Bosch HFM-7 mass airflow meter operating under hot film anemometry methods. Direct calibration of the Bosch meter was made with an ASME standard venturi flow meter across a wide range of flow rates to correlate output voltage to measured flow rate.

Emissions measurements are recorded using a Testo 330-2 LL gas analysis meter. The analyzer is capable of taking experimental measurements of the O_2 , CO , NO , pressure, and temperature from the flue gas stream. The O_2 measurement has a range of 0 to 21% with a resolution of 0.1%. Oxygen concentration is detected via an electrochemical fuel cell with a permeable layer of electrodes that allow the flue oxygen molecules and reference air molecules to transfer ions, creating a voltage potential across the electrodes that can be interpreted as an O_2 concentration within the flue gases. Similarly, the CO concentration is also measured via an electrochemical fuel cell, but differs in that O_2 molecules that permeate the electrodes are

used to react with the CO on the opposite electrode to form CO_2 . This chemical reaction results in the consumption of O_2 on the reference side of the fuel cell and is used in conjunction with the electrode at the reaction location to obtain a voltage potential that can ultimately be interpreted as a concentration of CO . This results in a CO measurement in parts per million (ppm) from 0 - 30,000 at a resolution of 1 ppm. Operating on a similar principal as the CO sensor, an electrochemical fuel cell is used to determine the concentration of NO in a range of 0-3,000 ppm with a 1 ppm resolution. The CO_2 recorded by the Testo analyzer is estimated from the O_2 measurement and limited by the maximum theoretical value of CO_2 based on the fuel composition at the stoichiometric limit. The Testo sampling probe, placed in the exhaust gas stream, includes a thermocouple and inlet for flue gas sampling. To correct measurements for water condensation in the sampling line, the correction procedure of Richter *et al.* [1] is used, requiring a separate measurement of O_2 using a Bosch LSU 4.9 ZrO_2 wide-band oxygen/lambda sensor. Ambient moisture content and temperature are measured in real time with an Omega HX92B series humidity sensor and K-type thermocouple. Figure 3-6 shows a comparison of measured O_2 , CO , and NO between baseline and mixing pot cases.

3.3 Emissions Reduction Design Selection

3.3.1 Motivation for Design Selection

Many studies of experimental biomass combustion systems have demonstrated that increasing turbulent mixing, combustion gas temperatures, and residence time, results in lower harmful emissions due to the increased oxidation [24, 41-47]. The vast majority of the studies focus on small particle feed systems that can operate in a quasi-steady state. These types of systems are more easily optimized due to consistent burn rates. Batch type systems that use cord wood have a highly varied burn cycle with large changes in fuel burn rate and fuel composition due to typical variations in lignocellulosic fuel decomposition.

Given the current boiler design, non-reacting flow simulations demonstrate unmixed fuel and air streams progress to the bottom of the secondary chamber. These unmixed hot gas streams are then cooled when they hit the secondary chamber bottom, walls, and back exhaust tubes. Based on this, it is clear that the design could benefit from increased mixing in the secondary chamber. The design selection is based on several contributing improvements which work together to increase turbulent kinetic energy and aim to avoid the rapid quenching of the secondary chamber combustion products. Figure 3-4 shows the flow augmentation basket chosen as a proof of concept design. The basket is made of a low thermal capacity material, allowing for the rapid increase in material temperature approaching that of the gas temperature, thereby insulating it from the cooler secondary chamber walls, avoiding early cool-down. The shape is

designed to collect the hot gases within the basket promoting turbulent mixing of the fuel and air stream at high temperatures. Since gas is collected within a basket before being ejected from the side, the flow path and therefore the residence time is increased at higher temperatures. The anticipated overall effect of this design is to primarily reduce the *CO* emissions, which would increase combustion efficiency and lead to a small increase in thermal efficiency. This design selection is a simple modification for both the manufacturer and consumer, and over time could result in significant reduction in *CO* emissions.

3.4 Modification of Boiler and Performance Testing

3.4.2 Experimental Results

Experimental data taken with the mixing pot shows that it is most effective during high temperature peak burn rate portions of the burn. This observation indicates that this device would be most useful in situations where large fuel charges are used and high burn rates can be maintained. A narrow region of time between 0.5 - 1.5 hrs. (shaded region) shows the greatest increase in temperatures as seen in Figure 3-5(a) for the primary chamber gas temperature. In the primary chamber only a small increase in temperature is seen due to the relatively consistent nature of the burn. However, in the secondary chamber a larger increase in gas temperature is observed with a maximum at approximately 1700°F. This is a 41% difference compared to approximately 1200°F for the baseline case. This is due to the containment of the hot exhaust gas within the mixing pot, which increases the turbulent mixing and allows for greater heat release. This follows through to the exhaust where in Figure 3-5(c) a relatively significant increase in temperature is seen at the flue. This increase in gas temperature is beneficial for the oxidation of *CO* to *CO*₂. However, due to these higher temperatures, an increase in *NO* should also be expected.

A reduction in emissions is indicated in Figure 3-6(a), showing the *O*₂ reaching a lower concentration in the exhaust products between the baseline and mixing pot cases. A decrease in available oxygen by approximately 33% can be seen during the peak burn corresponding to the peak temperatures in the secondary chamber and flue. This rapid decrease in oxygen concentration is an indication of increased oxidation and corresponds to the decrease in *CO*. Figure 3-6(b) shows a comparison of *CO* emissions between the baseline case and the mixing pot. The decrease in *CO* is due to the high temperature and improved mixing conditions promoted by the mixing pot in the secondary chamber. The mixing pot clearly has a beneficial effect on the *CO* emissions by reducing the magnitude and duration of the first *CO* peak. However, this same effect results in a relatively small (12%) increase in peak *NO* emissions (see Figure 3-6(c)). Table 3.1 shows a comparison of overall mass percent emissions. As expected, the mixing pot

promotes oxidation and mixing, resulting in a difference in CO_2 of approximately 5.6%, NO approximately 7.4%, and CO approximately 14.3%.

3.4.3 Computational Simulations

A solid model of the EBW-200 wood boiler provided by Econoburn was converted to a triangulated surface mesh using Autodesk[®] Inventor software and implemented in the computational domain using a newly developed cut-cell approach [48]. Figure 3-7(a) shows the overall geometry of the combustion chambers. Fuel pyrolysis gases produced in the primary chamber (top) enter the secondary chamber (bottom) through a slot measuring 2.0 cm wide by 23.0 cm long. Figure 3-7(b) shows a view of the refractory connecting the top and bottom chambers. Air is blown into the refractory through two cylindrical ducts, 4.80 cm in diameter. The ducts branch into five tubes, 2.05 cm in diameter, that supply air to mix with pyrolysis gases before reaching the secondary chamber. The fuel-air mixture burns in the secondary combustion chamber and enters the stack through the exit port.

To explore the effects of modifying the secondary chamber, surface meshes of the mixing pot and several impact plate geometries are combined with the boiler surface mesh. Descriptions and simulations of the impact plate will be discussed later in Section 4.5 of this report. The mixing pot geometry is an elliptical shell with one open end and a wall thickness of 1.27 cm. The pot is 29.2 cm in height and 33.0 cm wide with a 12.06 cm diameter hole removed through the geometric center of one side. Figure 3-8 shows the combined secondary chamber and mixing pot meshes used in the simulation. The mixing pot is inserted into the secondary chamber with the open end of the pot centered under the slot. The opening allows the fuel-air mixture to accumulate and mix before entering the remaining space of the secondary chamber. The gases exit the mixing pot through the side hole and a 1.27 cm clearance gap between the top of the pot and the ceiling of the secondary chamber. Figure 3-9 shows a close-up view of the clearance gap.

The flow equations used to model this process are solved using block-structured, uniformly spaced, Cartesian meshes. To capture the geometry in the secondary chamber, a cut-cell description is used where cells that reside in the solid material are turned-off and internal boundaries are added. An appeal of a cut-cell description is avoiding the time intensive step of generating unstructured CFD meshes that closely follow the solid geometry. Figure 3-7(b) shows the Cartesian CFD domain and various boundary types used in the study. The upper y boundary and x-z dimensions of the space are defined to capture the extent of the enclosed air ducts, the slot located underneath the primary chamber, and the solid walls of the chamber. The overall height of the domain is selected to capture the solid floor of the chamber. The diameter of the air holes are small relative to the overall size of the overall computational domain, which is 0.52 m x 0.50

m x 0.59 m. To adequately resolve the disparity in length scales, a large number of grid cells (~3.5 million) are used - requiring the use of parallel computing. In this approach, the solution domain is decomposed into several blocks (100s) for parallel execution. These types of numerical simulations require specialized computer hardware made available through the use of the UB Center for Computational Research (CCR).

The technical approach is based on the use of CFD which solves modeled equations governing the fluid flow. The specific modeling approach pursued is Large Eddy Simulations (LES). In this approach, the Navier-Stokes equations are pre-filtered, resulting in the following system of equations describing mass, momentum, energy, and species conservation,

$$\text{Equation 3-1} \quad \frac{\partial \bar{\rho}}{\partial t} + \nabla \cdot (\bar{\rho} \tilde{\mathbf{u}}) = 0$$

$$\text{Equation 3-2} \quad \frac{\partial (\bar{\rho} \tilde{\mathbf{u}})}{\partial t} + \nabla \cdot (\bar{\rho} \tilde{\mathbf{u}} \tilde{\mathbf{u}}) = \nabla \cdot (-\bar{\mathbf{p}} \tilde{\mathbf{I}} + \tilde{\boldsymbol{\tau}} + \tilde{\mathbf{T}}_{uu}) + \bar{\rho} \tilde{\mathbf{g}}$$

$$\text{Equation 3-3} \quad \frac{\partial (\bar{\rho} \tilde{e}_t)}{\partial t} + \nabla \cdot (\bar{\rho} \tilde{\mathbf{u}} \tilde{h}_t) = \nabla \cdot (\tilde{\mathbf{T}}_{uh} + \tilde{\mathbf{T}}_{uu \cdot u} + \overline{\mathbf{u} \cdot \tilde{\boldsymbol{\tau}} - \bar{\mathbf{q}}}) - \sum_{m=1}^N h_{fm}^o \overline{\dot{\omega}_m'''} + \bar{\rho} \tilde{\mathbf{u}} \cdot \tilde{\mathbf{g}}$$

$$\text{Equation 3-4} \quad \frac{\partial (\bar{\rho} \tilde{Y}_m)}{\partial t} + \nabla \cdot (\bar{\rho} \tilde{\mathbf{u}} \tilde{Y}_m) = \nabla \cdot (\tilde{\mathbf{T}}_{uY_m} + \bar{\mathbf{q}}_m) + \overline{\dot{\omega}_m'''}_m$$

where, $\tilde{\phi}(\mathbf{x}) = \overline{\rho \phi} / \bar{\rho}$ represents a density weighted filtered quantity. In Equation 3-1 through Equation 3-4 $\bar{\rho}$ is the mixture density, $\tilde{\mathbf{u}}$ is the velocity, \bar{p} is the pressure, $\tilde{e}_t (= \tilde{h}_t - \tilde{R}\tilde{T})$ is the total resolved energy, \tilde{Y}_m is the mass fraction of m^{th} species, and $\tilde{h}_t (= \tilde{h} + \tilde{\mathbf{u}} \cdot \tilde{\mathbf{u}}/2)$ is the total enthalpy including the resolved sensible enthalpy (\tilde{h}) and kinetic energy. The filtered viscous stress tensor ($\tilde{\boldsymbol{\tau}}$), species diffusion (\mathbf{q}_m), and heat fluxes ($\bar{\mathbf{q}}$) may be modeled using Newton's, Fick's, and Fourier's laws, respectively, in terms of resolved quantities, thereby neglecting subgrid fluctuations. The remaining second-order correlation quantities, $\tilde{\mathbf{T}}_{\alpha\beta}$, in Equation 3-2 through Equation 3-4 represent unknown sub-grid scale correlation for variables α and β , and are defined as: $\tilde{\mathbf{T}}_{\alpha\beta} \equiv -\bar{\rho}(\overline{\alpha\beta} - \tilde{\alpha}\tilde{\beta})$. An abundance of models are currently available for closing these terms and taken from the open literature. The final term, $\overline{\dot{\omega}_m''}'_m$, in Equation 3-3 and Equation 3-4 accounts for the average production/destruction of species due to chemical reactions. It is the modeling of this term which poses the greatest challenge to combustion simulation because of its exponential dependence on temperature.

It is important to have an adequate description of the inlet/outlet boundaries of the computational domain. Figure 3-7(b) shows colored outlines of the boundaries used in the study. The Econoburn EBW-200 uses a blower to inject air into the two central ducts. Cold flow testing of the EBW-200 flow system by Econoburn

provided a blower flow rate of 150 cfm. Using this volumetric flow rate and the cross-sectional area of the ducts, an entrance velocity of 2.75 m/s was calculated and imposed on the blower inlet boundaries (yellow) of the CFD domain. A second inlet boundary (yellow) is imposed above the slot connecting the primary and secondary chambers. This boundary contains material property descriptions of the pyrolysis gases obtained experimentally. The downward velocity of the gas into the chamber was set to a constant velocity of 7.0 m/s. This velocity was selected based on measurements captured using a high-speed camera, Figure 3-10 shows a representative image of the jet from experiments. The outlet boundary (red) is set to open with corresponding stagnation properties that allow gas mixtures to freely exit the secondary combustion chamber. The remaining boundary conditions are treated as isothermal walls (black) with temperatures of 300 K. A constant room temperature was selected to simulate a cold run of the boiler.

Cold-flow CFD simulations for the baseline impact plate and mixing pot geometries were carried out over 3.00 sec of physical time. Time averaged statistics are collected by running the simulations over a total of 2.50 sec of physical time with samples taken every 3.7 ms and 2.8 ms for the impact plate and mixing pot, respectively. Gathering of statistics starts after 0.50 sec of physical time to allow for initial flow transients to wash downstream. A total of 54,000 and 71,400 statistics are therefore gathered over the baseline and mixing pot cases, respectively, for approximately 10 flow-through times. A typical run takes 7 days employing 128 processors (21,504 CPU hours) for the flow to develop and take enough samples to obtain time-averaged mean and RMS statistics of flow quantities.

Figure 3-11 shows time-averaged snapshots of the flow using the baseline impact plate geometry. Centerline slices in Figure 3-11(a) and (b) show the mean mixture fraction and outlines of the impact plate. In the baseline model, the fuel-air jet issued from the primary chamber travels downstream and impinges on the inclined surface of the impact plate. Higher concentrations of mixture fraction found in the front and sides of the chamber suggest that the baseline impact plate tends to direct the fuel-air mixture into these regions. Flow directed down the incline circulates in a pocket between the front of the impact plate and the front chamber wall. Similarly, flow directed to the sides of the boiler circulates in the space between the sides of the impact plate and the chamber walls. Figure 3-12(a) and Figure 3-12(b) show isocontours of the stoichiometric mixture fraction colored by Turbulent Kinetic Energy (TKE). Two counter-rotating vortex structures form between the sides of the impact plate and chamber walls, which are driven by oncoming streams of fuel-air mixture flowing off the sides of the impact plate. Peak TKE levels, indicating rapid changes in flow velocity, occur in the shear layers of the jet and regions of flow separation at the edges of the impact plate. Figure 3-11(c) and Figure 3-11(d) show RMS mixture fraction at centerline slices in the chamber. Low levels of RMS mixture fraction are found in the cores of the vortex pairs, indicating the fuel-

air mixture is well mixed in these regions. By contrast, high levels of RMS mixture fraction indicate poor mixing of fuel and air at the front of the boiler. The highest levels of turbulent mixing in this configuration are due to the circulation regions established by the impact plate.

Figure 3-13 shows time-averaged snapshots of the flow using the mixing pot geometry. Centerline slices in Figure 3-13(a) & (b) show the mean mixture fraction and outlines of the mixing pot. In this configuration, the fuel-air jet issued from the primary chamber travels downstream before impinging on the bottom of the mixing pot. The pot fills with fuel-air mixture and continuous impingement of the jet causes chaotic turbulent mixing. The fuel-air mixture exits through the hole in the side of the mixing pot or rises to the ceiling of the chamber and escapes through the clearance gap. Flow exiting the hole forms a secondary circular jet that impinges on the opposing chamber wall, which directs flow towards the adjacent sides of the chamber. Flow exiting through the gap travels along the ceiling of the chamber, extending in every direction. High concentrations of mixture fraction in the region surrounding the secondary jet indicates biasing of flow to the side of the chamber opposing the hole, contrasted to low concentrations found on the opposing side where no hole is present. Similarly, higher concentrations of mixture fraction are observed on the ceiling of the chamber due to the gap, contrasted to lower concentrations on the floor of the chamber. Figure 3-14(a) & Figure 3-14(b) show an isocontour of the stoichiometric mixture fraction colored by TKE. Peak TKE values are found in the secondary jet and correspond to flow separation occurring at the hole in the mixing pot geometry. Figure 3-13(c) & Figure 3-13(d) show centerline slices of the RMS mixture fraction. Low levels of RMS mixture fraction occur in the inside of the mixing pot region, indicating high levels of mixing and air-fuel homogeneity. By contrast, low levels of turbulent mixing are present outside of the mixing pot and in the region where the secondary jet impinges on the opposing chamber wall. This can be attributed to the fact that the most highly turbulent flows in the chamber are contained within the mixing pot geometry, which prevents influence on surrounding space in the chamber. The highest levels of turbulent mixing in this configuration are due to the chaotic flow established inside of the mixing pot geometry.

Figure 3-15 shows probability density functions (PDF) of mixture fraction throughout the computational domain for the baseline and mixing pot configurations. The PDF is a metric used to evaluate the effectiveness of mixing in the secondary chamber. Data samples were collected in 5 ms intervals for a total of 50 ms after flow transients were sufficiently washed away. Mixture fraction values of zero and unity on the horizontal axis indicate points in the domain where only air and fuel are found, respectively. The vertical axis shows the relative frequency of points in the domain corresponding to the mixture fraction values. The theoretical average mixture fraction was calculated to be 0.77 based on the mass flow rates of fuel and air

into the secondary chamber. This corresponds to a mixture fraction where ideal mixing of fuel and air occurs. The PDF for the mixing pot shows a peak relative frequency at a mixture fraction of 0.66, while the baseline case shows a peak at 0.15. This indicates a greater probability that the mixture fraction throughout the secondary chamber is closer to the ideal value than the baseline case. This suggests that better mixing is achieved with the mixing pot than the baseline design, as supported by the experimental results. CFD simulations in earlier discussions revealed significantly lower RMS mixture fraction inside of the mixing pot than in the baseline chamber. This suggests that the improvement in fuel-air homogeneity, increase in gas temperatures, and reduction in emissions is due to the highly turbulent mixing taking place within the mixing pot.

3.5 Impact Plate Geometry Optimization and Minimization of CO

Different configurations of the impact plate were simulated using CFD to explore its fundamental role on turbulent mixing in the secondary chamber. Figure 3-7 shows a mesh of the empty secondary chamber included for comparison to demonstrate the effects of including the baseline impact plate. The baseline impact plate shown in Figure 3-16 is a triangular prism with a 4° angle of inclination towards the front wall of the chamber. The plate is 25.4 cm wide by 38.1 cm deep. The front and back of the plate measure 2.54 cm and 5.08 cm in thickness, respectively. Two additional variations of the impact plate design are shown in Figure 3-17 & Figure 3-18. These meshes use 11° and 18° angles of inclination towards the front wall of the chamber and were selected to explore the role of the plate angle on turbulent mixing. Figure 3-19 & Figure 3-20 show configurations of the impact plate with 4° inclines facing the side and exit port of the chamber. The plate angled towards the exit port of the chamber has the same dimensions as the baseline model, but faces the opposite direction. The plate angled towards side facing the chamber wall has front and back thicknesses of 2.54 cm and 5.08 cm, which produce a 4° angle of inclination in the direction of the positive x-axis. These two configurations are used to compare with the baseline impact plate design to explore the effects of changing the direction of the incline.

Cold-flow CFD simulations for the baseline impact plate and mixing pot geometries were carried out over 3.00 sec of physical time. Time averaged statistics are collected by running the simulations over a total of 2.50 sec of physical time. Table 3.2 shows a summary of the statistic time intervals and total number of samples taken for all configurations in the study. Gathering of statistics starts after 0.50 sec of physical time to allow for initial flow transients to wash downstream.

Figure 3-21 and Figure 3-22 show time-averaged snapshots of the flow using impact plates geometries at varying angles of inclination. Centerline slices show the mean mixture fraction and outlines of the impact

plates. In the empty chamber configuration, the fuel-air jet impinges on the flat floor of the secondary chamber. High concentrations of mixture fraction are found along the floor and walls, where the flow travels uninterrupted. The variations using 11° and 18° angles redirect the fuel-air mixture to the front of the chamber in the same manner as the baseline model. Increasing angles result in higher concentrations of mixture fraction at the front of the chamber and lower concentrations near the exit port. The steeper incline prevents portions of the fuel-air mixture from spilling over the rear end of the impact plate and instead encourages accumulation near the front. Figure 3-23 and Figure 3-24 show an iso-contour of the stoichiometric mixture fraction colored by TKE. Increasing angles also increase the diameter of the vortex structures forming on the sides of the plates, resulting in the formation of cone-like vortexes. The cone structure is driven by flows running off the sides of the impact plate at increasing heights. Peak TKE values for all configurations are observed in the shear layers of the jet and the edges of the impact plates. Figure 3-25 and Figure 3-26 show centerline slices of the RMS mixture fraction. In the configuration without an impact plate, high RMS mixture fraction are found throughout the chamber, indicating poor mixing. For the cases with impact plates, the RMS mixture fraction increases within the vortex structures as the plate angle increases. Since the diameters of the vortexes increase with the plate angle, this leads to a decrease in rotational speed and consequently reduced mixing effectiveness. However, this also results in a decrease in RMS mixture fraction in the remaining regions of the chamber indicating improved mixing in those areas. This is due to the increase in rotational speed of the remaining regions due to the closer proximity of the impact plate at higher angles.

Figure 3-27 and Figure 3-28 show time-averaged snapshots of the flow using impact plate geometries in varying directions. Centerline slices show the mean mixture fraction and outlines of the impact plates. The backwards and sideways impact plates form larger circulation regions at the front of the chamber due to the larger plate thicknesses in these regions. Mixture fraction concentrations show no significant deviations from what is observed in the baseline case in the front and rear of the chamber. The sizes of the vortex structures formed in the backwards case are identical to those in the baseline case since the geometries are the same. In the sideways variation, the flow is biased to the side of the chamber opposing the angle of inclination on the impact plate as evidenced by high mixture fraction concentrations. Figure 3-29 and Figure 3-30 show isocontours of the stoichiometric mixture fraction colored by TKE. For the backward and sideways plates, peak TKE values are also found in the jet and at the plate edges. Figure 3-31 and Figure 3-32 show centerline slices of the RMS mixture fraction. No significant differences between the baseline impact plate and backwards plates are observed in mixing. In the sideways facing case, the differences in plate thicknesses create two vortex pairs with different diameters.

Probability density functions (PDF) of mixture fraction throughout the computational domain were created for the various impact plate configurations. Data samples were collected in 5 ms intervals for a total of 50 ms after flow transients were sufficiently washed away. Table 3 shows a summary of the mixture fractions at the peak probability across all configurations. Figure 3-33 shows PDF comparisons for the empty chamber case and the baseline impact plate. Compared to the boiler with no impact plate, the 4° angle is shown to shift the mixture fraction at peak probability towards the ideal mixture fraction. Figure 3-34 shows PDF comparisons for cases with varying plate angles of inclination. For the impact plate cases facing the front of the secondary chamber, an increase in the angle of inclination results in mixture fractions at peak probability shifting closer to the ideal. However, increasing the angle beyond 11° results in a decrease in mixture fraction at peak probability, shifting away from the ideal. Figure 3-35 shows PDF comparisons for cases with changing directions of the impact plate. In configurations where the direction of the plate was changed, it is observed that there is little change in the mixture fraction at peak probability for all three cases. CFD simulations in earlier discussions revealed lower RMS mixture fraction fluctuations in the cases with smaller angles of inclination due to the differences in vortex structures created by the impact plate. In addition, the steepest angle of inclination was also shown to pool larger concentrations of fuel near the front of the boiler since the geometry inhibited the gases from flowing freely. This suggests that the improvement in fuel-air homogeneity and mixing is due to how well the vortex structures mix the fuel and air, as well as how effectively the mixture is able to travel to the exit port. Similarly, for the case with varying plate directions, no significant change in mixing was noted. This is likely due to no major changes in the mixing behavior of the vortex structures at the plate edges.

3.6 Conclusion

In summary, the mixing pot design is chosen as a low cost, low maintenance secondary flow augmentation device for reducing harmful emissions. The increase of gas temperatures, residence time, and fuel/air mixing is the primary goal of the design selection. A comparison of experimental temperature data was shown, and the results indicate the device is successful in increasing gas temperatures. Experimental measurements of emissions also demonstrate that overall CO is reduced by 14.3%. However, the increase in temperature comes with the undesirable yet lesser effect of increasing NO by approximately 7.4%. Determination of whether the device produced an increase in residence time and mixing was explored through secondary chamber modeling. It should also be noted that at this point, the overall effect on thermal efficiency is unclear, however in theory the increased oxidation of CO would increase the combustion efficiency which would have a beneficial effect on thermal efficiency.

Computational simulations show an increase in mixing with the presence of the mixing pot in the secondary chamber. The primary mechanism of emissions reduction is the violent turbulent mixing occurring within the pot that does not occur in the baseline design. In the impact plate optimization, an increase in plate angle corresponded to an increase in effective fuel mixing for the 11° case, but a decrease in mixing for the 18° case. Changes in the direction of the baseline impact plate showed no significant changes in mixing.

Table 3.1. Comparison of Total Emissions With and Without Mixing Pot [%wt]

	no mixing pot (baseline)	mixing pot
<i>CO₂</i>	5.77	6.10
<i>CO</i>	0.30	0.26
<i>NO</i>	0.0026	0.0028

Table 3.2. Summary of Statistics Across All Simulations

case	sampling interval (10^{-5} s)	No. of samples
<i>Empty Chamber</i>	2.80	89,285
<i>Mixing Pot</i>	5.00	50,000
<i>Plate (4°, Front)</i>	3.70	67,567
<i>Plate (11°, Front)</i>	6.00	41,666
<i>Plate (18°, Front)</i>	2.80	89,285
<i>Plate (4°, Back)</i>	3.80	71,428
<i>Plate (4°, Side)</i>	3.80	71,428

Table 3.3. Summary of Mixture Fractions at Peak Probability

case	Z_{peak}
<i>Empty Chamber</i>	0.13
<i>Mixing Pot</i>	0.66
<i>Plate (4°, Front)</i>	0.15
<i>Plate (11°, Front)</i>	0.26
<i>Plate (18°, Front)</i>	0.12
<i>Plate (4°, Back)</i>	0.10
<i>Plate (4°, Side)</i>	0.12

Figure 3-1. Experimental Schematic

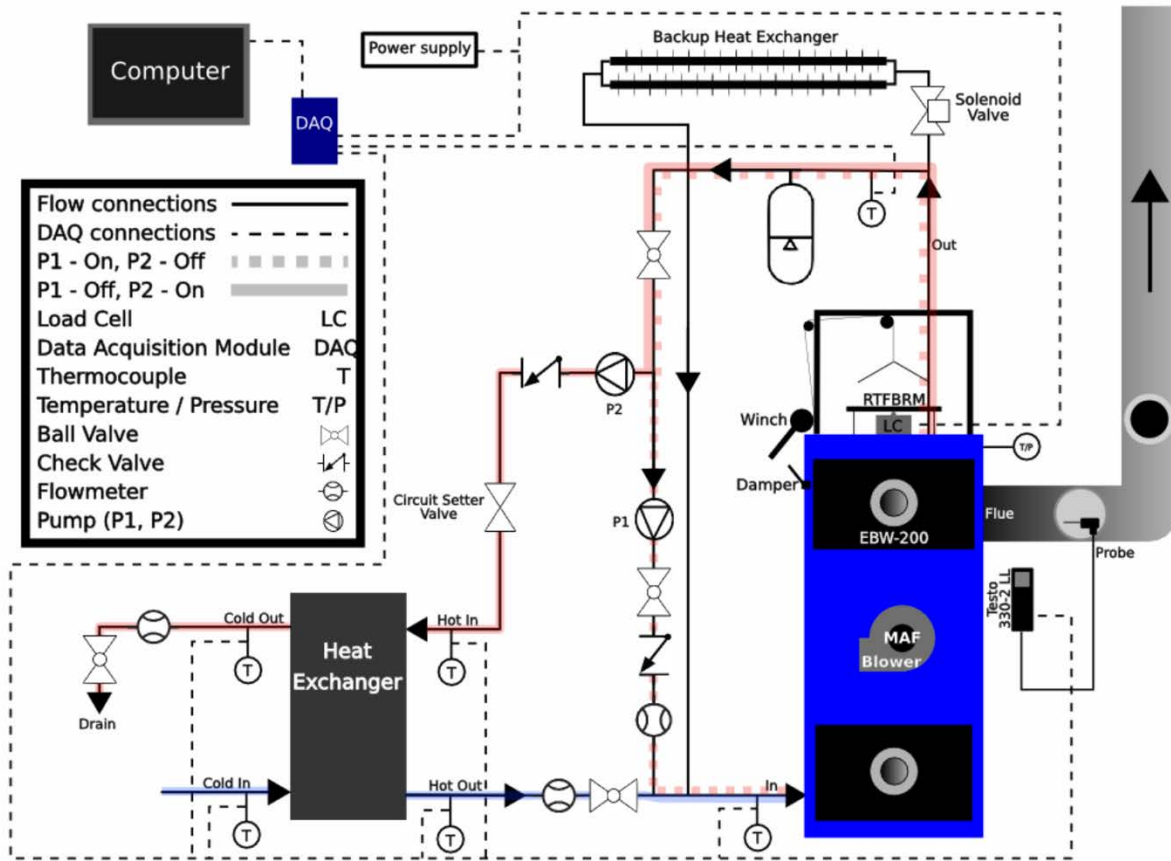


Figure 3-2. Real Time Fuel Burn Rate Monitor with Hanging Basket

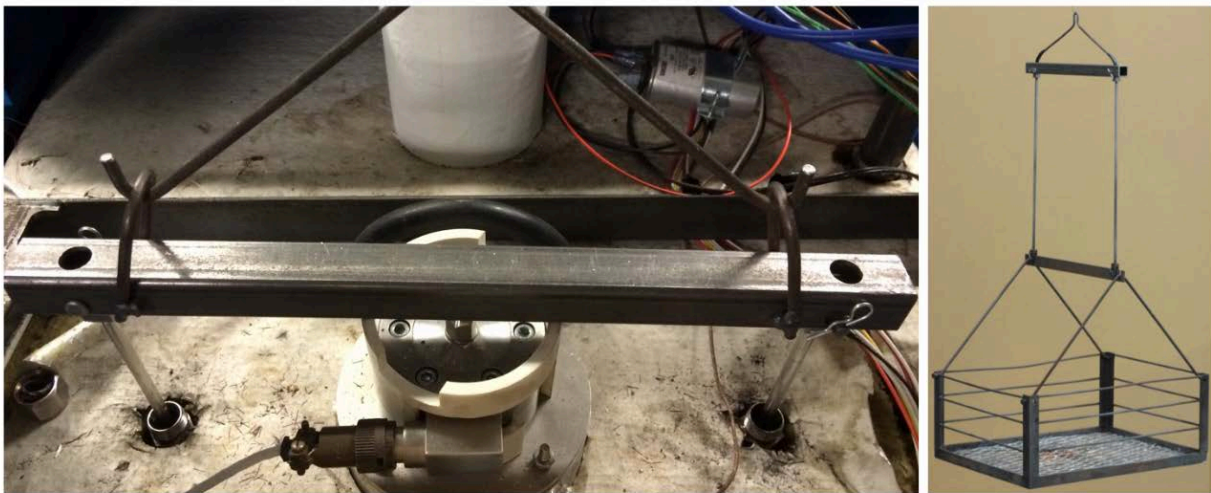


Figure 3-3. Cutaway View of Econoburn Two-Stage Hydronic Heater

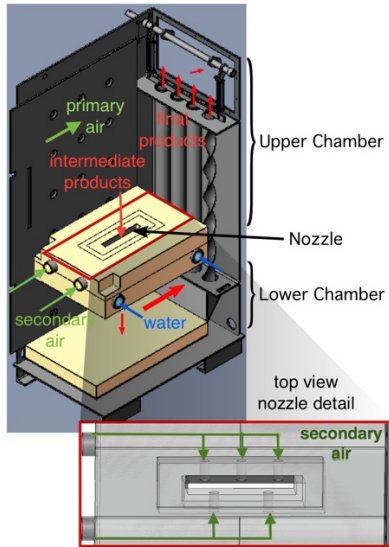
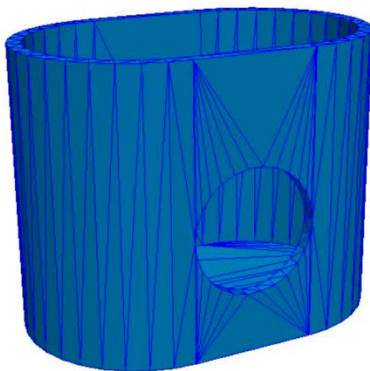


Figure 3-4. Physical and Computational Model of Mixing Pot

Mixing pot (a) picture (used in experiment) (b) CFD model.



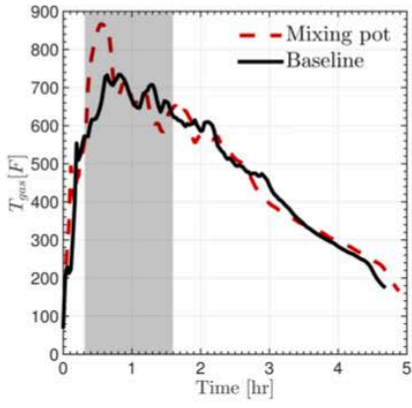
(a)



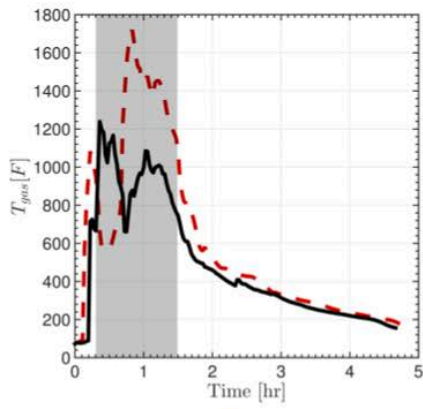
(b)

Figure 3-5. Gas Temperature Measurements

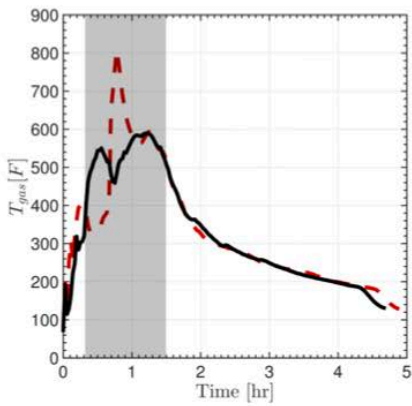
Comparison of gas temperatures between baseline and mixing pot runs for (a) primary chamber, (b) secondary chamber and (c) flue.



(a)



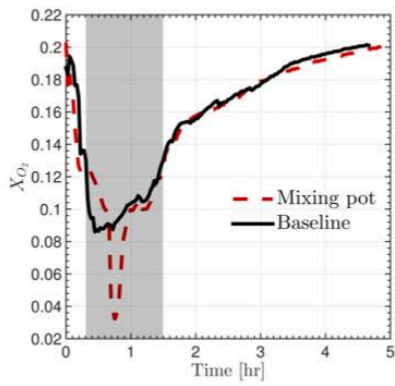
(b)



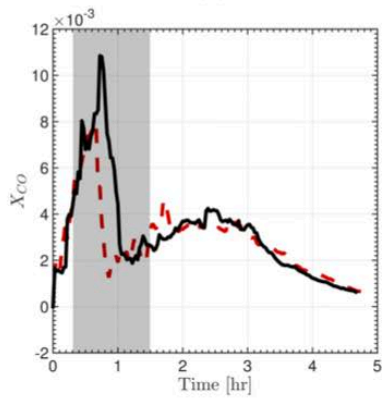
(c)

Figure 3-6. Emission Measurements

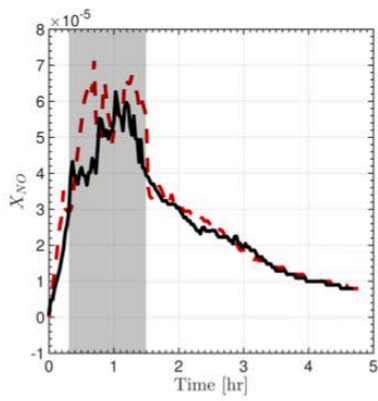
Comparison of gas species between baseline and mixing pot runs at flue for (a) O₂ (b) CO and (c) NO.



(a)



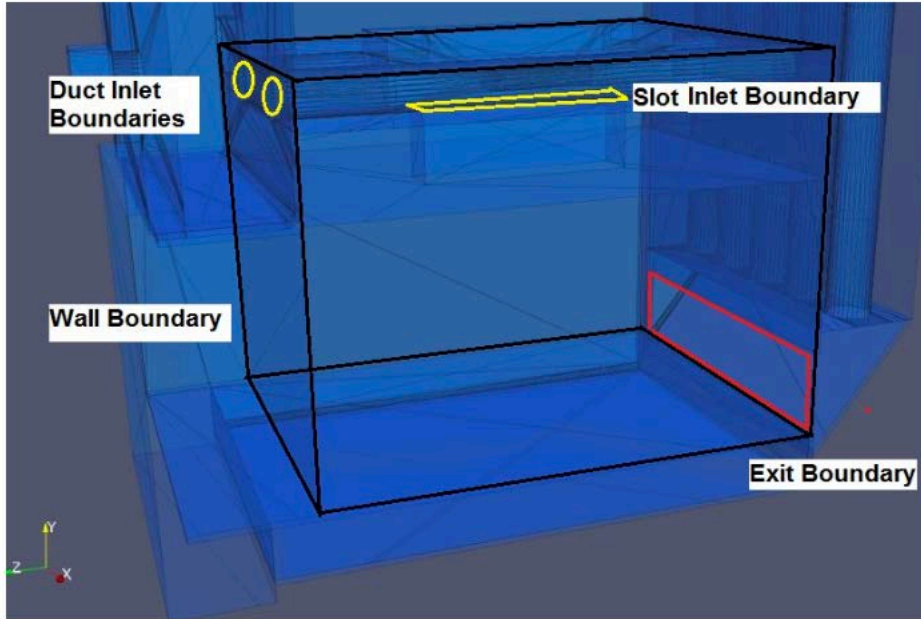
(b)



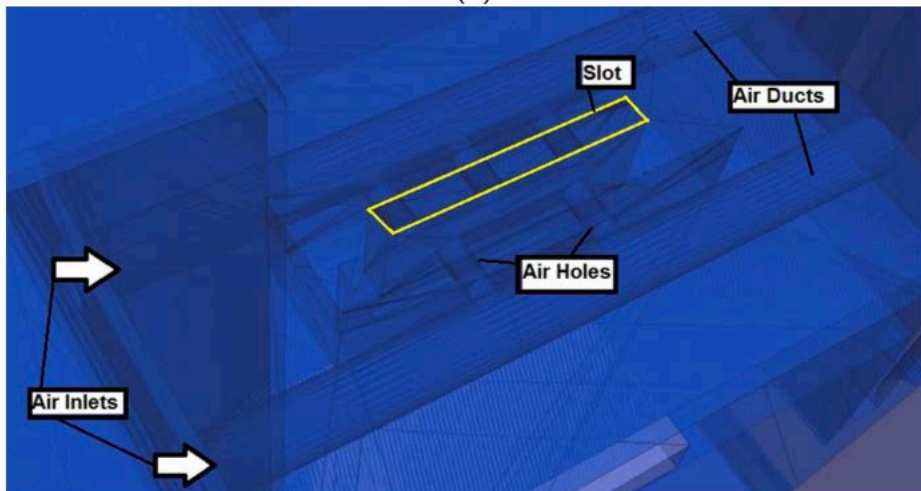
(c)

Figure 3-7. CFD Domain of Econoburn

Sketch of the CFD domain for lower chamber of Econoburn boiler showing (a) outline of domain and (b) air hole detail in boiler refractory.



(a)



(b)

Figure 3-8. Econoburn Boiler Mesh with Mixing Pot

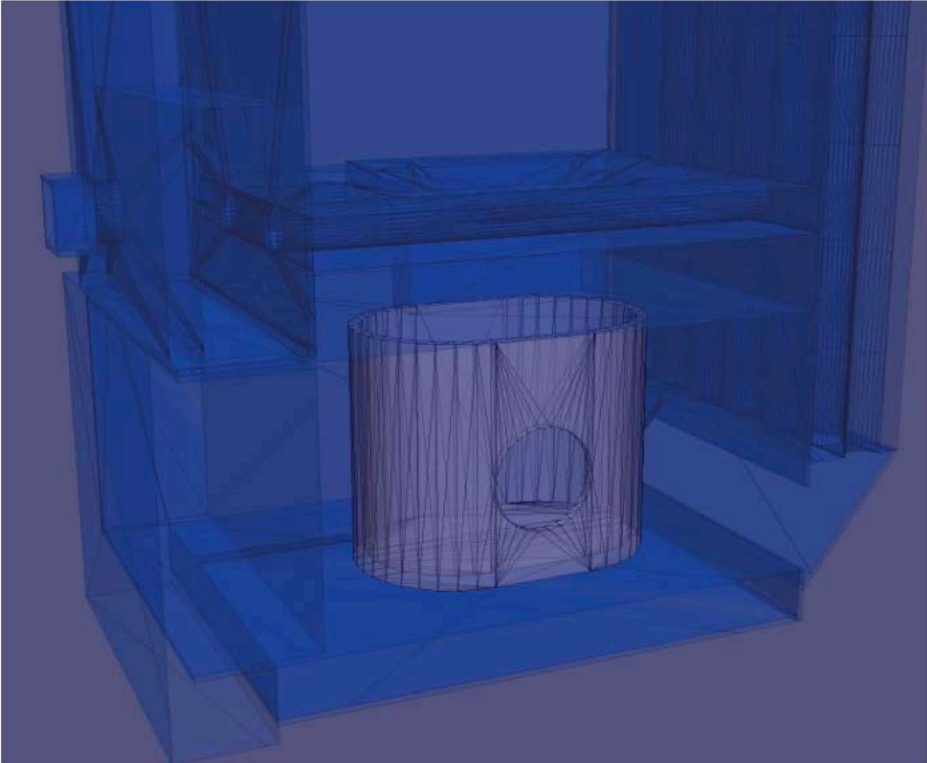


Figure 3-9. Mixing Pot Clearance Gap

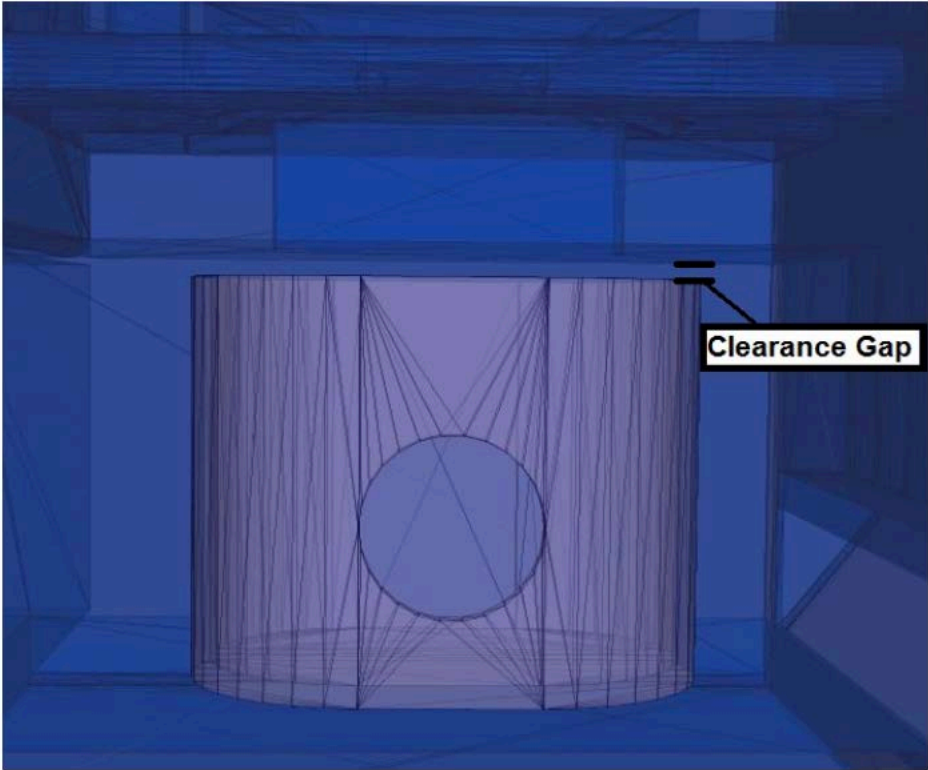
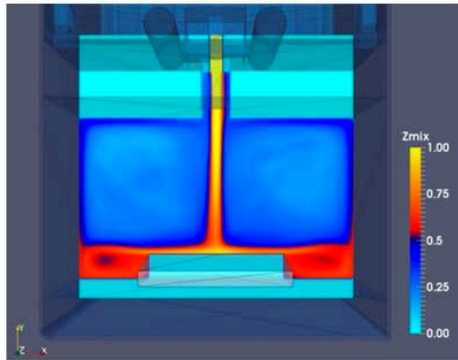


Figure 3-10. High-speed Camera Image of Air-fuel Jet

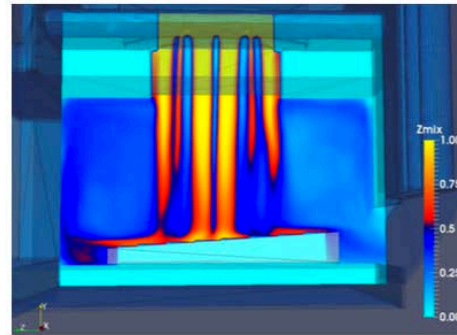


Figure 3-11. Average and RMS Mixture Fraction of Baseline Case

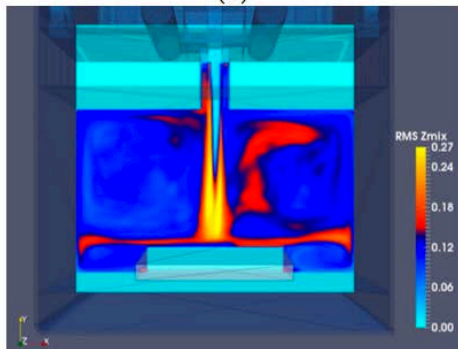
Centerline slices of the baseline case showing average mixture fraction (a) front, (b) side, and RMS mixture fraction (c) front, (d) side.



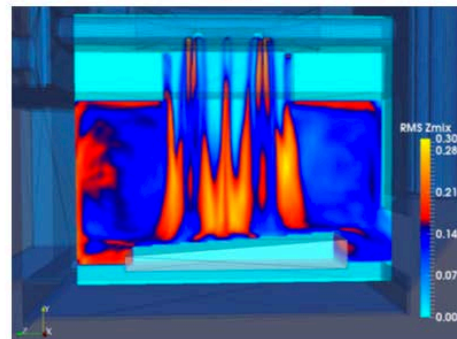
(a)



(b)



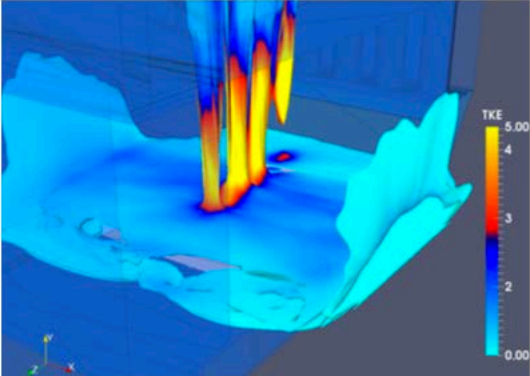
(c)



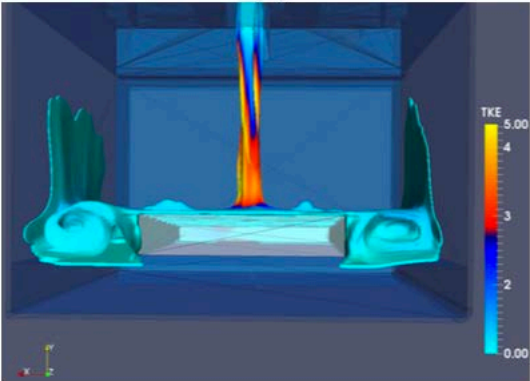
(d)

Figure 3-12. TKE in Baseline Case

Contours of stoichiometric mixture fraction in the baseline case colored by TKE.



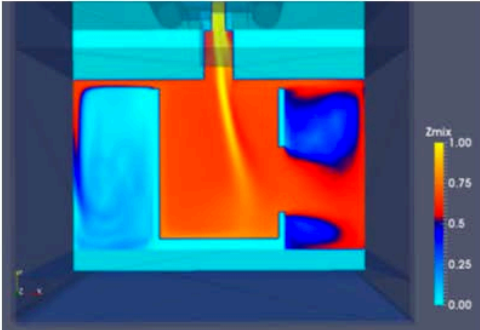
(a)



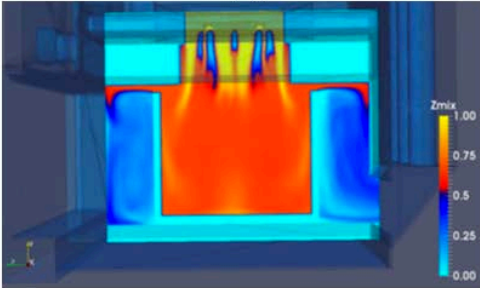
(b)

Figure 3-13. Average and RMS Mixture Fraction of Mixing Pot Case

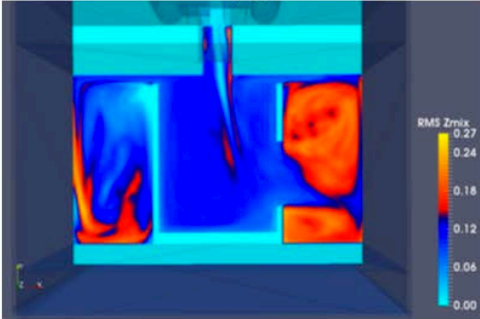
Centerline slices of the mixing pot case showing average mixture fraction (a) front, (b) side, and RMS mixture fraction (c) front, (d) side.



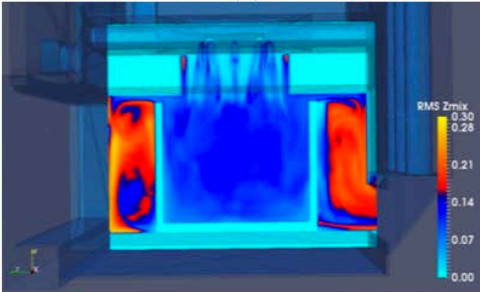
(a)



(b)



(c)



(d)

Figure 3-14. TKE in Mixing Pot Case

Contours of stoichiometric mixture fraction in the mixing pot case colored by TKE.

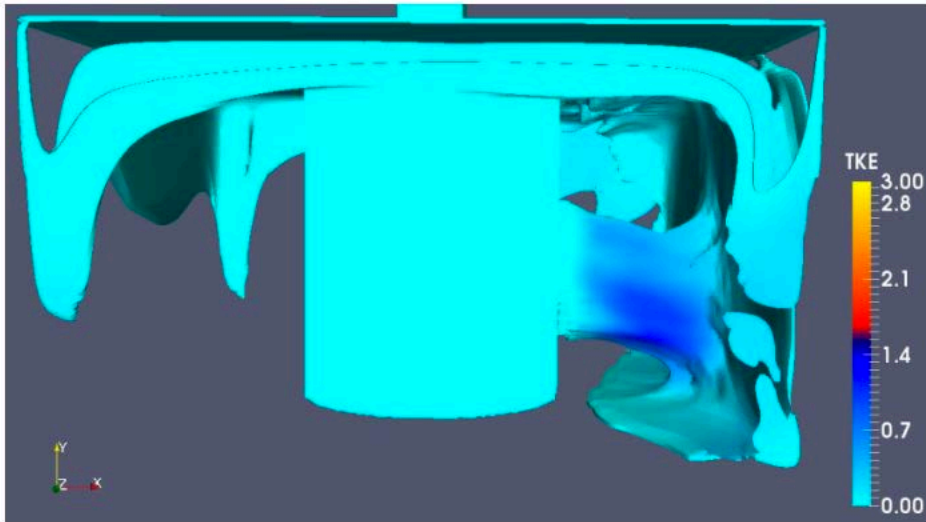


Figure 3-15. PDF Comparisons Between Baseline and Mixing Pot Cases

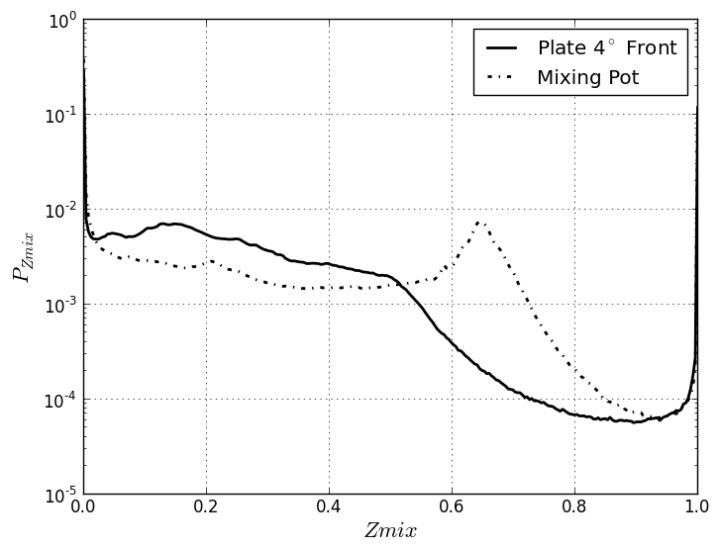


Figure 3-16. Mesh Use In Forward 4° Angle of Inclination Case



Figure 3-17. Mesh Use In Forward 11° Angle of Inclination Case

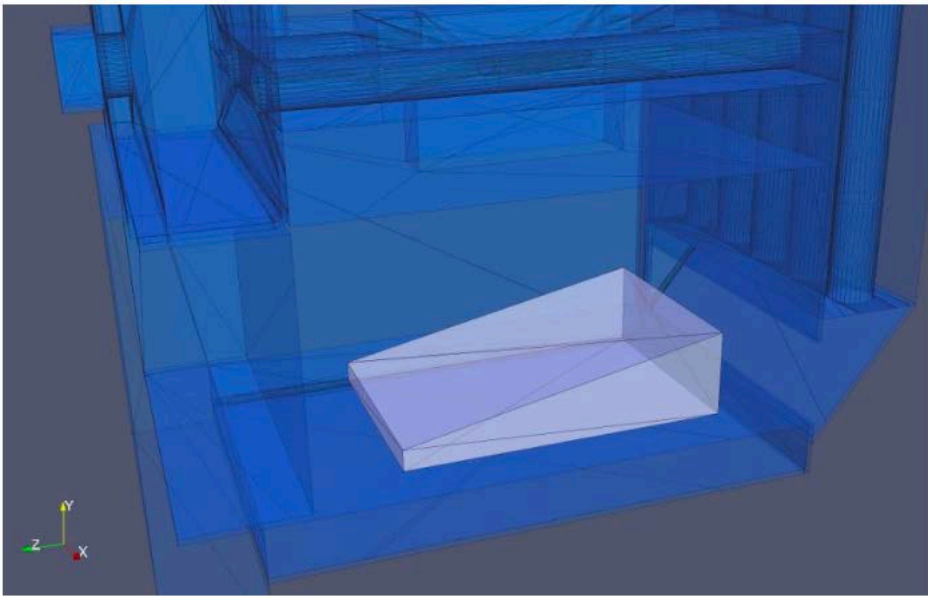


Figure 3-18. Mesh Use In Forward 18° Angle of Inclination Case

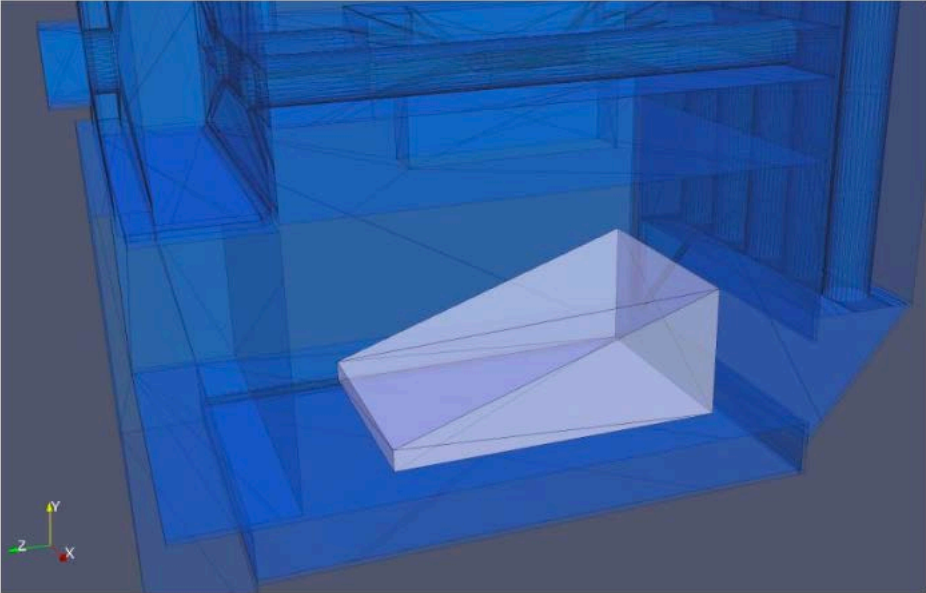


Figure 3-19. Mesh Use In Sideways 4° Angle of Inclination Case

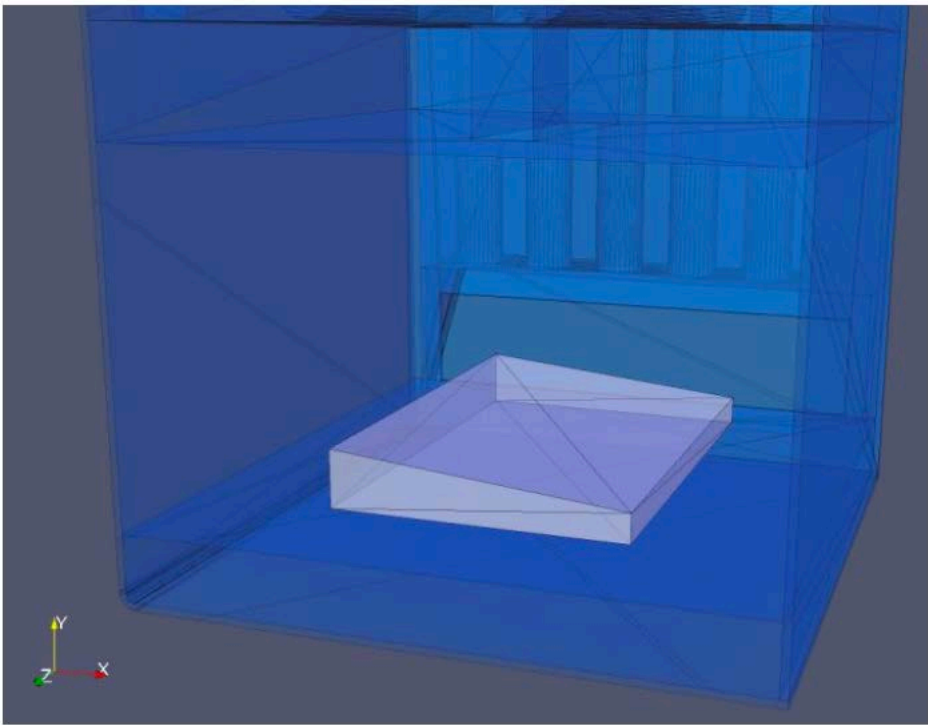


Figure 3-20. Mesh Use In Backward 4° Angle of Inclination Case

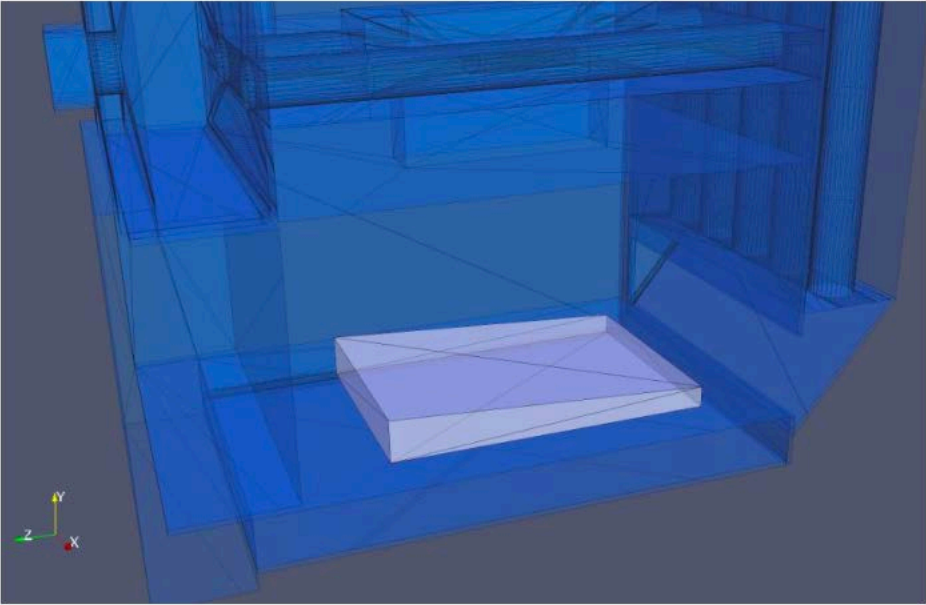
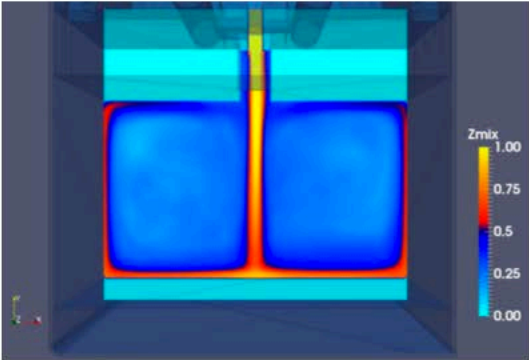
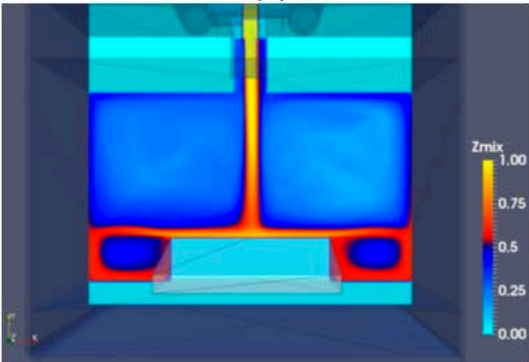


Figure 3-21. Average Mixture Fraction for Empty, 11°, and 18° Cases (Front)

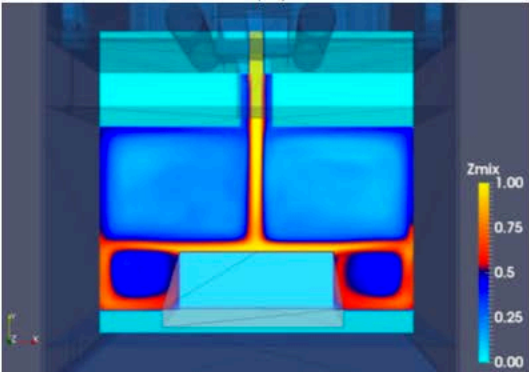
Z-axis slices showing average mixture fraction in the (a) empty, (b) 11°, and (c) 18° cases.



(a)



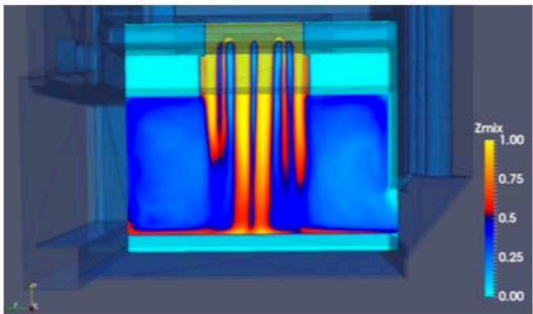
(b)



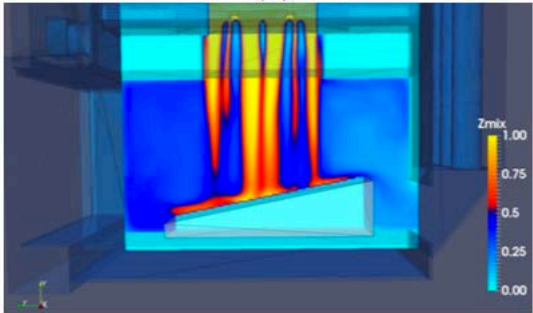
(c)

Figure 3-22. Average Mixture Fraction for Empty, 11°, and 18° Cases (Side)

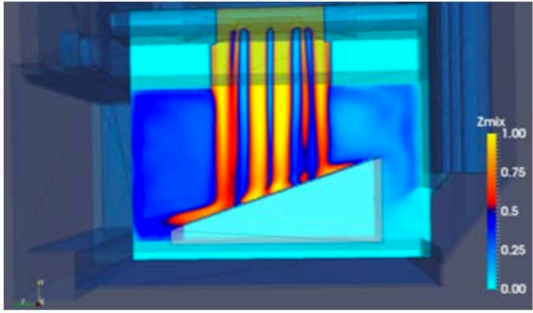
X-axis slices showing average mixture fraction in the (a) empty, (b) 11°, and (c) 18° cases.



(a)



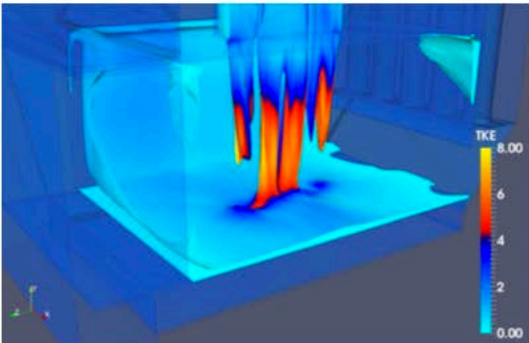
(b)



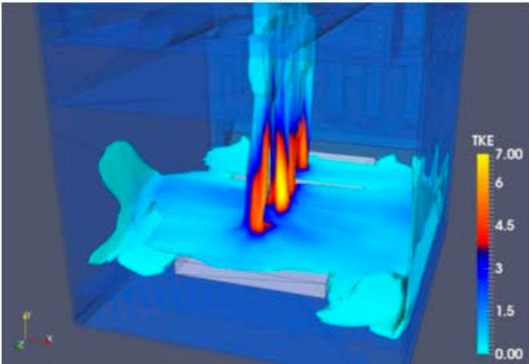
(c)

Figure 3-23. TKE in Empty, 11°, and 18° Cases

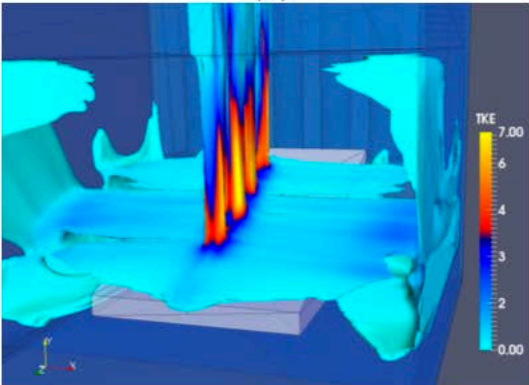
Isocontours of stoichiometric mixture fraction colored by TKE for the (a) empty, (b) 11°, and (c) 18° cases.



(a)



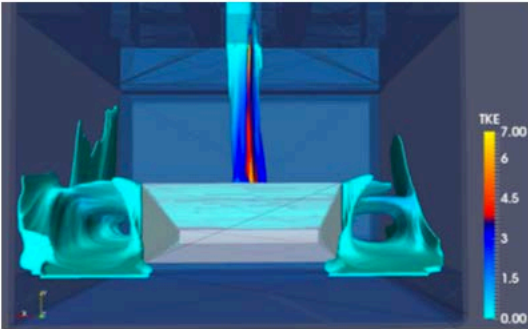
(b)



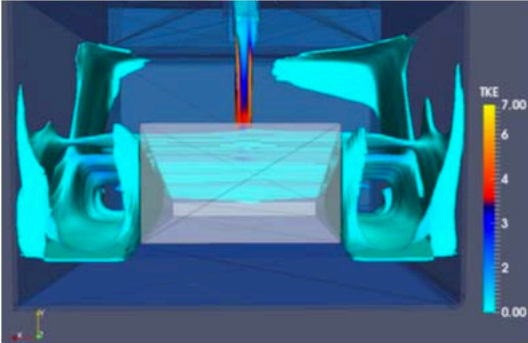
(c)

Figure 3-24. TKE and Vortex Formation in Empty, 11°, and 18° Cases

View from rear of boiler detailing vortex formation in the (a) empty, (b) 11°, and (c) 18° cases.



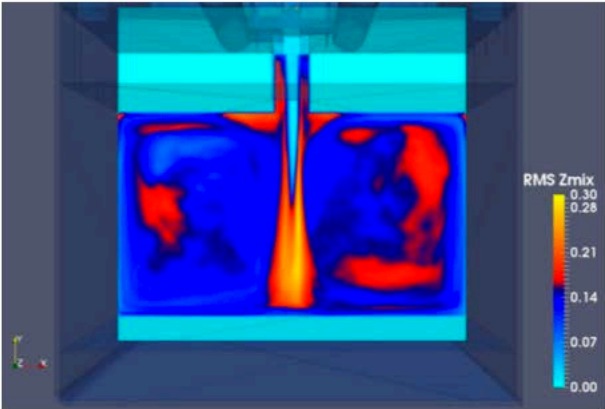
(a)



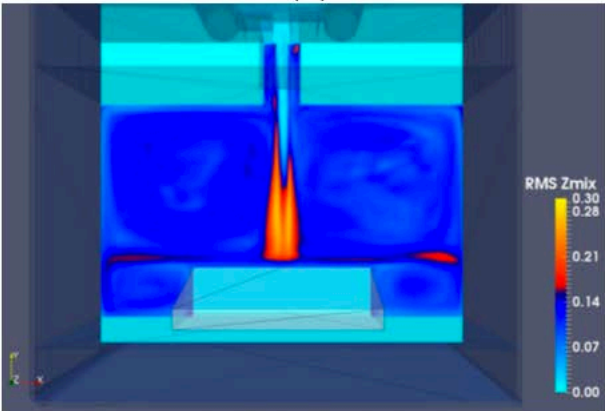
(b)

Figure 3-25. RMS Mixture Fraction in Empty, 11°, and 18° Cases (Front)

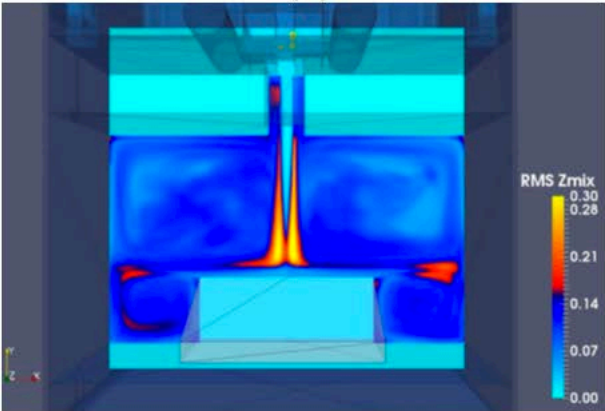
Z-axis slices showing RMS mixture fraction in the (a) empty, (b) 11°, and (c) 18° cases.



(a)



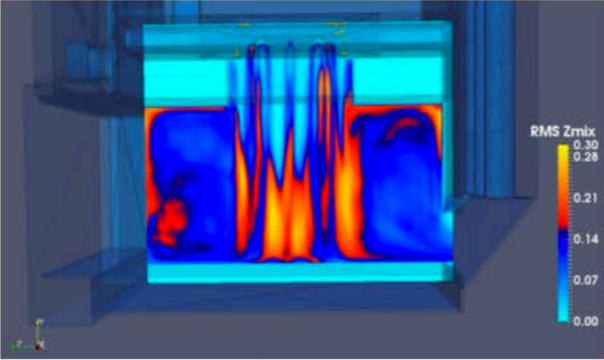
(b)



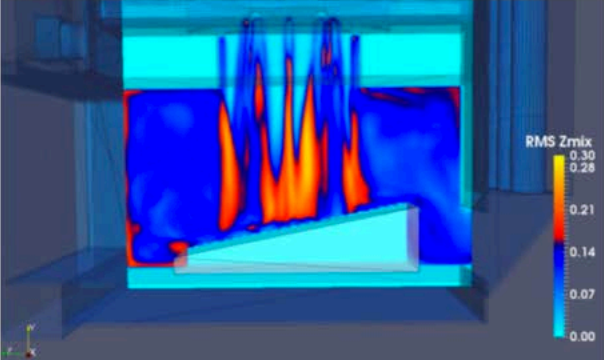
(c)

Figure 3-26. RMS Mixture Fraction in Empty, 11°, and 18° Cases (Side)

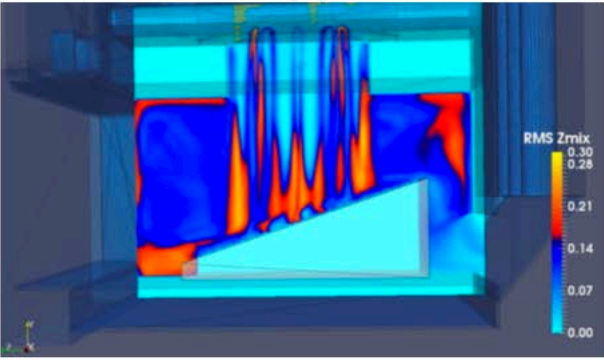
X-axis slices showing RMS mixture fraction in the (a) empty, (b) 11°, and (c) 18° cases.



(a)



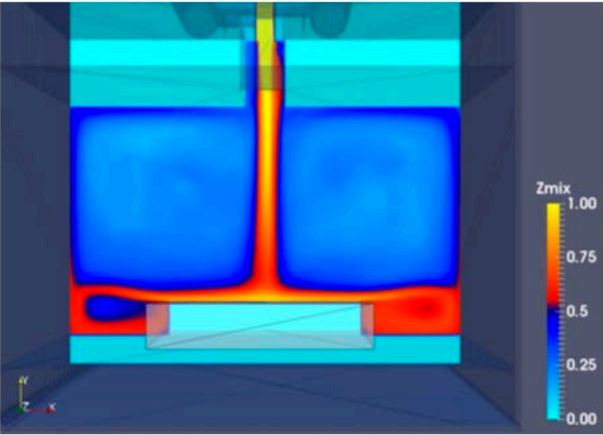
(b)



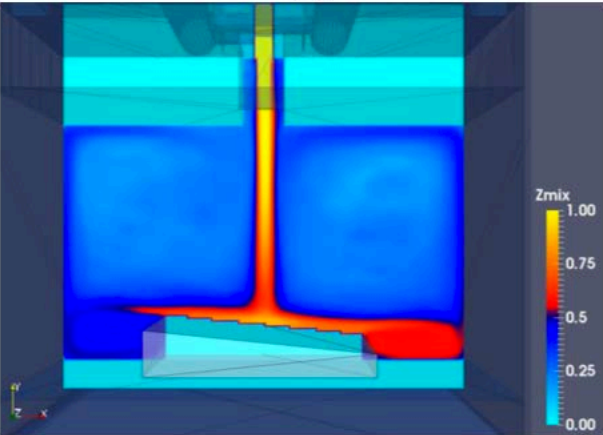
(c)

Figure 3-27. Average Mixture Fraction in 4° Backward and Sideways Cases (Front)

Z-axis slices showing average mixture fraction in the 4° (a) backwards and (b) sideways cases.



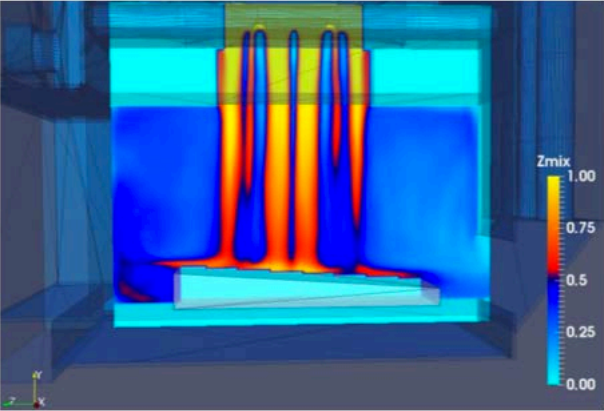
(a)



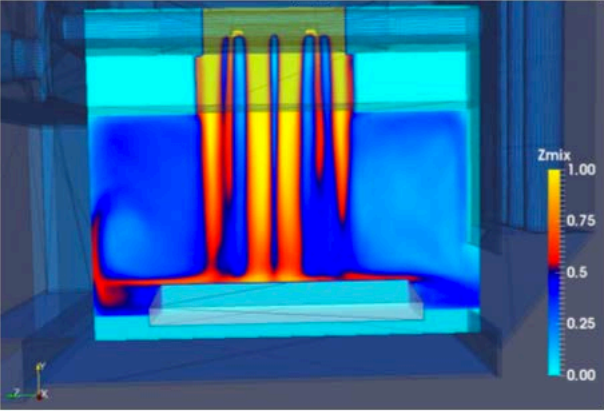
(b)

Figure 3-28. Average Mixture Fraction in 4° Backward and Sideways Cases (Side)

X-axis slices showing average mixture fraction in the 4° (a) backwards and (b) sideways cases.



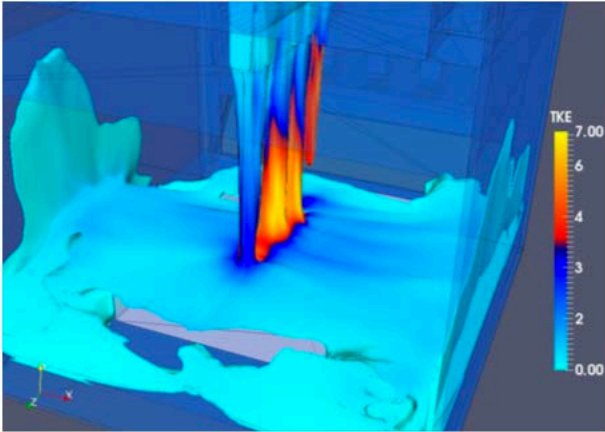
(a)



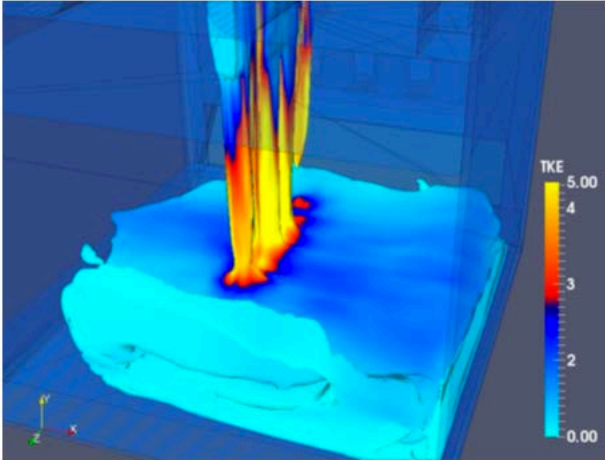
(b)

Figure 3-29. TKE in 4° Backward and Sideways Cases

Isocontours of stoichiometric mixture fraction colored by TKE for the 4° (a) backwards and (b) sideways cases.



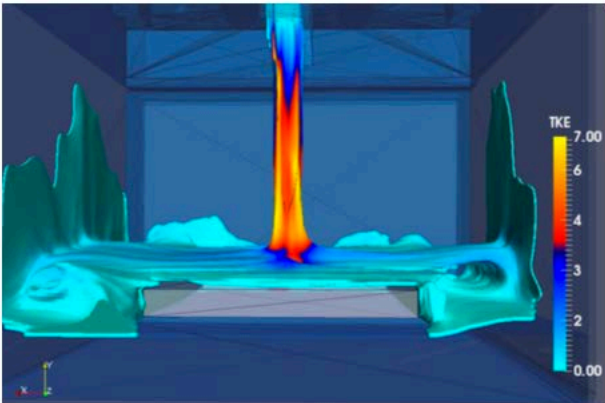
(a)



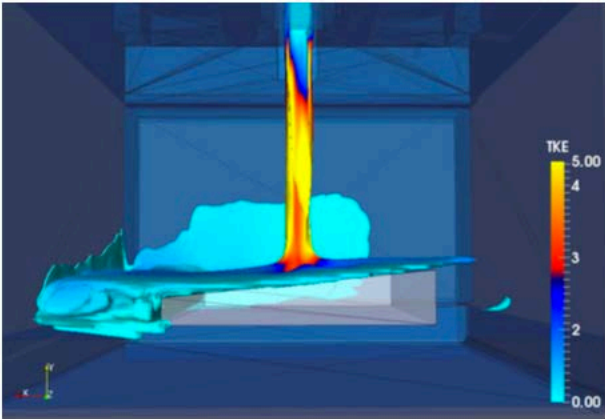
(b)

Figure 3-30. TKE and Vortex Formation in 4° Backward and Sideways Cases

View from rear of boiler detailing vortex formation in the 4° (a) backwards and (b) sideways cases.



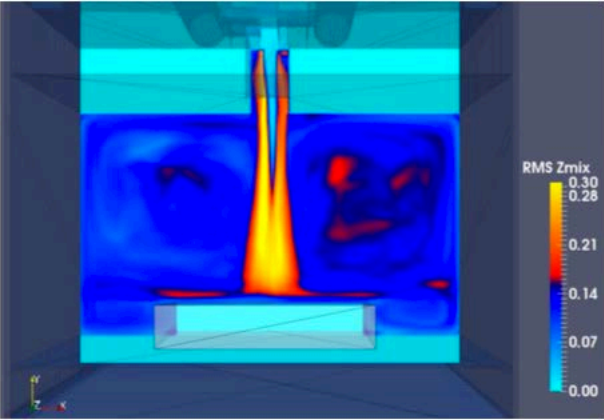
(a)



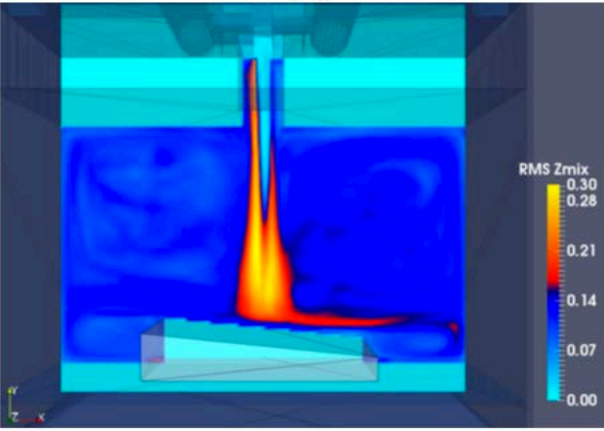
(b)

Figure 3-31. RMS Mixture Fraction in 4° Backward and Sideways Cases (Front)

X-axis slices showing RMS mixture fraction in the 4° (a) backwards and (b) sideways cases.



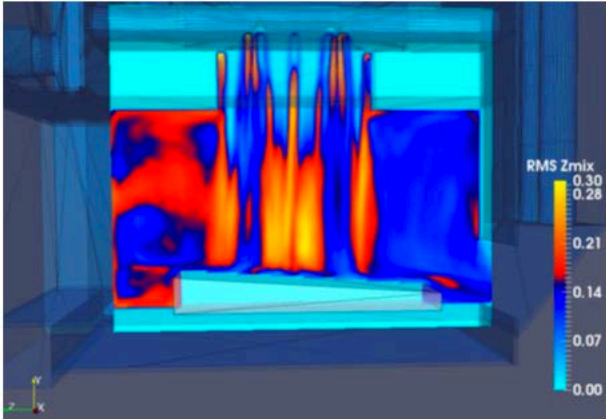
(a)



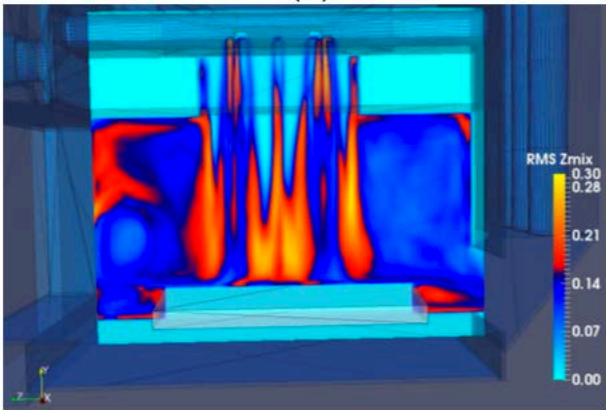
(b)

Figure 3-32. RMS Mixture Fraction in 4° Backward and Sideways Cases (Side)

Z-axis slices showing RMS mixture fraction in the 4° (a) backwards and (b) sideways cases.



(a)



(b)

Figure 3-33. PDF Comparisons for Baseline and Empty Chamber Cases

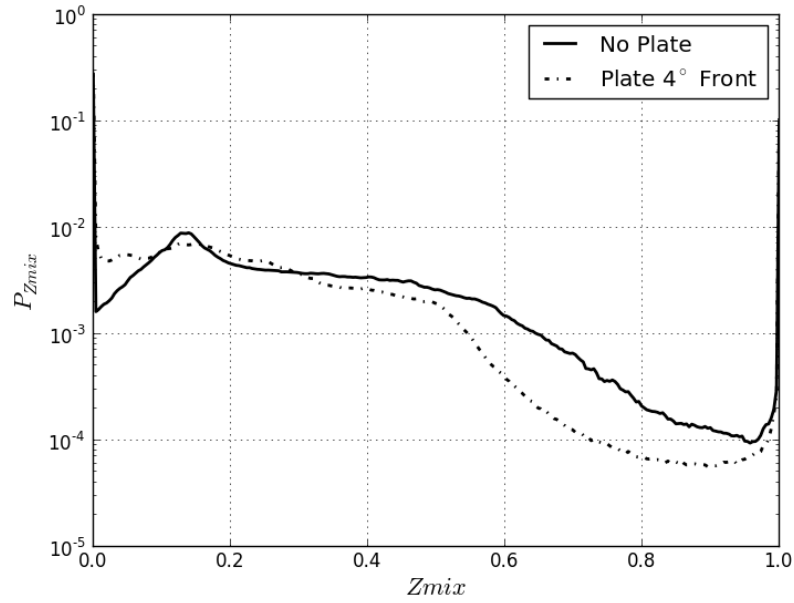


Figure 3-344. PDF Comparisons for Cases with Varying Angles of Inclination

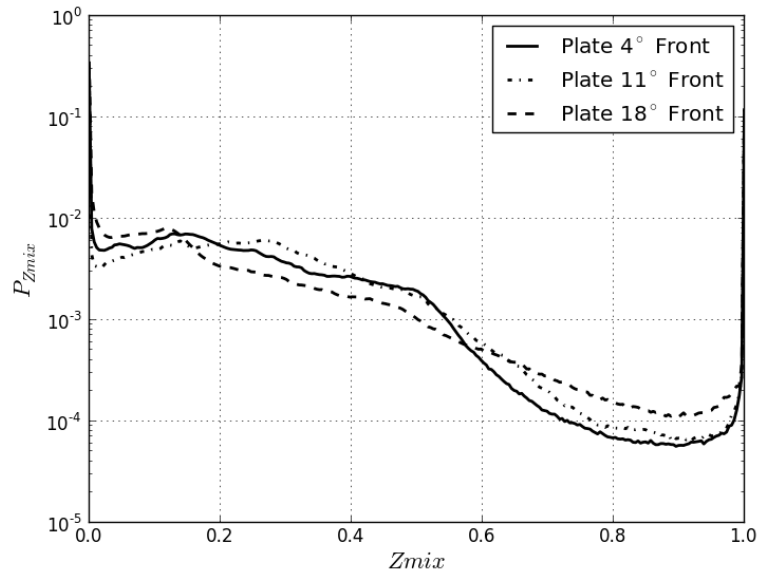
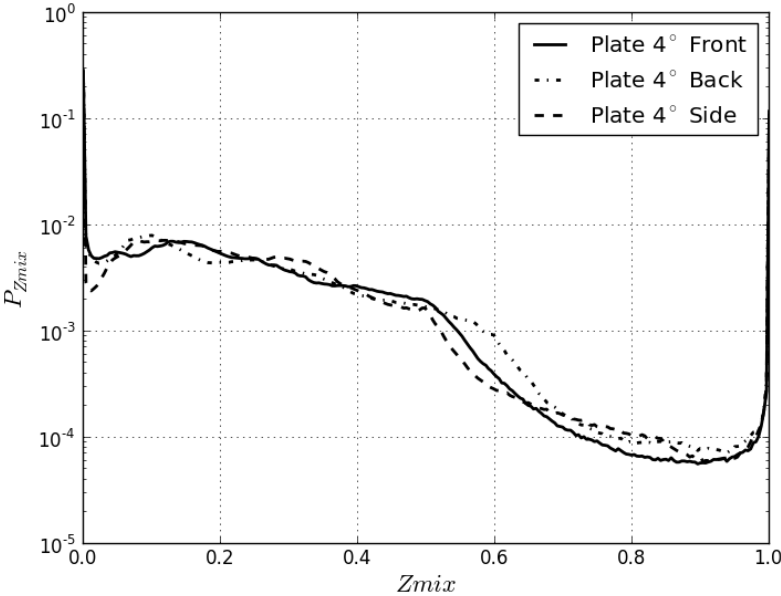


Figure 3-355. PDF Comparisons for Cases with Varying Directions



4 Fuel Sensitivity

4.1 Introduction

The advantage of using biomass over fossil fuel has been widely discussed for power generation and heating [49-51]. Many developing nations rely exclusively on biomass for energy production, as well as rural areas in northern regions of the United States where wood-fired heaters are an economically attractive alternative. However, one of the prevailing challenges using these systems is emissions. For the northeastern US, emissions from wood-fired heaters are one of the leading sources of reduced air quality. To provide stricter guidelines on the certification of these systems, the Environmental Protection Agency has recently defined specific new regulations for wood burning appliances including wood stoves, masonry heaters, pellet-burning stoves, and hydronic heaters [8]. Many studies focus on the characterization of emissions from specific biomass appliances, stoves, boilers, and large scale (>1 MW) power plants [52, 53]. Reduction in harmful pollutants resulting from the combustion of biomass materials is the primary goal of many government agencies and research developments.

The effect that various fuels have on these appliances has been briefly explored by comparing fuel types, sizes, delivery methods, and appliance operating factors [27, 53, 54]. Bignal *et al.* 2008 found that lower moisture content fuels facilitate the reduction of particulate matter (PM) and polycyclic aromatic hydrocarbon (PAH) emissions. Additionally, operation at full load and avoidance of smoldering fuel benefits in reduced emissions [55]. Petterson *et al.* 2011 found that for Swedish stoves air starved combustion with high heat output resulted in higher levels of CO due to the lack of oxidation. It was noted that overloading the stove can result in excessive heat output and oxygen starve combustion conditions due to low air to fuel ratios [56]. Roy *et al.* 2012 compares the operation of hay and grass briquettes in a domestic wood stove showing no significant variation in performance (both emissions and efficiency) for the alternative fuel types [24]. This report will similarly explore the variation in fuel type, size and moisture during typical operation of the Econoburn boiler. It will use the analysis developed in Task 13 to provide accurate estimates of H_2O and CO_2 emissions by additionally defining the elemental composition of the fuel as it changes with time.

The formulation developed uses measurements commonly made in the biomass industry, without direct knowledge of exact fuel type or fuel moisture content. Exhaust gas concentrations (O_2 , CO , and NO) and mass flow (fuel and air) measurements are used in an atom balance, assuming a 2:1 ratio of hydrogen to oxygen atoms in the fuel. Validation of the analysis has been demonstrated through non-intrusive tunable diode laser absorption spectroscopy measurements of CO_2 and H_2O in the flue. The results from the TDLAS measurements are based on first-principles quantum spectroscopy theory, where single molecular

absorption transitions are monitored to extract information regarding concentrations and temperatures of the absorbing gas species.

The rest of this study is organized as follows. Section 5.2 will discuss the experimental setup used in the analysis. Section 5.3 will summarize the analysis used to calculate the exhaust species and non-homogeneous elemental fuel composition. Section 5.4 will discuss the results of different fuels tested. Finally, section 5.5 will discuss the major conclusions.

4.2 Experimental

4.2.1 Hydronic Heater Experimental Setup

The test facility previously discussed in Richter et al. 2016 [40] and section 2.2 is used in this study where an Econoburn EBW-200 wood-fired hydronic heater is instrumented.

Figure 4-1 shows the differentiated mass loss rate with time for the BIOBLOCKS[®] (black line), cherry (red line), and pine (green line). Blower air flow rates are measured using a Bosch HFM-7 mass airflow meter operating under hot film anemometry methods. Direct calibration of the Bosch meter was made with an ASME standard venturi flowmeter. These measurements are used in the emission analysis discussed in section 4.3.

The fuel explored in this study is comprised of three variations. The first are BIOBLOCKS[®]. Manufactured by Summit Wood Industries, the blocks are made from 100% hardwood chips (composed primarily of red oak) and contain an average 8.3% dry-basis by mass water moisture. The exact moisture content of the blocks is measured in accordance with ISO standard 3130. Second, locally sourced kiln dried cherry cord wood with approximately 15.1% dry-basis by mass water moisture is used as a typical alternative fuel commonly used in rural domestic appliances. Third, 2x4 pine lumber cut into 6 inch long blocks and kiln dried to approximately 13.75% dry-basis by mass water moisture were also compared. A Testo 606-1 moisture meter was used to measure moisture content in the cherry and pine by averaging measurements of both end and center cut locations on a random sample of 20 pieces for each cherry and pine fuel.

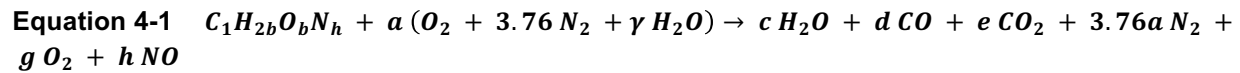
A full load boiler run typically requires 32 blocks ($\approx 62\text{ lbs}, 28\text{ kg}$). Accounting for variations in fuel density and limitations on the size of the load, 42lbs of cherry and 35lbs of pine were the maximum load capacities for the hanging basket.

4.2.1.1 Measurements of CO, NO, and O₂

Emissions measurements are recorded using a Testo 330-2 LL gas analysis meter. The analyzer is capable of taking experimental measurements of the O₂, CO, NO, pressure, and temperature from the flue gas stream. To correct measurements for water condensation in the sampling line, the correction procedure of Richter et al. [2] is used, requiring a separate measurement of O₂ using a Bosch LSU 4.9 ZrO₂ wide-band oxygen/lambda sensor. Ambient moisture content and temperature are measured in real time with an Omega HX92B series humidity sensor and K-type thermocouple. Figure 4-2 shows measured O₂ for each fuel type with very similar trends and magnitudes.

4.3 Emissions Analysis

A variable fuel formulation is developed in section 5.2.7 to determine the flue gas composition given the direct measurements of fuel and air flow rate, CO, NO, and O₂. In this approach, the wood fuel is assumed to have a variable composition, with the defining characteristic that the hydrogen and oxygen are released at a constant 2:1 ratio [57]. To include fuel nitrogen and reduce unknowns in the analysis, NO emissions are assumed to be derived entirely from the fuel, consistent with earlier studies [53, 58-60]. The overall one-step reaction for combustion is assumed to have the following form,



The unknown wood fuel composition is described as $C_1H_{2b}O_bN_h$ with the moisture content of the fuel included as part of the composition. The moisture in humid air is calculated from ambient humidity and temperature measurements, leaving three unknowns (b , h , and a). The right hand side of the reaction species coefficients c , d , e , g , and the total moles, N_{tot} , leave a total of eight unknowns. Three constraints are provided by measured values of CO, NO, and O₂ expressed as $X_i = n_i/N_{tot}$. Three more constraints come from atomic balances for C, H, and O (N is dependent on the NO measurement) along with the condition that the mole fractions sum to unity. Closure of the system of equations is obtained from measurements of fuel mass loss and air flow rate. In total, eight equations are solved as a system of equations for each sample measurement using Gaussian elimination. The resulting analysis provides real time C, H, O, and N atomic ratios for the non-homogeneously decomposing fuel, and emissions mole fraction of species (CO₂, H₂O, CO, NO, O₂, and N₂) in the flue exhaust.

4.4 Results

A comparison of CO measurements versus normalized time is shown in Figure 4-3a. Given the similarity in fuel composition, large deviations in emissions are not expected. The trends shown by each fuel type exhibit the typical double peak. Red oak gives an approximately 18% increase in peak CO during the first peak over that of the cherry and pine, this is likely attributed to the approximately 30% increase in peak burn rate over the cherry and pine fuels, leading to higher fuel to air ratios.

The NO is interesting in that the vast majority of NO is derived from the nitrogen contained in the fuel. Figure 4-3b shows a comparison of the NO vs normalized time where cherry and red oak are shown to be very similar in magnitude, differing only marginally (approximately 20% only during peak burn) and meeting back with the red oak levels during the early and late stages. The pine interestingly shows a rather significant decrease in NO during the majority of the burn with a maximum difference of approximately 80%. This is likely due to the low nitrogen content of the fuel (strengthened by the increase in nitrogen rich bark contained in cord wood and compressed mixtures of hard wood with the BIOBLOCKS[®]).

Figure 4-4a and Figure 4-4b show a comparison of the three fuels' CO_2 and H_2O versus normalized time. The early release of H_2O can be seen in each of the three fuel types with very similar ranges of values for both CO_2 and H_2O . The overall H_2O emissions are comparable for each of the fuel loads due to the reduction in initial fuel mass combined with the increase in moisture content for both the pine and cherry fuels. As a basic check the actual H/O ratio was calculated without a specific assumed value based on the knowledge of the measured CO_2 and H_2O in the flue exhaust. Figure 4-5 shows the measured H/O ratio for the portion of a run excluding the charcoal oxidation stage (during this stage the H and O approach zero and the values become meaningless). It can be seen that the three different fuel types, BIOBLOCKS[®] (red oak), cherry, and pine produce a relatively constant H:O ratio at the approximate value of 2:1.

4.4.2 Time History: Elemental Fuel Composition

Figure 4-6(a)-(c) shows the ratios H/C , O/C , and N/C as a function of normalized time. As the majority of unbound fuel moisture is driven from the fuel, the initial increase in effective H and O atomic ratios for each of the fuels can be seen. Virgin fuel pyrolysis and combustion then takes over with a linear decrease in H and O with time until the fuel H has been oxidized. Finally, the full consumption of H and O leads to the charcoal oxidation stage, where the remaining H_2O is delivered from the humidity in the incoming air. In Figure 4-6(c) the nitrogen slowly increases as the remaining charcoal is further depleted. Minor differences in fuel H and O can be seen where the fuel with the higher moisture content (cherry and pine)

demonstrate increased hydrogen and oxygen, however overall agreement is shown in magnitude and trend for the H and O ratios. Nitrogen ratios show a considerable decrease for the case of pine 2x4s, corresponding with a reduction in NO production throughout the burn.

4.4.3 Time History: Heating Value

The time dependent fuel composition can be used to estimate the higher heating value of the fuel [27].

$$\text{Equation 4-2} \quad HHV = (33.5[CC] + 142.3[HC] - 15.4[OC] - 14.5[NC]) \times 10^{-2}$$

Equation 4-2 represents the HHV [MJ/kg] for biomass fuel given a specified elemental mass percentage for carbon (CC), hydrogen (HC), oxygen (OC), and nitrogen (NC) [27]. Figure 4-7 shows the HHV for the variable fuel composition of red oak (black), cherry (red), and pine (green) with a comparison to a reference value for coal (grey). As the virgin fuel dries early in time, it undergoes pyrolysis and forms charcoal where the HHV approaches that of coal (32.3 MJ/kg). Similar trends are observed for each of the three fuel types. The cherry and pine show higher ratios of H and O compared to red oak due to the higher moisture content of the fuel subsequently decreasing the HHV values compared to the red oak.

4.4.4 Time History: Thermal Efficiency

Thermal efficiency is often expressed in terms of total (integrated) heat delivered (ΔQ_{del}) divided by the total caloric chemical energy available (ΔQ_{comb}) of the fuel used, *i.e.*, $\bar{\eta}_{th} = \Delta Q_{del} / \Delta Q_{comb}$, where a single efficiency is reported per fuel charge [8]. While this definition provides an estimate of the average efficiency of an appliance, it is limited since important transient information is lost. Using the results from Figure 4-7, η_{th} can now be computed as: $\eta_{th} = (\dot{Q}_{del} + \dot{Q}_{stor}) / \dot{Q}_{comb}$, where $\dot{Q}_{comb} = (|\dot{m}_f| HHV)$ is the heat produced from combustion. The term $\dot{Q}_{stor} = C_b m_b (dT_b/dt)$ represents the instantaneous heat transferred to the boiler and inferred from the measured mean water and wall temperatures. The term $\dot{Q}_{del} = C_w \dot{m}_w (T_{w,out} - T_{w,in})$ is the delivered heat to the thermal load (heat exchanger) which is experimentally determined from measurements of the water temperature and flow rate going in ($T_{w,in}$) and out ($T_{w,out}$) of the boiler. Figure 4-8 shows a comparison of the instantaneous efficiency as a function of normalized time for each of the three fuels tested. Similar trends are observed for each of the fuel types with a higher peak efficiency found for the pine followed closely by the red oak and the cherry. Integrated thermal efficiencies ($\bar{\eta}_{th} = (\Delta Q_{del} + \Delta Q_{stor}) / \Delta Q_{comb}$) calculated for each fuel (red oak, cherry, and pine) are comparable with approximately $\bar{\eta}_{th_{redoak}} = 53\%$, $\bar{\eta}_{th_{cherry}} = 54\%$, and $\bar{\eta}_{th_{pine}} = 58\%$ respectively.

4.4.5 Total Emissions

By integrating the total mass of CO, NO, and CO₂ emissions and normalizing by the total mass of the exhaust an overall emissions value is obtained to compare against each fuel type. Table 4.1 shows the total [%wt] of CO, NO, and CO₂ for red oak, cherry, and pine. The values indicate that red oak produced the most emissions with a 19% increase in CO over the cherry and pine. Red oak NO shows a 44% increase over cherry and pine where the pine is significantly reduced, due to lower nitrogen content in the fuel.

4.5 Conclusion

The analysis presented below in section 5.2.7 provides a clear description of the various stages in fuel decomposition for batch-run wood burning systems. The changing elemental composition of the fuel is calculated without direct knowledge of the exact wood type or unbound moisture content. This task tests three different fuel types (Red Oak, Cherry, and Pine) in varied loads and moisture contents (8.3%, 15.1%, 13.75% respectively). Results demonstrate a close similarity in overall emissions trend.

In particular, production of *NO* in the pine showed significant reduction over the other fuels due to the lower nitrogen content in the fuel. Total pine *CO* emissions are in-line with the cherry cord wood and only moderately lower than the red oak with a 16% difference. Ultimately these results agree with previous studies and demonstrate various wood species produce little variation in emissions as well as efficiency. Reduction in *NO* may be most effective through the selection of low nitrogen containing fuels. Effects due to fuel shape and size are inconclusive, however lower emissions seen in the pine may indicate that loading configuration may play a role.

Instantaneous real time efficiency shows a similar trend and magnitude for each of the fuels adding to the conclusion that minor variations in wood species shape and size do not significantly effect performance. The effect of moisture content on the higher heating value and efficiency show minor reductions compared to red oak at 8.3% during the peak burn rate. However other studies [55] claim that particulate and polycyclic aromatic hydrocarbon emissions is increased with higher moisture contained fuels.

It is interesting to note that Kinsey et al. 2012, tests a 38 kW updraft hydronic heater with both red oak and pine with similar moisture levels (27-38% and 36% respectively) [61]. Their results for the same appliance running different fuels for pine show an increase in thermal efficiency over red oak similar to the increase seen in this study. Additionally, a reduction in nitrogen based emissions (*N₂O*) is also observed for pine.

Table 4.1. Total Emissions for Runs with Red Oak, Cherry and Pine [%wt]

	red oak	cherry	pine
<i>CO</i>	0.28	0.23	0.24
<i>NO</i>	0.0041	0.0035	0.0022
<i>CO₂</i>	5.0	4.3	4.6

Figure 4-1. Burn Rate for Red Oak, Cherry and Pine

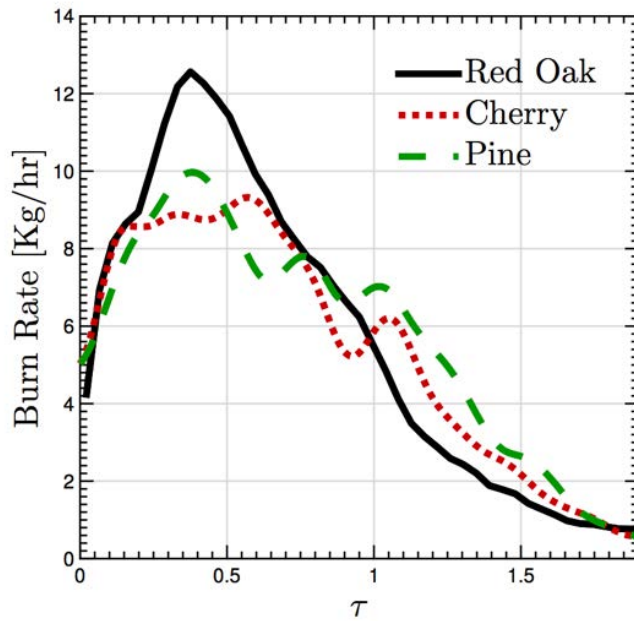


Figure 4-2. O₂ Mole Fraction

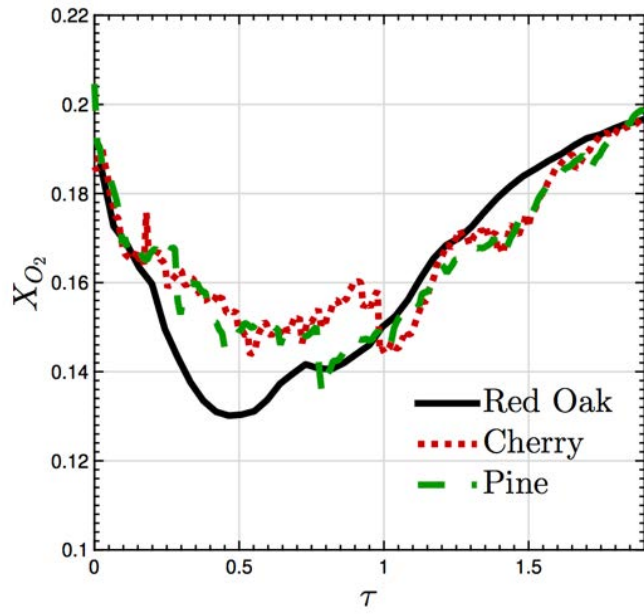
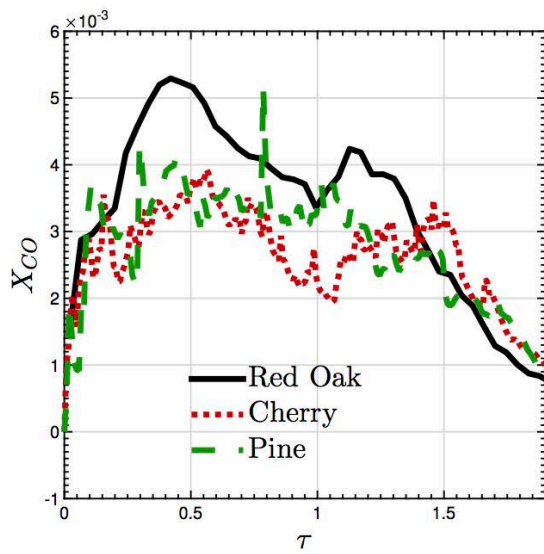
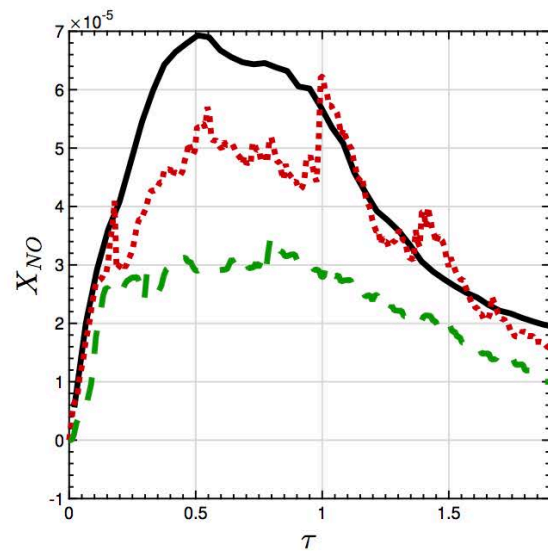


Figure 4-3. CO and NO Mole Fraction

Comparison of (a) CO mole fraction, (b) NO mole fraction vs. normalized time.



(a)



(b)

Figure 4-4. H₂O and CO₂ Mole Fraction

Comparison of (a) H₂O mole fraction, (b) CO₂ mole fraction vs. normalized time.

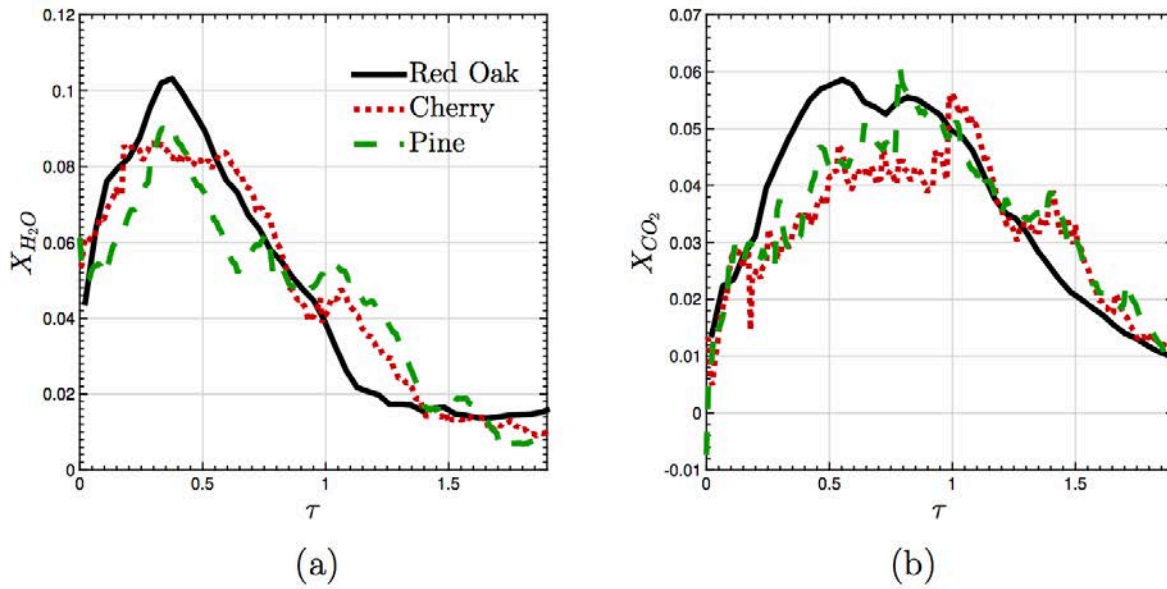


Figure 4-5. Calculated Hydrogen:Oxygen Ratio During Burn

Calculated hydrogen to oxygen ratio during a burn excluding the charcoal oxidation stage for BIOBLOCKS (red oak), cherry and pine fuels.

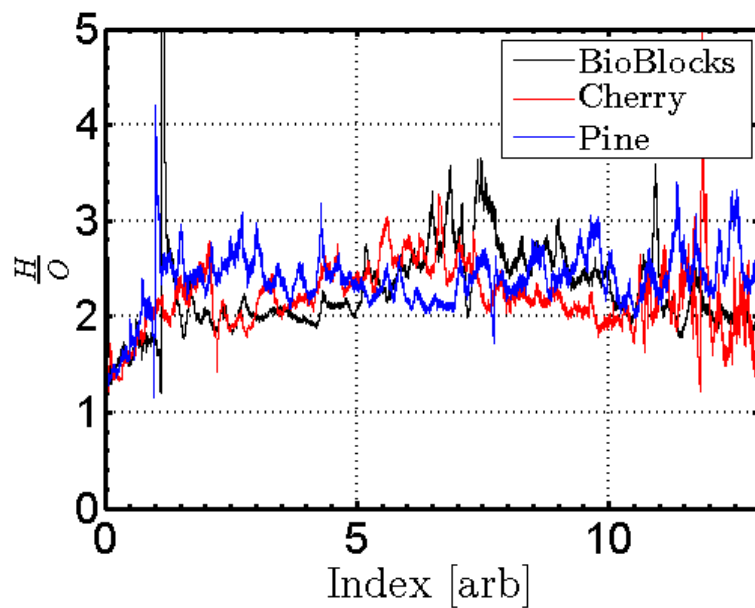


Figure 4-6. Comparison of Atomic Ratios

Comparison of (a) H/C , (b) O/C , and (c) N/C vs normalized time for red oak, cherry and pine.

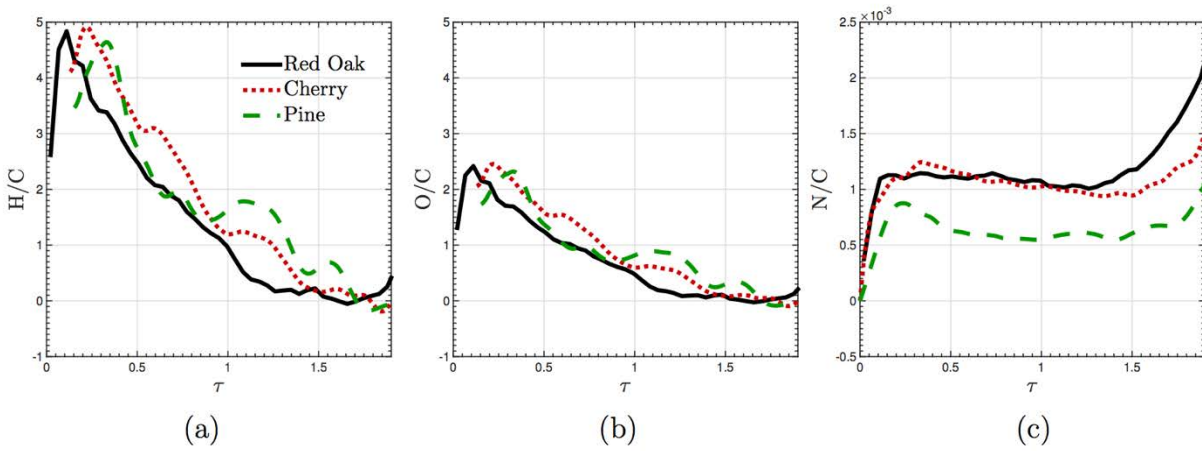


Figure 4-7. Comparison of Higher Heating Value

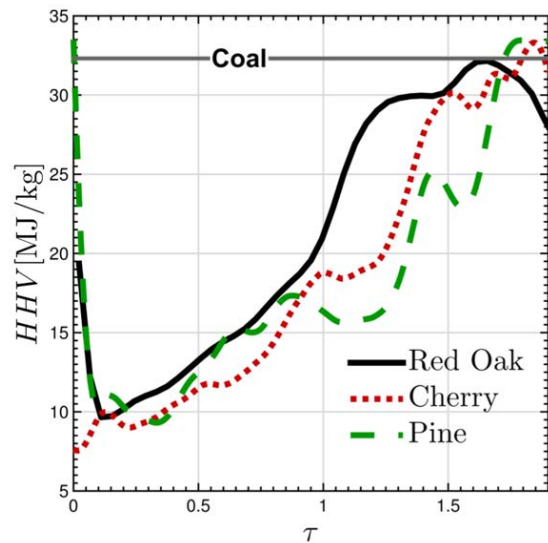
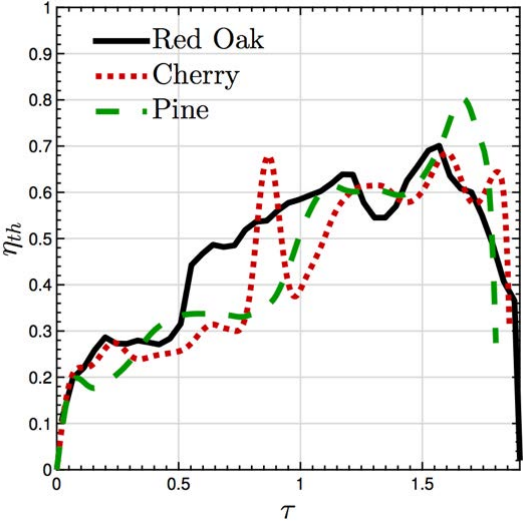


Figure 4-8. Comparison of Real Time Efficiency



5 Improving Emission Measurements

5.1 Water Vapor Corrections

5.1.1 Introduction

Combustion gas analysis and stack emissions measurements typically used in the automotive, aircraft, processing, and heating and air conditioning industries use a variety of sensor technologies including gas chromatography [62, 63], electrochemical fuel cells [40, 64], and infrared spectroscopic methods [63, 65-70].

Spectroscopic infrared based methods have been developed for non-intrusive in-situ measurements [69, 70]. One of the most widely used is Fourier Transform infrared spectroscopy (FTIR) which uses a wide spectral range compared to the range of wavelengths measured by a dispersive spectrometer, this provides a beneficial increase in the signal to noise ratio [63, 66, 70-73]. Tunable diode laser absorption spectroscopy is also commonly used for non-intrusive emissions measurements do to its ability to detect lower emissions concentrations and determine temperature, pressure, and velocity of the gas [67, 68]. Non-dispersive infrared (NDIR) methods have been used in on-board emissions monitors for automobiles and provide an accurate non-intrusive method for in-situ measurements [69]. Nakamura et al. 2002, also discusses the effect of H_2O interference with respect to spectral overlap and molecular interaction, presenting a correction strategy if the water concentration is additionally known. The use of these infrared based spectroscopic techniques in-situ would eliminate the need for a water vapor dilution correction, however individual development for portable in-situ measurements can be prohibitively expensive.

Many of these technologies that are not in-situ based, sample the gas by pumping an *in-situ* sample through a system of tubes to reach the sensor at a remote location (prominent analyzer manufacturers are: Testo, Wohler, Land, etc.). Since water vapor is inevitably present in combustion products, an inherent characteristic with the gas sampling strategy is that the mixture state changes as the sample is drawn towards the sensor. In particular, temperature and humidity changes can be significant, resulting in a very different gas mixture at the sensor interface compared with the *in-situ* location. Significant amounts of condensed water vapor (liquid) have been observed to collect over time in the filters, probe lines, and condensation reservoir. This causes an increase in the pressure drop, overloading the sample pump and resulting in reduced flow of the sampled gas. Common solutions to these problems are addressed through various industry led developments such as heated probe lines, fast sample draw rates, as well as sample conditioning through Peltier cooling chambers [74]. The latter provides a set of repeatable conditions standardized at a

temperature (273 K) and pressure (1013 mbar) [74] which allow for relative comparisons of combustion performance when operated under the prescribed dry conditions. This condition defines what will be referred to as a relative emissions measurement, since all values obtained are accurate relative to the dry state. In contrast, absolute emissions measurement define the molar concentrations at an unaltered *in-situ* state. Some analyzers alternatively, use the surrounding air temperature for sample conditioning. Unfortunately, in such units the gas temperature and humidity at the sensor can be ambiguous. These analyzers bring the sample gas mixture from a “wet” *in-situ* condition, as it exists at the original sample location, to a “dry” condition that has gone through an incomplete water condensation change due to cooling. Within this discussion, “dry” will refer to the state of the mixture at the sensor where an unknown but lesser quantity of water vapor is contained within the sample compared with the original high temperature wet mixture condition; or, *in-situ* state.

In this study a heated Bosch LSU 4.9 ZrO_2 wide-band oxygen sensor is used to measure *in-situ* oxygen concentrations. The heated aspect of the Bosch sensor is important to this study since it insures that there is no water vapor condensation at the sensor interface positioned *in-situ*. These types of sensors are used extensively in the automotive industry where precise knowledge of absolute oxygen concentrations are required for optimal engine performance [75]. The second sensor is within a remote gas sampling Testo 330-2 LL analyzer. These types of combustion gas analysis units are widely used in various industries to monitor exhaust gas composition for regulatory certification testing and combustion optimization studies. The sensor used in the Testo is an electrochemical/galvanic sensor based on the principle of ion selective potentiometry [74, 76]. Due to the sensors remote location within the hand-held analyzer a sample of test gas is pumped through a system of tubes, often several feet long, and multiple filters before reaching the sensor interface. This process cools the mixture and partially condenses the water vapor from the sample gas, effectively changing the molar concentrations.

The motivation for this study is to develop a correction methodology to determine accurate absolute *in-situ* gas compositions from a remote gas sampling analyzer. Richter *et al.* 2016 [40] uses remote gas sampling measurements for comparison to combustion model species concentrations and indicates the need for a correction strategy to account for the lost humidity. Similar strategies may be known in closed industry circles, however, a lack of published detail on the subject further motivates this work. The rest of this paper is organized as follows. In Section 6.1.2 the experimental setup will be outlined providing details on the specific instrumentation used to develop the correction method. In Section 6.1.3 results will first demonstrate the effectiveness of the Bosch instrument to measure the absolute oxygen concentration versus the gas sampling analyzer measurements. A correction method will be presented that requires the use of

both oxygen sensors (Bosch and Testo) working in tandem to correct measured species concentrations from the remote analyzer. Finally, validation of the method will be demonstrated with a known concentration of CO. Section 6.1.4 will outline the conclusions of the study.

5.1.2 Experiments

An experimental set-up is designed (see Figure 5-1) wherein a test cell is constructed from commonly used PVC pipe fittings sealed at each end of an aluminum cylinder. The primary function of this test cell is to provide a contained environment where uniformity in temperature, humidity, and gas concentration can be assumed. Figure 5-1 shows the experimental schematic along with a photo of the actual assembly with main system components indicated. Premixed NIST traceable calibration gas at oxygen concentrations of 15%, 10%, 5%, and air (20.9%) are used in this study. Measurements of gas temperature (T) and relative humidity (ϕ) are taken along with oxygen concentrations (% by volume) using two sensors (Bosch and Testo). Data is simultaneously recorded using a National Instruments data acquisition board (NI USB-6008) with LabVIEW and Testo EasyHeat software at a frequency of 1 Hz. Temperature data is taken using a K type thermocouple located in the probe of the Testo analyzer. Relative humidity is measured using an Omega HX92B series humidity sensor within the test cell. A Bosch LSU 4.9 ZrO_2 wide-band oxygen/lambda sensor coupled with an ETAS CBS100.1-2E smart lambda cable to regulate the power supplied to the heated sensor is used *in-situ*. The gas sampling remote analyzer uses electrochemical/galvanic sensors within a Testo 330-2 LL analyzer.

A single run for each gas is started after powering on all sensors from a cold start and initializing the data acquisition systems. Upon sensor warm-up (approximately 30 seconds) the calibration gas valve is opened and calibration gas is supplied to the test cell. The remote analyzer samples the calibration gas at approximately 0.6 lpm while the gas is supplied to the test cell at a rate of 1.2 lpm allowing for a controlled system flushing and asymptoting of concentrations to a steady state (approximately 5-8 minutes). The test cell is oriented vertically with the exhaust outlet located at the bottom to take advantage of the buoyancy of the dry calibration gas over that of air, facilitating the initial test cell purge. After reaching a steady concentration, data is collected at dry conditions for at least one minute, after which water vapor is introduced into the calibration gas upstream of the test cell, through a contained sample of boiling water. Test cell humidity is monitored and a steady state humidity of approximately 95-100% RH is reached after 1-2 minutes. During the testing period, humidity, temperature, and the known dry gas concentrations define the test cell conditions and are simultaneously recorded. Temperature conditions within the test cell are inherently unsteady due to heat release from the ZrO_2 oxygen sensor as well as latent heat release associated with the condensing water vapor introduced into the test cell. Using psychrometric relationships, an

expected (calculated) oxygen concentration can be found based on the known test cell conditions with an associated uncertainty propagated from the measured experimental humidity and temperature. Pressure within the test cell is atmospheric, given the low flow velocity and open exhaust tube. Water vapor partial pressures are calculated from the relation found by Wagner and Pruss, 1993 [77]. After each run the humidity sensor requires a dry air purge due to moisture saturation during the experiment, this is done by flushing the system with dry air at a low flow rate for 24 hours to completely dry out the system prior to the next test.

5.1.3 Results

Figure 5-2 shows measured oxygen concentrations vs. time, comparing the Testo (orange dots), Bosch (blue dots), and calculated (black line) values as conditions within the test cell are varied, each with respective uncertainty bounds (indicated by shaded regions). Experimental uncertainty is calculated for the gas sensors, humidity sensor, and thermocouple. Factory reported instrument accuracies for each instrument is used for the shaded uncertainty regions seen in Figure 5-2 and Figure 5-3. Uncertainty bounds for the calculated oxygen and carbon monoxide (black line with shaded bounds) are obtained by calculating the concentrations using the upper and lower limits of the humidity, temperature, and specified concentration separately to find the propagated upper and lower uncertainty of the calculated/expected concentration. Zero molar uncertainty is assumed for the case of air.

The calculated results are based on the known molecular weight of dry gas (M_a), water vapor (M_w), gas temperature (T), and gas pressure (P, taken to be atmospheric) at the measured relative humidity (ϕ). These variables are used in the definition of humidity ratio $\omega = m_w/m_a = (M_w/M_a)\phi P_{sat}/(P - P_w)$ to determine a relationship between the mass of the gas and water vapor in the mixture. Multiplying the respective molecular weights results in a mole fraction ratio $\% \omega = (M_a/M_w)\omega = X_a/X_w$ where individual concentrations are calculated after imposing $X_a + X_w = 1$.

At early time, before moisture is added, all measurements agree since there is no water vapor to displace the oxygen. Moving forward in time, after the dry conditions have been sufficiently demonstrated, water vapor is introduced into the gas mixture as is evident by the increase in relative humidity and decrease in oxygen concentrations due to displacement. The Bosch O_2 sensor is seen to reliably agree with the calculated O_2 value within the experimental uncertainty. As the relative humidity approaches 100% the disagreement between the Testo and Bosch sensors becomes significant and deviates further as temperature increases. The Testo O_2 measurements (seen in Figure 5-2) plateau after a minor decrease in concentration, indicating a non-zero, finite amount of humidity influencing the sensor. If the humidity within the remote

unit were zero, no shift would be recorded and completely dry conditions could be assumed. Figure 5-2(a) demonstrates the effect measured in air where the gas sampling analyzer shows an approximate 7% error (@316K and 98%RH). Figure 5-2(b) measured in 15% O_2 with the rest N_2 where the gas sampling analyzer shows an approximate 8% error (@319K and 99%RH). Similarly, Figure 5-2(c) shows the effect measured in 10% O_2 with the rest N_2 where the gas sampling analyzer shows an approximate 11% error (@320K and 98%RH). It is important to realize that these errors will increase even further in combustion gases where the temperatures are much higher. For instance, additional measurements taken for wood-fired appliances (not shown) indicate errors as high as 25%.

A correction methodology is developed from comparing the definition of species mole fraction for both wet and dry samples. The correction for any remotely measured gas species reduces to $X_{i,wet} = X_{i,dry} (X_{O_2,wet}) / (X_{O_2,dry})$ where $X_{O_2,wet}$ is measured by the Bosch sensor, and $X_{O_2,dry}$ is measured by the Testo sensor. To validate the correction method, Figure 5-3 shows a specialized case where the conditions within the test cell are brought to ~344K and high humidity. It should be noted a small jump in oxygen concentration can be seen as water vapor is added to the test cell, this is due to the inclusion of trapped air in the water vapor line. The effects of which become negligible within 5 minutes. These conditions clearly reveal the deviation in CO measured with the gas sampling analyzer to that of the corrected value based on the method previously discussed. Initially a steady state is reached where the calibrated CO sensor measures the dry molar concentration in the calibration gas. As the calibration gas is mixed with water vapor to increase the relative humidity, the temperature within the chamber is further augmented by heating the cell inlet and walls with a heat gun, to more clearly emphasize the measured disparity. The correction method allows the measured CO value (from the Testo) to remain within the regions of uncertainty thereby demonstrating its effectiveness in measuring the absolute *in-situ* species concentration under wet conditions.

5.1.4 Conclusion

A method for correcting dry gas concentration measurements due to water vapor condensation has been developed. This method requires the use of a heated ZrO_2 wide-band oxygen/lambda sensor to calculate the *in-situ* concentrations. Calibration testing of the two sensors is done to demonstrate the observed water vapor dilution effect and to assess the accuracy of the Bosch and Testo sensor under varied humidity and temperature ranges. Results indicate both the Bosch and Testo instruments operate accurately within the bounds of uncertainty under dry conditions and deviate with increasing humidity. Validation of the correction method is achieved by comparison of the corrected CO measurements with calculated values and good overall agreement is seen.

5.2 Emission Measurements using Laser Absorption Spectroscopy

5.2.5 Introduction

The environmental advantage of using biomass over fossil fuel has been widely discussed for power generation and heating [49-51]. Many developing nations rely exclusively on biomass for energy production, as well as rural areas in northern regions of the United States where wood-fired heaters are an economically attractive alternative. One of the prevailing challenges using these systems, however, is emissions. For the northeastern US, emissions from wood-fired heaters are one of the leading sources of reduced air quality. To provide stricter guidelines on the certification of these systems, the Environmental Protection Agency has recently defined specific new regulations for wood burning appliances, including wood stoves, masonry heaters, pellet-burning stoves, and hydronic heaters [8]. Many studies focus on the characterization of emissions from specific biomass appliances, stoves, boilers, and large scale (>1 MW) power plants [52, 53]. Reduction in harmful pollutants resulting from the combustion of cellulosic based biomass materials is the primary goal of many government agencies and research developments.

Certification of these devices require an accurate representation of emissions species concentrations. Measurements of both CO_2 and H_2O are typically required for emissions-based efficiency calculations [12]. For many independent testing facilities and manufacturers, direct measurement of gas species can be cost prohibitive. Often, low cost gas sampling analyzers (Testo, Land, Wohler, etc.) are used to measure select harmful pollutants (CO and NO) directly, along with the oxygen sensors to estimate CO_2 concentrations based on an assumed constant fuel composition. In conjunction to the CO_2 estimation, H_2O is often approximated using a global reaction mechanism [7, 8, 10, 12, 40, 42, 54, 78-81]. It is therefore subject to interpretation and inaccurate for some conditions. While non-homogeneous biomass decomposition has been extensively studied [27, 54, 59, 80, 82, 83], its application in the biomass community has been relatively unexplored.

The facility and analysis for a constant fuel formulation (CFF) was developed in reference [40]. This study builds on reference [40] by presenting a novel variable fuel formulation to accurately calculate the non-homogeneous decomposition of the solid fuel and major exhaust gas species (CO_2 and H_2O) using measurements commonly made in the biomass industry. Exhaust gas concentrations (O_2 , CO , and NO) and mass flow (fuel and air) measurements are used in an atom balance, assuming a 2:1 ratio of hydrogen to oxygen atoms in the fuel. Validation of the analysis is demonstrated through non-intrusive tunable diode laser absorption spectroscopy measurements of CO_2 and H_2O in the flue. The results from the TDLAS measurements are based on first-principles quantum spectroscopy theory, where single molecular

absorption transitions are monitored to extract information regarding concentrations and temperatures of the absorbing gas species.

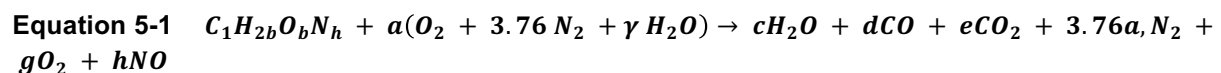
The rest of this study will be organized as follows. Section 6.2.6 will discuss the experimental setup used in the analysis. Section 6.2.7 will detail the analysis used to calculate the exhaust species and non-homogeneous elemental fuel composition. Section 6.2.7.1 will discuss the results of the CO_2 and H_2O validation with TDLAS. Finally, section 6.2.9 will discuss the major conclusions and outline the novelty of this work.

5.2.6 Experimental Facility

The test facility previously discussed in [40] and section 2.2 is used in this study where an Econoburn EBW-200 wood-fired hydronic heater is instrumented. The setup consists of primary and secondary water circulation loops, and a heat exchanger to expel heat. Figure 5-4a shows the boiler setup, where the load loop contains a 300,000 BTU/hr (87.9 kW) counterflow heat exchanger to transfer heat from the boiler to a cold thermal sink. Instantaneous fuel mass burn rate is measured according to the method presented in Richter et al. 2016 [40] (see Figure 5-4b). Figure 5-5a demonstrates the raw mass data and Figure 5-5b shows the differentiated mass loss rate with time. Figure 5-6 shows mean measured O_2 , CO , and NO with data spread from three runs.

5.2.7 Emissions Analysis

A variable fuel formulation is developed to determine the flue gas composition given the direct measurements of fuel and air flow rate, CO , NO , and O_2 . In this approach, the wood fuel is assumed to have a variable composition, with the defining characteristic that the hydrogen and oxygen is released at a constant 2:1 ratio [57]. To include fuel nitrogen and reduce unknowns in the analysis, NO emissions are assumed to be derived entirely from the fuel, consistent with earlier studies [53, 58-60]. This assumption is supported by the recent results of Rabaçal et al. 2013 [53] where measured NO emissions are linearly correlated with fuel nitrogen. The overall one-step reaction for combustion is assumed to have the following form,



On the left hand side of the reaction, the unknown wood fuel composition is described as $C_1H_{2b}O_bN_h$ with the moisture content of the fuel included as part of the composition. The moisture coefficient γ describes

the ratio of mole fractions between oxygen and water in humid air, and is calculated from ambient humidity and temperature measurements, leaving three unknowns (b , h , and a). On the right-hand side of the reaction, the remaining species coefficients c , d , e , g , and the total moles, N_{tot} , leave a total of eight unknowns. Three constraints are provided by measured values of CO , NO , and O_2 expressed as $X_{CO} = d/N_{tot}$, $X_{NO} = h/N_{tot}$ and $X_{O_2} = g/N_{tot}$, respectively. Three more constraints come from atomic balances for C , H , and O (N is dependent on the NO measurement) along with the condition that the mole fractions sum to unity. Closure of the system of equations is obtained from measurements of fuel mass loss and air flow rates,

$$\text{Equation 5-2} \quad \frac{\dot{m}_f}{\dot{m}_a} = \frac{(MW_C + 2b MW_H + b MW_O + h MW_N)}{a(MW_{O_2} + 3.76 MW_{N_2} + \gamma MW_{H_2O})}$$

In total eight equations are solved and are expressed in matrix form as,

$$\text{Equation 5-3} \quad \begin{bmatrix} 0 & 0 & 0 & 0 & -1 & 0 & 0 & X_{CO} \\ 0 & 0 & 0 & 0 & 0 & 0 & -1 & X_{O_2} \\ 0 & -1 & 0 & 0 & 0 & 0 & 0 & X_{NO} \\ 0 & 1 & 3.76 & 1 & 1 & 1 & 1 & -1 \\ 0 & 0 & 0 & 0 & 1 & 1 & 0 & 0 \\ 2 & 0 & 2\gamma & -2 & 0 & 0 & 0 & 0 \\ 1 & -1 & (2 + \gamma) & -1 & -1 & -2 & -2 & 0 \\ \Omega & -MW_N & \Psi & 0 & 0 & 0 & 0 & 0 \end{bmatrix} \begin{bmatrix} b \\ h \\ a \\ c \\ d \\ e \\ g \\ N_{tot} \end{bmatrix} = \begin{bmatrix} 0 \\ 0 \\ 0 \\ 0 \\ 1 \\ 0 \\ 0 \\ MW_C \end{bmatrix}$$

where the quantities Ψ and Ω are defined as,

$$\text{Equation 5-4} \quad \Psi = \frac{\dot{m}_f}{\dot{m}_a} (MW_{O_2} + 3.76 MW_{N_2} + \gamma MW_{H_2O})$$

$$\text{Equation 5-5} \quad \Omega = (-2 MW_H - MW_O)$$

The system of equations is solved for each sample measurement using Gaussian elimination. The resulting analysis provides real time C , H , O , and N atomic ratios for the non-homogeneously decomposing fuel, and emissions mole fraction of species (CO_2 , H_2O , CO , NO , O_2 , and N_2) in the flue exhaust.

5.2.7.1 Experimental Validation: TDLAS Measurements of CO_2 and H_2O

Tunable diode laser absorption spectroscopy is used to directly measure the concentrations of CO_2 and H_2O of the exhaust gas in the flue in order to validate the new analysis. Extremely accurate mole fractions are obtained because the signal is a result of individual molecular absorption transitions, and the lineshape of the feature is well defined. A schematic of the diagnostic setup is shown in Figure 5-7.

The infrared laser diode is a distributed feedback quantum cascade laser constructed by Nanoplus specifically for emission at $2.715 \mu\text{m}$, packaged in a TO-5 heat sink housing with a collimation lens on the front. A Lightwave ILX LDC-3721 laser diode driver and thermoelectric cooler (LDD-TEC) is used to control the laser. The diode emits at $2.715 \mu\text{m}$ when the temperature is 37°C and the current is 155 mA (output power of 5.4 mW). To scan through a wavenumber range, the output current is modulated using a Tektronix AFG3051C arbitrary function generator with a frequency of 20 Hz. The function generator output is connected to the LDD-TEC input, and modulates the output current of the LDD to the laser. The small, controlled current modulation scans the laser from a low to high wavelength. The wavenumber scan range used for these measurements is approximately 3683.5 cm^{-1} to 3686.5 cm^{-1} . This range is used to capture both CO_2 and H_2O peaks in a single ramp.

Due to incomplete combustion, soot is also present in the exhaust gases, and can accumulate on the CaF_2 windows. To mitigate this effect, the windows are bathed with N_2 throughout the duration of a run. To eliminate absorption in the laboratory air, the laser pitch and laser catch sides are housed in acrylic boxes that are purged with N_2 .

Every ten seconds, the system collects four ramps with 10,000 data points (2,500 points per ramp). Running at a frequency of 20 Hz, four ramps are scanned over a period of 0.2 seconds, which is faster than the transients occurring in the boiler. Three detectors are connected to a data acquisition system (National Instruments). The first detector captures the signal through a solid germanium etalon with a free spectral range of 1.75 GHz, which is used to convert between arbitrary time and wavenumber. The second detector captures the absorption signal through the flue gas. The third detector captures a baseline ramp, which is N_2 purged over its entire line-of-sight such that there is no absorption. This line-of-sight passes through the baseline tee, which extends from window to window in the flue, and is pumped with N_2 throughout the run.

The data from the three detectors is used to convert the raw signal (arbitrary voltage versus arbitrary time) into the final transmission versus wavenumber signal, which is compared to simulations using a line-by-line code. The path length through the flue gas is known precisely, and the temperature of the gas is known from a thermocouple located just upstream of the measurement. Simulations are performed for various combinations of CO_2 and H_2O mole fractions at the given temperature, and a Chi-square error surface is constructed from which the minimum gives the best-fit to the boiler data. The error surface monotonically decreases in all directions, such that the minimum found from the simulations is assumed to be a global minimum. The error surface, and corresponding raw data and best-fit simulation data can be seen in Figure 5-8.

5.2.8 Results

A comparison of emissions estimates of CO_2 , assuming either the VFF or CFF against TDLAS measurements are shown in Figure 5-9. The data bars represent variation in the measurements over three runs. Comparison of the VFF against TDLAS measurements agree well with a mean error of approximately 3%. The CFF formulation however, under predicts by a mean error of approximately 20%. These differences are due to the preferential release of H_2O early in time which changes the effective composition of C, H, O, and N in the wood. The VFF accounts for these changes, where the CFF inherently does not.

The early release of H_2O can be seen in Figure 5-10 where a comparison of the calculated VFF and CFF against TDLAS measurements are presented. Excellent agreement is observed between the TDLAS measurements and the VFF with an approximate mean error of 3%. However due to the uniform fuel assumption of the CFF, H_2O is underpredicted at early times and overpredicted during the charcoal oxidation stage, resulting in a mean error of approximately 23%. This direct comparison to TDLAS demonstrates the clearly erroneous assumption of a constant fuel approach, where it is shown that the VFF provides a more accurate physical description.

5.2.8.1 Time History: Elemental Fuel Composition

The BIOBLOCK[®] fuel used in this study is composed of 100% compressed hardwood and is assumed to be primarily of the red oak variety. Red Oak has an approximate composition of $C_1H_{1.7}O_{0.72}N_{0.001}$ [26], and with an 8.3% dry basis unbound water, would be approximately $C_1H_{1.94}O_{0.83}N_{0.001}$. Since no constraint has been placed on the exact fuel composition and moisture content, the elemental composition of the fuel can be determined as a function of time. Figure 5-11 shows the ratios H/C, O/C, and N/C as a function of time. Distinct stages of drying, pyrolysis/combustion, and charcoal oxidation are identified in Figure 5-11. In the drying stage the majority of unbound fuel moisture has been driven from the fuel resulting in an increase in effective H and O atomic ratios in the fuel. This is further supported by integrating the fuel based H_2O where approximately 2.2 kg (amount of free H_2O contained in 28 kg of 8.3% moist fuel) has been released at approximately 0.25 hrs, corresponding with the end of the drying stage. The second stage consists of a combination of virgin fuel pyrolysis and combustion resulting in a linear decrease in H and O with time until the fuel H has been oxidized. Stage three starting at approximately 2.75hrs is characterized by the full consumption of H and O leading to the charcoal oxidation stage. The nitrogen slowly increases as the remaining charcoal is further depleted.

5.2.8.2 Time History: Heating Value

The time dependent fuel composition can be used to estimate the higher heating value of the fuel [27].

$$\text{Equation 5-6 } HHV = (33.5[CC] + 142.3[HC] - 15.4[OC] - 14.5[NC]) \times 10^{-2}$$

Equation 5-6 represents the HHV [MJ/kg] for biomass fuel given a specified elemental mass percentage for carbon (CC), hydrogen (HC), oxygen (OC), and nitrogen (NC) [27]. Figure 5-12 presents the HHV for the variable fuel composition with comparison to reference values for red oak (with 8.3% moisture content) and coal. The images in Figure 5-12 show the progression of the burn at early and late times. As the virgin fuel dries early in time, it undergoes pyrolysis and forms charcoal, and the HHV is reduced (close to the constant value of 17.5 MJ/kg for red oak). The later burning is characterized primarily by charcoal oxidation, where the HHV approaches that of coal (32.3 MJ/kg).

5.2.8.3 Time History: Thermal Efficiency

Thermal efficiency is often expressed in terms of total (integrated) heat delivered (ΔQ_{del}) divided by the total caloric chemical energy available (ΔQ_{comb}) of the fuel used, (*i.e.*), $\bar{\eta}_{th} = \Delta Q_{del} / \Delta Q_{comb}$, where a single efficiency is reported per fuel charge [8]. While this definition provides an estimate of the average efficiency of an appliance, it is limited since important transient information is lost. The missing time dependent information is useful for understanding the boiler dynamics to improve function and design. An instantaneous thermal efficiency (η_{th}) is therefore desirable. The practical calculation of it is difficult since, previously, the time dependent caloric value of the wood was unknown. Using the results from Figure 5-12, η_{th} can now be computed as: $\eta_{th} = (\dot{Q}_{del} + \dot{Q}_{stor}) / \dot{Q}_{comb}$, where $\dot{Q}_{comb} = (|\dot{m}_f| HHV)$ is the heat produced from combustion. The term $\dot{Q}_{stor} = C_b m_b (dT_b/dt)$ represents the instantaneous heat transferred to the boiler and is inferred from the measured mean water and wall temperatures. The term $\dot{Q}_{del} = C_w \dot{m}_w (T_{w,out} - T_{w,in})$ is the delivered heat to the thermal load (heat exchanger) which is experimentally determined from measurements of the water temperature and flow rate going in ($T_{w,in}$) and out ($T_{w,out}$) of the boiler. Figure 5-13 shows \dot{Q}_{del} , \dot{Q}_{stor} , $\dot{Q}_{combVFF}$, and $\dot{Q}_{combCFF}$ versus time for a typical boiler run. It can be seen that \dot{Q}_{del} and \dot{Q}_{stor} are inversely proportional, indicating the heat rate delivered from the water is coming from the boiler heat capacitance, rather than from the heat generated from combustion. Compared to the CFF description, the heat release from the VFF is comparatively lower in the beginning and higher at the end, which is consistent with the individual fuel descriptions for red oak and coal. Figure 5-14 shows a comparison of the VFF and CFF instantaneous efficiency as a function of time. The efficiency using the CFF heating value (Figure 5-13, blue dashed line) results in non-physical values greater than unity. It is only when the heating value derived from the VFF (Figure 5-13, red solid line) is

used that physically realistic efficiencies are achieved. Integrated thermal efficiencies ($\bar{\eta}_{th} = (\Delta Q_{del} + \Delta Q_{stor}) / \Delta Q_{comb}$) calculated with CFF and VFF are comparable at approximately $\bar{\eta}_{thCFF} = 50\%$ and $\bar{\eta}_{thVFF} = 54\%$, respectively.

5.2.9 Conclusions

An experimental facility was modified for further experimental diagnostics, including direct measurements of air flow rates and a TDLAS setup at the flue [40]. Emissions and flow rate measurements are used in the new analysis and validated using direct, non-intrusive, first principles-based TDLAS measurements of CO_2 and H_2O . The analysis provides estimates of major exhaust species and changes in elemental fuel composition using emissions measurements of CO , NO , and O_2 and flow measurements of fuel and air. Good agreement was shown in the validation, comparing predictions of CO_2 and H_2O to TDLAS measurements.

This new analysis provides a clear description of the various stages in fuel decomposition for batch-run wood burning systems. The changing elemental composition of the fuel is calculated without direct knowledge of the exact wood type or unbound moisture content. Three distinct burn stages are presented, including drying, pyrolysis/combustion, and charcoal oxidation. Time dependent higher heating values are calculated based on the changing elemental composition with a range from 10 to 33 MJ/kg, consistent with the known fuel stages. Finally, instantaneous thermal efficiencies are calculated using the changing elemental fuel composition (VFF) and are shown to provide physically realistic values below unity.

Figure 5-1. Schematic of Water Vapor Dilution Experiment

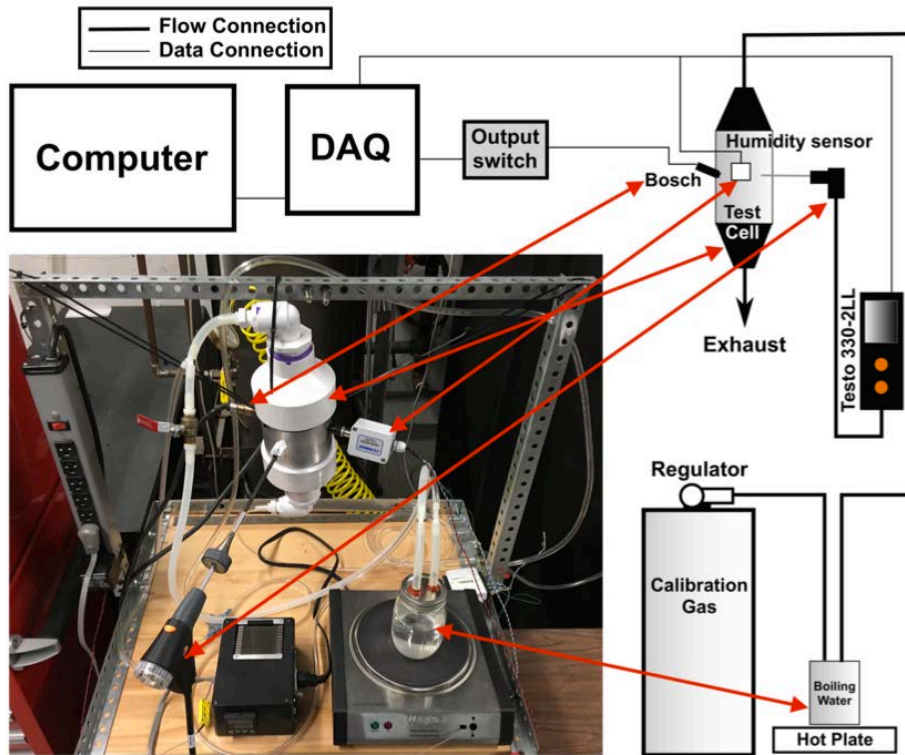


Figure 5-2. Oxygen Concentrations Comparisons

Oxygen concentrations over time (a. air, b. 15% O₂ and c. 10% O₂, rest N₂) with experimental uncertainty bounds plots of gas temperature and relative humidity are shown below. Calculated (black) value based on measured temperature and humidity calculated from psychrometric relations.

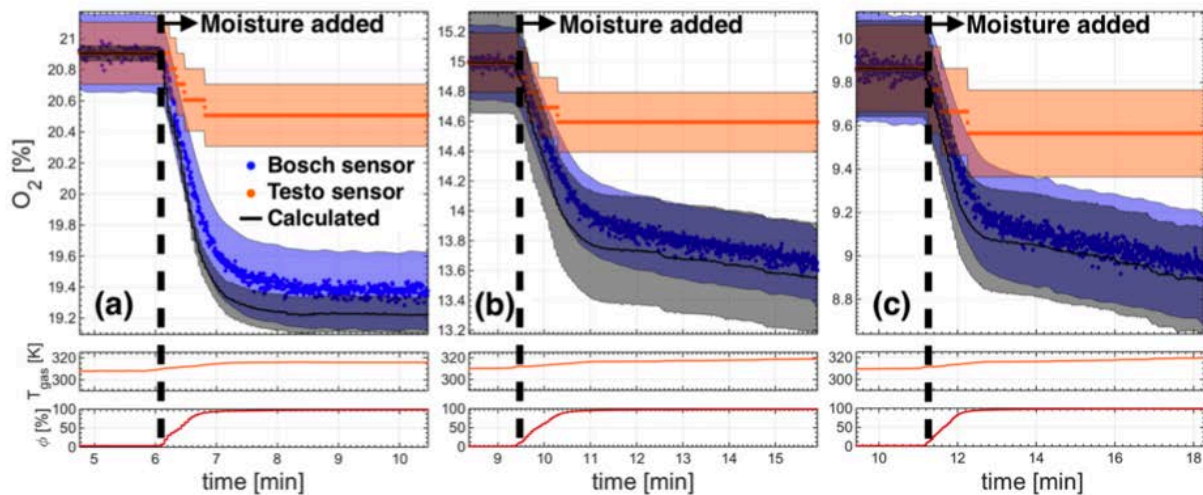


Figure 5-3. Higher Temperature Oxygen Comparison Case

Specialized higher temperature case run with a gas mixture of (a) 5% O₂ and (b) 5020 ppm CO, the rest is N₂, demonstrating the CO correction.

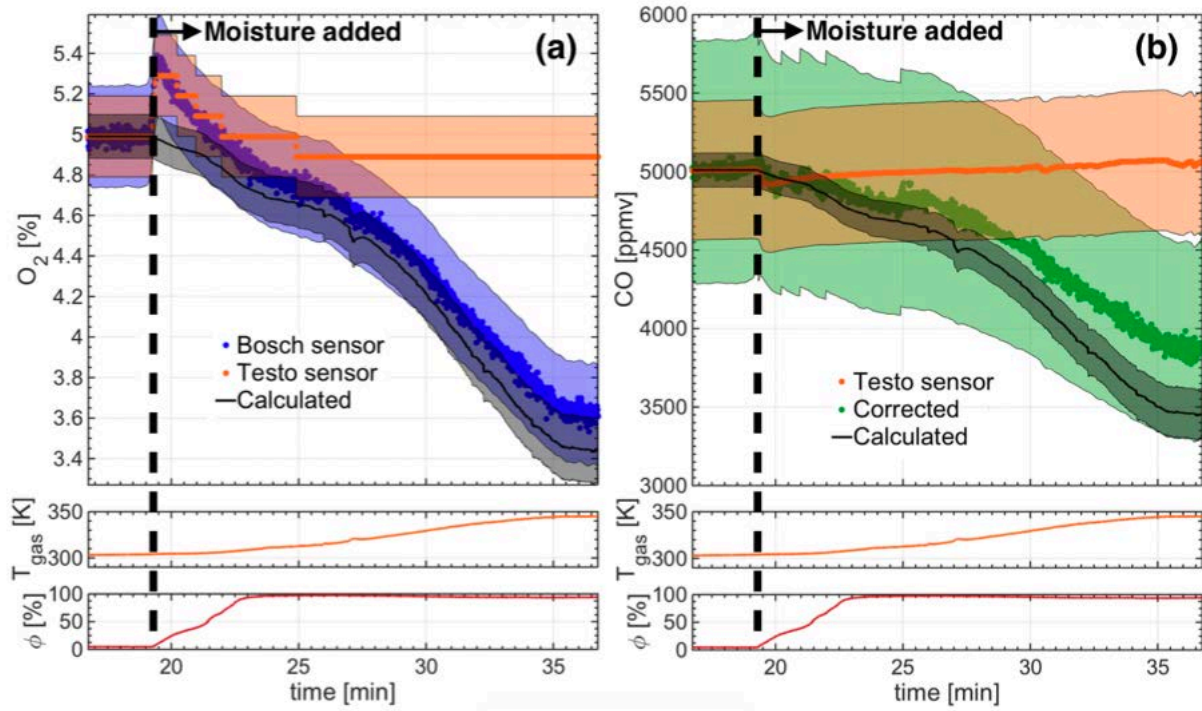
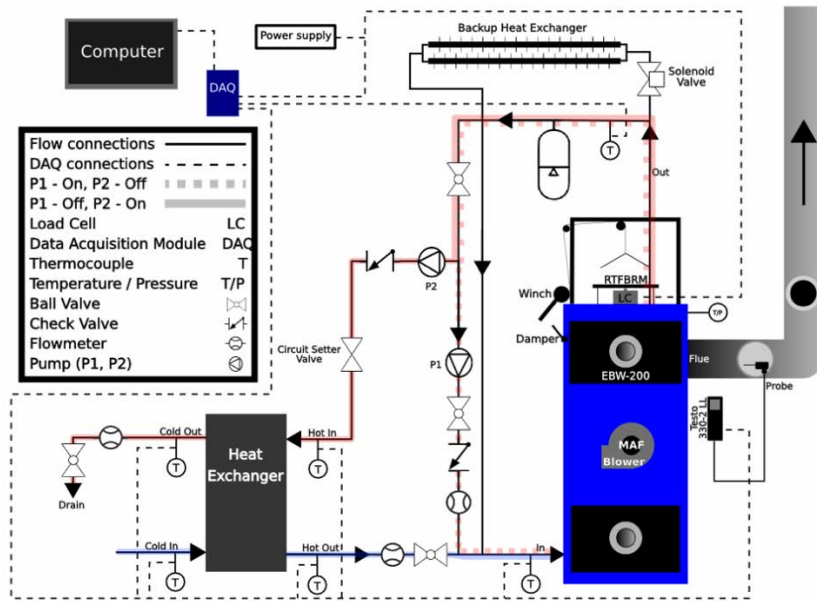


Figure 5-4. Experimental Schematic and RTFBRM

Experimental facility showing (a) experimental schematic and (b) RTFBRM load cell with cross member and hanging basket.

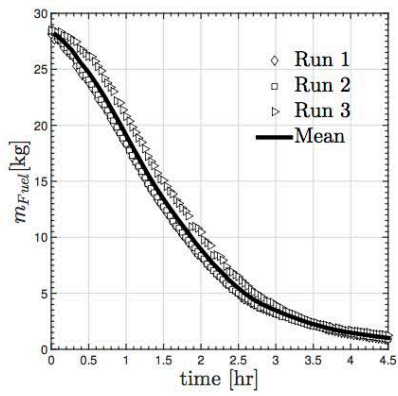


(a)

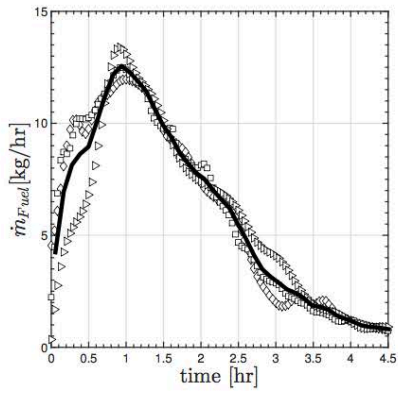


(b)

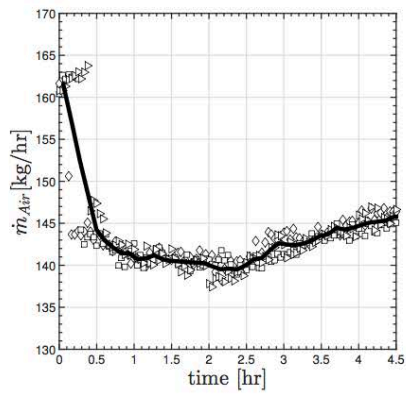
Figure 5-5. Comparison of Mass, Burn Rate, and Air Flow Rate



(a)



(b)



(c)

Figure 5-6. Comparison of O₂, CO, and NO

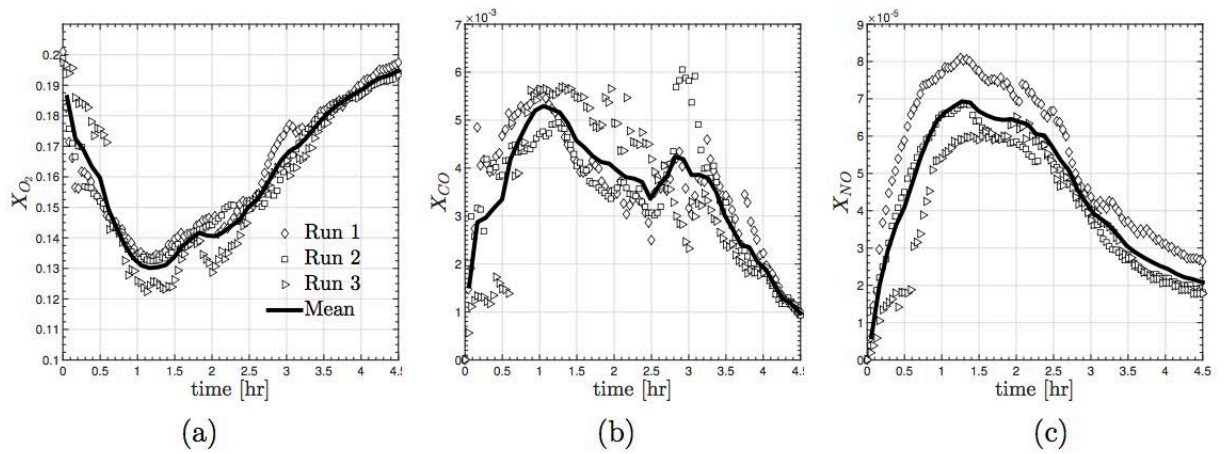


Figure 5-7. TDLAS Schematic

TDLAS setup showing pitch and catch configuration with zoomed in flue and catch side image.

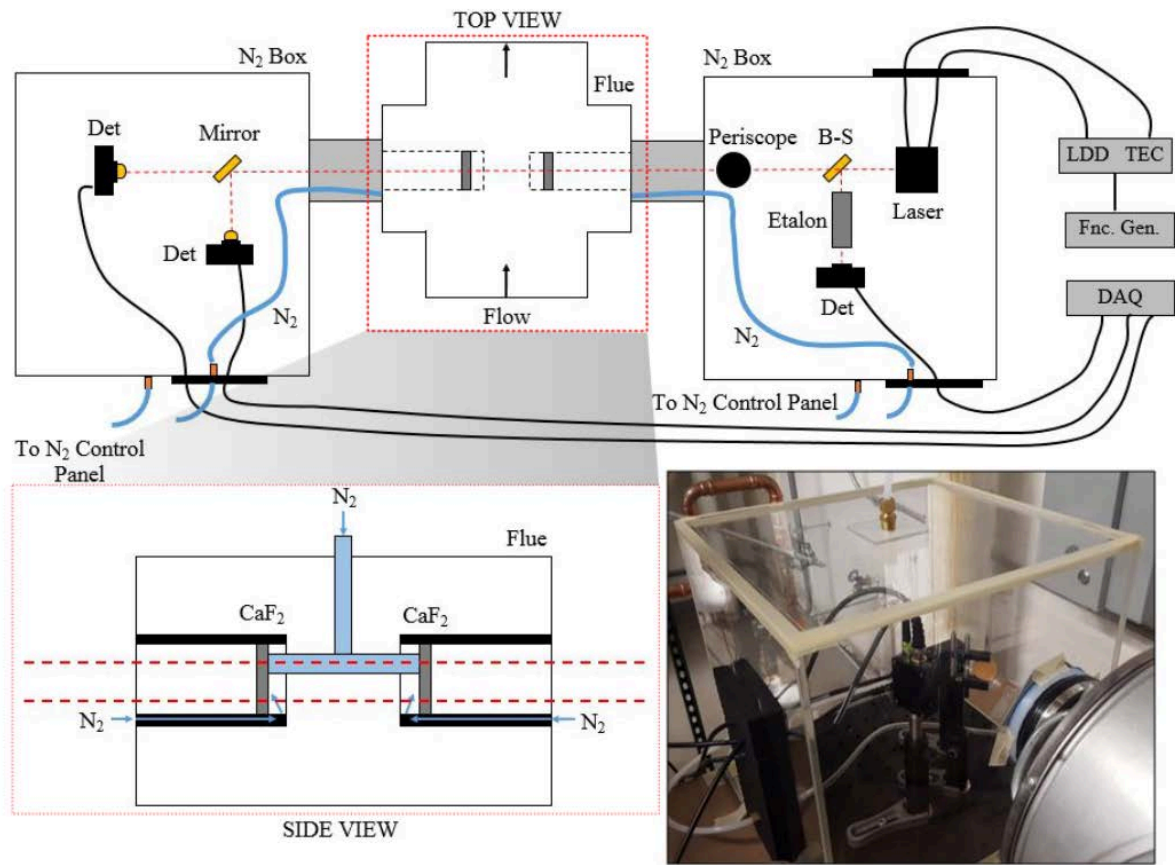


Figure 5-8. Chi-Squared Surface and Comparison of Raw Data with Best Fit Simulation

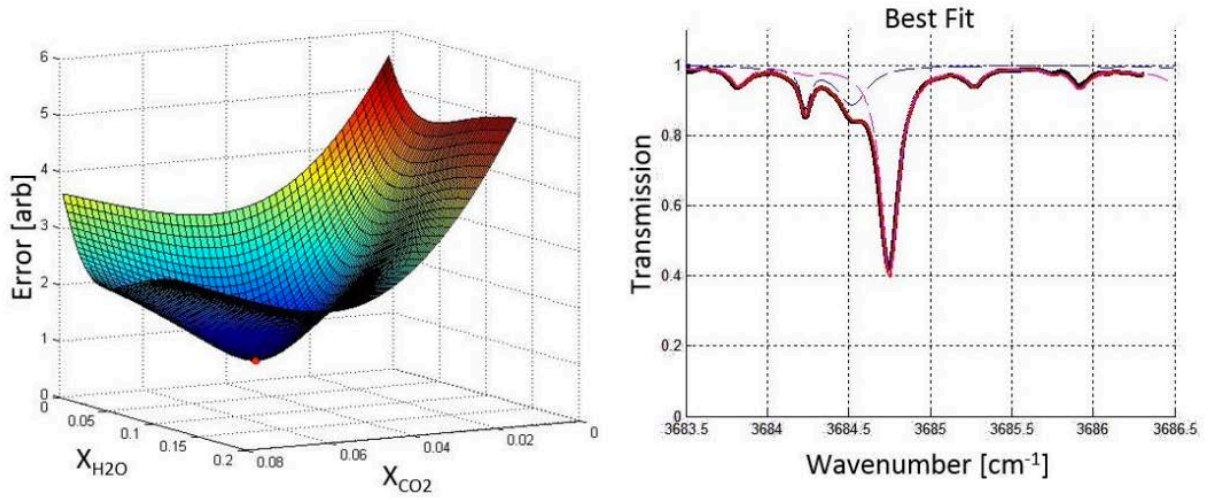


Figure 5-9. Comparison of Variable Fuel and Constant Fuel Formulations with TDLAS for CO_2

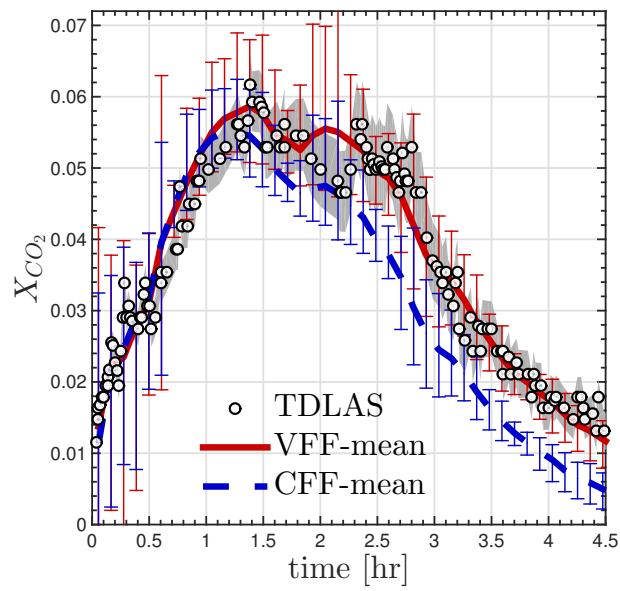


Figure 5-10. Comparison of Variable Fuel and Constant Fuel Formulations with TDLAS for H₂O

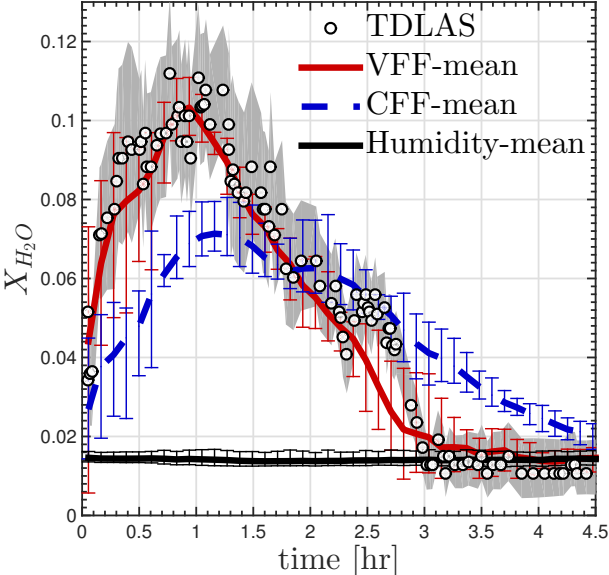


Figure 5-11. Atomic Ratio for H, O, and N

Atomic ratio of HON normalized by carbon for experimental variation in BIOBLOCK[®] fuel composition.

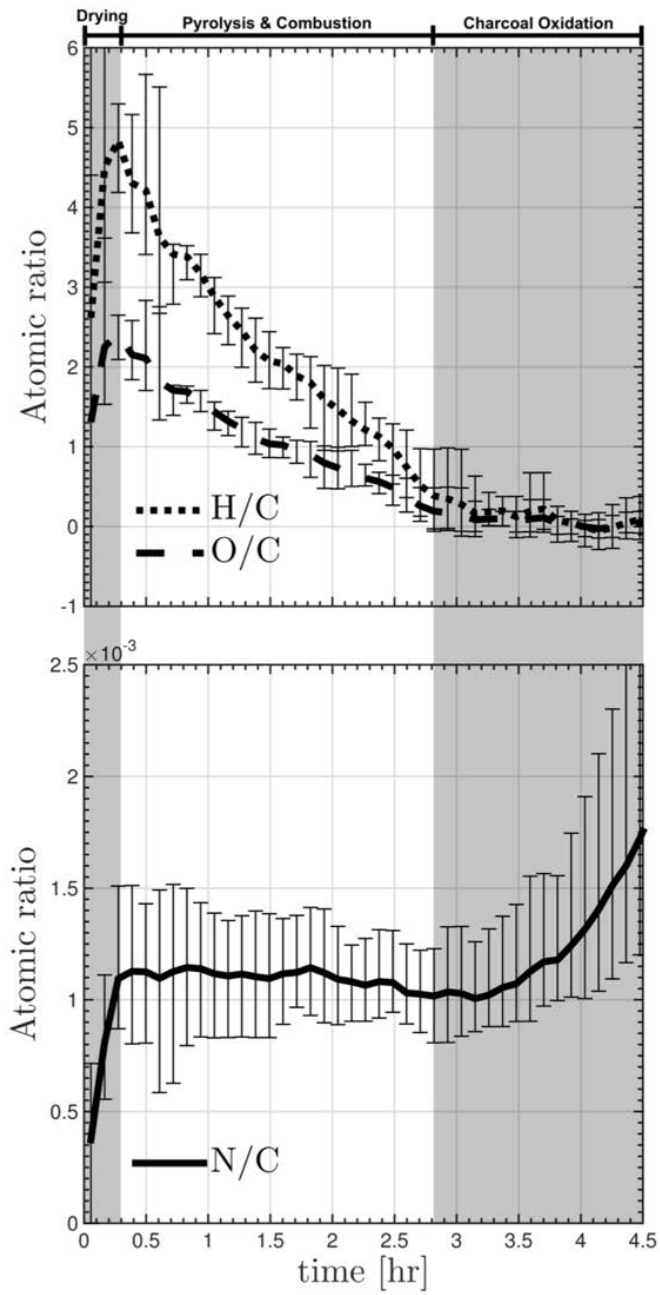


Figure 5-12. Comparison of Variable Fuel HHV

Comparison of variable fuel HHV with constant fuel values for Red Oak and Coal. Fuel images show early (mixed pyrolysis and charcoal formation) and late (charcoal oxidation) fuel burn progression.

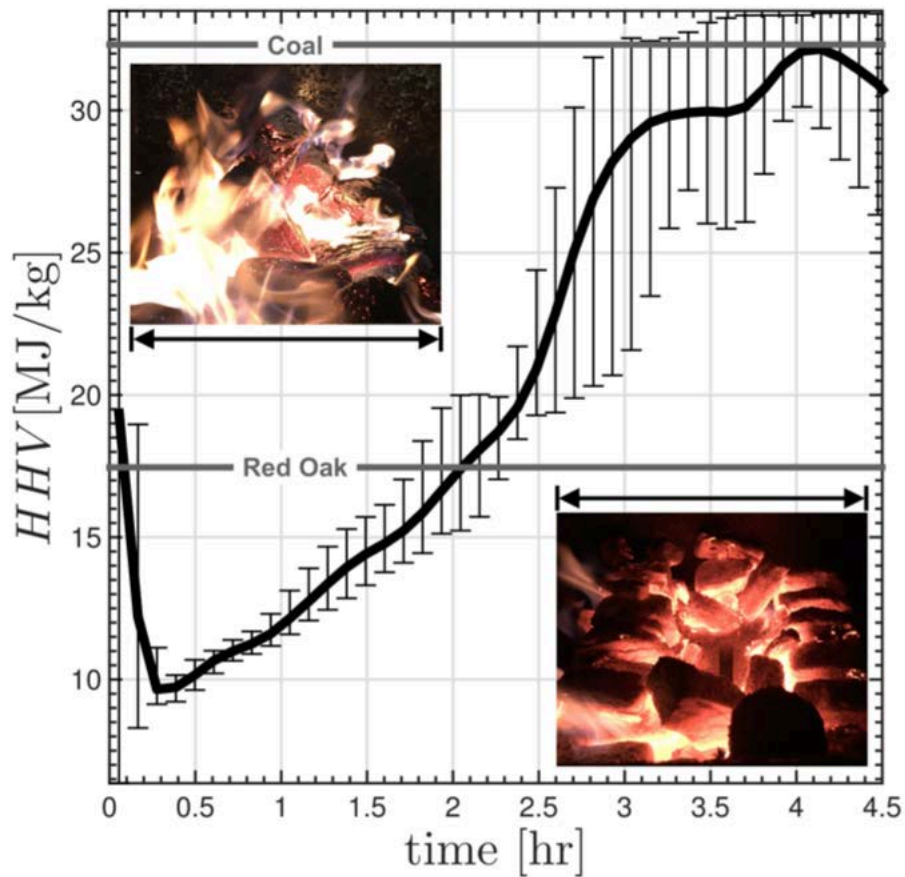


Figure 5-13. Summary of Thermal Heat Rates

Summary of thermal heat rates showing \dot{Q}_{del} , \dot{Q}_{stor} , \dot{Q}_{combCF} and \dot{Q}_{combVF} for a single characteristic case.

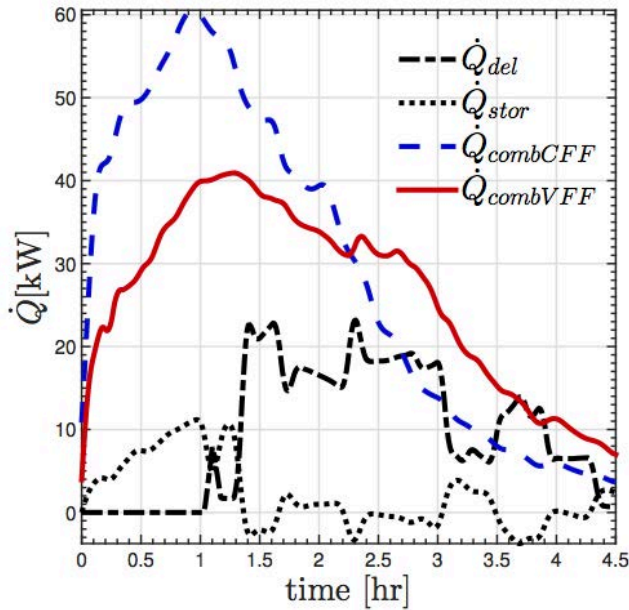
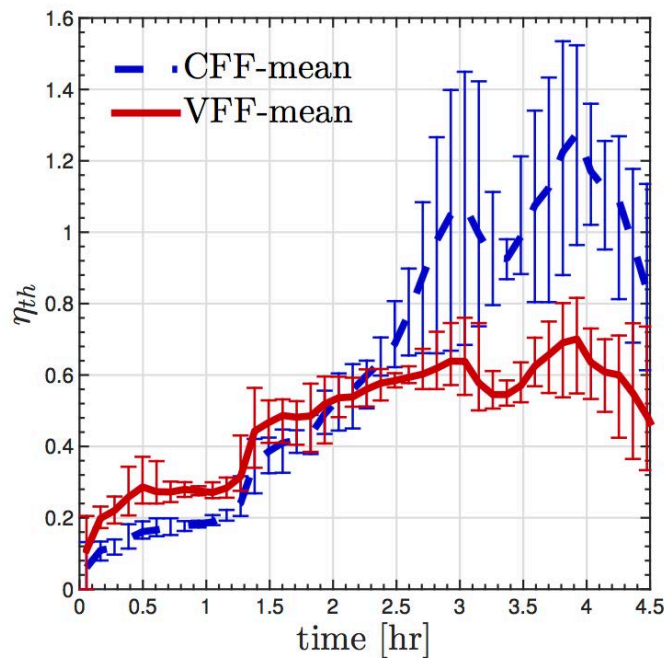


Figure 5-14. Instantaneous Real Time Thermal Efficiency Comparison

Instantaneous real time thermal efficiency comparison using constant fuel heat of combustion versus time dependent variable fuel heat of combustion.



References

1. Richter, J.P., J.C. Mollendorf, and P.E. DesJardin, *Absolute and Relative Emissions Analysis in Practical Combustion Systems - Effect of Water Vapor Condensation*. Measurement Science and Technology, 2016.
2. Richter, J.P., et al., *Emissions From a Domestic Two-Stage Wood-Fired Hydronic Heater - Effects of Non-homogeneous Fuel Decomposition*. Renewable Energy, 2016: p. (under review).
3. Weisberger, J.M., et al., *Emissions from a domestic two-stage wood-fired hydronic heater - effects of fuel variation on non-homogenous fuel decomposition*. 2017: p. (in preparation to be submitted).
4. Bojko, B.T. and P.E. DesJardin, *Formulation and assessment of flamelet-generated manifolds for reacting interfaces*. Combust. Flame, 2016. **173**: p. 296--306.
5. Bojko, B.T., *On the formulation and assessment of flamelet generated manifolds applied to two phase turbulent combustion*, in *Mechanical and Aerospace Engineering*. 2016, University at Buffalo, State University of New York.
6. Richter, J.P., et al., *Emissions from a domestic two-stage wood-fired hydronic heater - development of a system level modelling with flamelet generated manifolds*. Renewable Energy, 2017: p. (in preparation to be submitted).
7. Butcher, T.A., *A Test Method for Certification of Cord Wood-Fired Hydronic Heating Appliances with Partial Thermal Storage: Measurement of Particulate Matter (PM) and Carbon Monoxide (CO) Emissions and Heating Efficiency of Wood-Fired Hydronic Heating Applications with Partial Thermal Storage*. 2013, Brookhaven National Laboratory.
8. Butcher, T. and N. Russell, *Review of EPA Method 28 Outdoor Wood Hydronic Heat Test Results*. 2011, New York State Energy Research and Development Authority (NYSERDA).
9. Butcher, T., et al., *Report on Testing of the Econoburn Model EBW200-170 Wood Hydronic Heater Using Partial Thermal Storage*. 2014, Brookhaven National Laboratory.
10. Nussbaumer, T. and J. Good, *Determination of the combustion efficiency in biomass furnaces*, in *Proceedings 10th European conference and technology Exhibition biomass for energy, industry and climate protection*. Würzburg. 1998.
11. Association., C.S., *CAN/CSA-B415.1-92 Performance Testing of Solid-Fuel-Burning Stoves, Inserts, and Low-Burn-Rate Factory-Built Fireplaces*. CSA standard., 1992: p. 77.
12. Workgroup, C.T.M., *Performance Testing of Solid-Fuel-Burning Heating Appliances*. CSA Standard B415.1-10. 2010.
13. Kang, S.B., et al., *Development of a test facility to evaluate performance of a domestic wood pellet boiler*. Renewable Energy, 2013. **54**: p. 2--7.
14. Rehfuess, E. and others, *Fuel for life: household energy and health*. 2006.
15. Guo, M., W. Song, and J. Buhain, *Bioenergy and biofuels: History, status, and perspective*. Renewable and Sustainable Energy Reviews, 2015. **42**: p. 712--725.
16. Parikka, M., *Global biomass fuel resources*. Biomass and Bioenergy, 2004. **27**(6): p. 613 - 620.
17. Berndes, G., M. Hoogwijk, and R. van den Broek, *The contribution of biomass in the future global energy supply: a review of 17 studies*. Biomass and bioenergy, 2003. **25**(1): p. 1--28.
18. Yevich, R. and J.A. Logan, *An assessment of biofuel use and burning of agricultural waste in the developing world*. Global biogeochemical cycles, 2003. **17**(4).
19. Fischer, G. and L. Schrattenholzer, *Global bioenergy potentials through 2050*. Biomass and bioenergy, 2001. **20**(3): p. 151--159.
20. Saidur, R., et al., *A review on biomass as a fuel for boilers*. Renewable and Sustainable Energy Reviews, 2011. **15**: p. 2262--2289.
21. Chaney, J., H. Liu, and J. Li, *An overview of CFD modeling of small-scale fixed-bed biomass pellet boilers with preliminary results from a simplified approach*. Energy Conversion and Management, 2012. **63**: p. 149--156.

22. Collazo, J., et al., *Numerical simulation of a small-scale biomass boiler*. Energy Conversion and Management, 2012. **64**: p. 87--96.
23. Sefidari, H., N. Razmjoo, and M. Strand, *An experimental study of combustion and emissions of two types of woody biomass in a 12-MW reciprocating-grate boiler*. Fuel, 2014. **135**: p. 120--129.
24. Roy, M.M. and K.W. Corscadden, *An experimental study of combustion and emissions of biomass briquettes in a domestic wood stove*. Applied Energy, 2012. **99**: p. 206--212.
25. Ryfa, A., et al., *Decoupled numerical simulation of a solid fuel fired retort boiler*. Applied Thermal Engineering, 2014. **73**: p. 794--804.
26. Agency, N.F.P., *The SFPE Handbook of Fire Protection Engineering*. 1995, Quincy, MA: National Fire Protection Agency.
27. Demirbas, A., *Combustion characteristics of different biomass fuels*. Progress in energy and combustion science, 2004. **30**(2): p. 219--230.
28. Reynolds, W., *The element potential method for chemical equilibrium analysis: Implementation in the interactive program STANJAN, version 3*. Technical Rept., 1986.
29. Pope, S.B., *Gibbs function continuation for the stable computation of chemical equilibrium*. Combustion and Flame, 2004. **139**(3): p. 222 - 226.
30. Bajus, M., *Pyrolysis of woody material*. Petroleum & Coal, 2010. **52**(3): p. 207--214.
31. Ragland, K., D. Aerts, and A. Baker, *Properties of wood for combustion analysis*. Bioresource technology, 1991. **37**(2): p. 161--168.
32. Gomez-Barea, A., et al., *Prediction of gas composition in biomass gasifiers.*, in *2nd International Congress of Energy and Environment Engineering and Management (IICIEEM2007)*. 2007.
33. Brent, R.P., *Algorithms for minimization without derivatives*. 2013: Courier Corporation.
34. Barber, C.B., D.P. Dobkin, and H.T. Huhdanpaa, *The Quickhull algorithm for convex hulls*. ACM Trans. on Mathematical Software, 1996. **22**(4): p. 469-483.
35. Watson, D., *Contouring: a guide to the analysis and display of spatial data*. 2013: Elsevier.
36. Kamimoto, T. and M.-h. Bae, *High combustion temperature for the reduction of particulate in diesel engines*. 1988, SAE Technical Paper.
37. Akihama, K., et al., *Mechanism of the smokeless rich diesel combustion by reducing temperature*. 2001, SAE Technical Paper.
38. Kaario, O., et al., *Studying Equivalence ratio--Temperature Maps in a Heavy-Duty Diesel Engine*. Swedish-Finnish Flame Days Paper, 2011. **16**.
39. Kinsey, J.S., et al., *Emissions characterization of residential wood-fired hydronic heater technologies*. Atmospheric Environment, 2012. **63**: p. 239--249.
40. Richter, J.P., et al., *Measurements of fuel burn rate, emissions and thermal efficiency from a domestic two-stage wood-fired hydronic heater*. Renewable Energy, 2016. **96**: p. 400-409.
41. Miettinen, H., M. Paulsson, and D. Stroemberg, *Laboratory study of N₂O formation from burning char particles at FBC conditions*. Energy & fuels, 1995. **9**(1): p. 10--19.
42. Nussbaumer, T., *Combustion and co-combustion of biomass: fundamentals, technologies, and primary measures for emission reduction*. Energy & fuels, 2003. **17**(6): p. 1510--1521.
43. Zhang, X., et al., *Experimental investigation and mathematical modelling of wood combustion in a moving grate boiler*. Fuel Processing Technology, 2010. **91**(11): p. 1491--1499.
44. Eskilsson, D., et al., *Optimisation of efficiency and emissions in pellet burners*. Biomass and Bioenergy, 2004. **27**(6): p. 541--546.
45. González, J.F., et al., *Combustion optimisation of biomass residue pellets for domestic heating with a mural boiler*. Biomass and Bioenergy, 2004. **27**(2): p. 145--154.
46. Koziński, J.A. and R. Saade, *Effect of biomass burning on the formation of soot particles and heavy hydrocarbons. An experimental study*. Fuel, 1998. **77**(4): p. 225--237.
47. Ozil, F., et al., *Efficiency of catalytic processes for the reduction of CO and VOC emissions from wood combustion in domestic fireplaces*. Fuel Processing Technology, 2009. **90**(9): p. 1053--1061.

48. DesJardin, P.E., B.T. Bojko, and M.T. McGurn, *Initialization of high-order accuracy immersed interface CFD solvers using complex CAD geometry*. Int. J. Numer. Meth. Eng., 2016.
49. Lehmann, J., *A handful of carbon*. Nature, 2007. **447**(7141): p. 143--144.
50. Bhat, I., R. Prakash, and others, *LCA of renewable energy for electricity generation systems---a review*. Renewable and Sustainable Energy Reviews, 2009. **13**(5): p. 1067--1073.
51. Lund, H., et al., *The role of district heating in future renewable energy systems*. Energy, 2010. **35**(3): p. 1381--1390.
52. Porteiro, J., et al., *Numerical modeling of a biomass pellet domestic boiler*. Energy & Fuels, 2009. **23**(2): p. 1067--1075.
53. Rabaçal, M., U. Fernandes, and M. Costa, *Combustion and emission characteristics of a domestic boiler fired with pellets of pine, industrial wood wastes and peach stones*. Renewable Energy, 2013. **51**: p. 220--226.
54. Jenkins, B., L. Baxter, and T. Miles, *Combustion properties of biomass*. Fuel processing technology, 1998. **54**(1): p. 17--46.
55. Bignal, K.L., S. Langridge, and J.L. Zhou, *Release of polycyclic aromatic hydrocarbons, carbon monoxide and particulate matter from biomass combustion in a wood-fired boiler under varying boiler conditions*. Atmospheric Environment, 2008. **42**(39): p. 8863--8871.
56. Pettersson, E., et al., *Stove performance and emission characteristics in residential wood log and pellet combustion, part 2: wood stove*. Energy & Fuels, 2011. **25**(1): p. 315--323.
57. Pemberton-Pigott, C., *Calculating Energy Efficiency Using a Chemical Mass Balance Method*. Brookhaven National Laboratory - Pellet Stove Workshop (Personal Communication), 2016.
58. De Soete, G.G., *Overall reaction rates of NO and N₂ formation from fuel nitrogen*, in *Symposium (international) on combustion*. 1975. p. 1093--1102.
59. Glarborg, P., A. Jensen, and J.E. Johnsson, *Fuel nitrogen conversion in solid fuel fired systems*. Progress in Energy and Combustion Science, 2003. **29**(2): p. 89--113.
60. Sartor, K., et al., *Prediction of SO_x and NO_x emissions from a medium size biomass boiler*. Biomass and Bioenergy, 2014. **65**: p. 91--100.
61. Kinsey, J.S., et al., *Emissions characterization of residential wood-fired hydronic heater technologies*. Atmospheric environment, 2012. **63**: p. 239--249.
62. McEwen, D., *Automobile Exhaust Hydrocarbon Analysis by Gas Chromatography*. Analytical Chemistry, 1966. **38**(8): p. 1047--1053.
63. Christian, T.J., et al., *Comprehensive laboratory measurements of biomass-burning emissions: 2. First intercomparison of open-path FTIR, PTR-MS, and GC-MS/FID/ECD*. Journal of Geophysical Research: Atmospheres, 2004. **109**(D2).
64. Limousy, L., et al., *Gaseous products and particulate matter emissions of biomass residential boiler fired with spent coffee grounds pellets*. Fuel, 2013. **107**: p. 323--329.
65. Liu, J.T., et al., *Near-infrared diode laser absorption diagnostic for temperature and water vapor in a scramjet combustor*. Applied Optics, 2005. **44**(31): p. 6701--6711.
66. Yokelson, R.J., D.W. Griffith, and D.E. Ward, *Open-path Fourier transform infrared studies of large-scale laboratory biomass fires*. Journal of Geophysical Research: Atmospheres, 1996. **101**(D15): p. 21067--21080.
67. Lackner, M., *Tunable diode laser absorption spectroscopy (TDLAS) in the process industries--a review*. Reviews in Chemical Engineering, 2007. **23**(2): p. 65--147.
68. Qu, Z. and F.M. Schmidt, *Low-cost TDLAS sensor for real-time in-situ temperature and H₂O measurements in biomass combustion applications*, in *Field Laser Applications in Industry and Research, May 5-9, 2014, Florence, Italy*. 2014.
69. Nakamura, H.K., N.; Adachi M.; Ishida K., *Development of a Wet-Based NDIR and Its Application to On-Board Emission Measurement System*. 2002: Warrendale, Penn.
70. Truex, T., Collins J. Jetter J. Knight B. et al., *Measurement of Ambient Roadway and Vehicle Exhaust Emissions-An Assessment of Instrument Capability and Initial On-Road Test Results with an Advanced Low Emission Vehicle*. 2000, SAE Technical Paper 2000-01-1142.

71. Griffiths, P.R. and J.A. De Haseth, *Fourier transform infrared spectrometry*. Vol. 171. 2007: John Wiley & Sons.
72. Griffith, D.W., et al., *FTIR remote sensing of biomass burning emissions of CO₂, CO, CH₄, CH₂O, NO, NO₂, NH₃, and N₂O*, in *Global biomass burning. Atmospheric, climatic, and biospheric implications*. 1991.
73. Goode, J.G., et al., *Trace gas emissions from laboratory biomass fires measured by open-path Fourier transform infrared spectroscopy: Fires in grass and surface fuels*. Journal of Geophysical Research: Atmospheres, 1999. **104**: p. 21237.
74. Jecht, U., *Flue Gas Analysis in Industry; Practical guide for Emission and Process Measurements*. Testo AG.
75. Takeuchi, T., *Oxygen sensors*. Sensors and Actuators, 1988. **14**(2): p. 109--124.
76. Durst, R.A., *Ion-selective electrodes: proceedings*. 1969, Washington: US National Bureau of Standards.
77. Wagner, W. and A. Pruss, *International equations for the saturation properties of ordinary water substance. Revised according to the international temperature scale of 1990. Addendum to J. Phys. Chem. Ref. Data 16, 893 (1987)*. Journal of Physical and Chemical Reference Data, 1993. **22**(3): p. 783--787.
78. Ziegler, B. and W. Keen, *Test Of A Wood-Fired Outdoor Hydronic HeHeat For Emissions and Efficiency*. 2008, Intertek Testing Services NA INC.
79. Nussbaumer, T., E. Burkhard, and R. Albrecht, *Biomass Combustion in Europe Overview on Technologies and Regulations*. 2008, New York State Energy Research and Development Authority (NYSERDA).
80. Saidur, R., et al., *A review on biomass as a fuel for boilers*. Renewable and Sustainable Energy Reviews, 2011. **15**(5): p. 2262--2289.
81. Wiggins, G.M., *Evaluation of Biomass and Coal Briquettes for a Spreader Stoker Boiler Using an Experimental Furnace---Modeling and Test*. 2011.
82. Di Blasi, C., *Processes of flames spreading over the surface of charring fuels: effects of the solid thickness*. Combustion and Flame, 1994. **97**(2): p. 225--239.
83. Di Blasi, C., *Modeling and simulation of combustion processes of charring and non-charring solid fuels*. Progress in Energy and Combustion Science, 1993. **19**(1): p. 71--104.

Appendix A. Testing and Safety Protocols

A.1 Testing Protocol

Testing protocols have been defined as follows:

1. Laboratory exhaust fans are turned off and doors closed to allow sufficient flue draft.
2. Data acquisition instruments are turned on.
3. RTFBRM hanging basket rods are cleaned and replaced if necessary.
4. Wood kindling, newspaper and BIOBLOCKS are carefully placed into the basket for the initial cold start run. Arrangement of blocks and kindling are as follows: two rows of 7 are placed on the bottom left and right sides of the hanging basket the center is filled with kindling and newspaper and a two row grid pattern of kindling is place on top with the remained 18 blocks placed in 4 sets of 4 in a triangular arrangement with the final two blocks placed on top (Fig. 2 below shows the arrangement partially completed).
5. The Testo gas analyzer is placed in the flue stack approximately 3 feet from the back of the boiler.
6. Data acquisition systems are initialized and the newspaper/kindling is ignited with a propane torch.
7. As the water temperature and flue temperature begin to rise the damper is left open until a draft can be sustained (approximately 300°F, read by the Testo meter).

A.2 Safety Protocol

Pre-run notification contacts

University Facilities Customer Service (8am-4:30pm): 645 2025

University Facilities Central Chilled Water Plant (24/7): 645-2205

University Police (normal start notification): 645-2222

Start and operating hours:

1. Call above contacts (30 minutes prior) before starting experiment ignition! Use contact list above and notify university services. Call again to notify university when an experiment cycle is complete. Each and every cycle requires university notification.
2. **The combustion experiment should only be “started”** between the hours of 7am thru 12noon; Monday thru Thursday. This will allow for the coordination of support services if needed. Once the combustion experiment is established it may run 24/7 until that experiment cycle is complete.

3. The experiment room shall be manned with a minimum of one person trained to observe and monitor the combustion experiment. Training qualifications and supervision requirements will be established by the Mechanical Engineering Department.
4. A cell phone or land line shall be available to the personnel operating the experiment.

Room Environmental Preparation (rooms 312 and 304):

1. Turn off all exhaust canopies and fume hoods.
2. Close “*double doors*” to rooms 312 and 304. Double doors must be closed thru duration of a combustion cycle to ensure correct boiler draft conditions.
3. Open single door that connects rooms 312 to room 304.
4. The room will get warm and humid. It’s a combustion experiment. Normal room AC systems will not provide normal classroom comfort levels.

Personnel Protection:

1. DO NOT under any circumstances spray water onto the boiler or into the firebox of the boiler. Resultant thermal shock may rupture heat exchanger surfaces with release of large quantity of flash steam.
2. Operate boiler in accordance with boiler manufacturer’s written instructions.
3. All surfaces on the experiment shall be assumed hot and hazardous. Avoid touching surfaces unless protected with leather gloves. An infrared non-contact thermometer may be used to pre-test surfaces.
4. Room floor may occasionally have water spillage, clean and dry to minimize slip and falls hazards. Walk and do not run in the room. Water may be pushed into the floor drains behind the boiler piping gallery.
5. The flue surface is capable of melting clothing fabricated from synthetic fibers.
6. Only closed toed shoes, boots, or sneakers shall be worn in the experiment room. Sandals and heels are prohibited.

7. Adding fuel to the combustion chamber: When adding fuel to the boiler fire, wear fire resistant welding gloves with gauntlets. Wear long sleeve fire resistant lab coat (Nomex or Indura). Coat shall be fully buttoned.

Shorts and skirts are prohibited in the room during and experimental cycle. Full-length pants are the recommended attire. Long sleeve shirts are recommended for persons working in close proximity to the experiment. Cotton clothing is recommended.